

TECHNISCHE UNIVERSITÄT MÜNCHEN

Lehrstuhl für Biologische Bildgebung

Multispectral optoacoustic tomography for imaging of disease biomarkers

Adrian Taruttis

Vollständiger Abdruck der von der Fakultät für Elektrotechnik und Informationstechnik der Technischen Universität München zur Erlangung des akademischen Grades eines

Doktor-Ingenieurs

genehmigten Dissertation.

Vorsitzender: Univ.-Prof. Dr. Klaus Diepold

Prüfer der Dissertation:

1. Univ.-Prof. Vasilis Ntziachristos, Ph.D.
2. Univ.-Prof. Dr. Gil G. Westmeyer

Die Dissertation wurde am 29.09.2011 bei der Technischen Universität München eingereicht und durch die Fakultät für Elektrotechnik und Informationstechnik am 26.04.2012 angenommen.

Kurzfassung

Multispektrale Optoakustische Tomografie (MSOT) ist ein neues Verfahren, das auf Ultraschall-Detektion von optischer Absorption, basierend auf dem photoakustischen Effekt, beruht und krankheitsrelevante biologische Vorgänge auflösen kann. Das Verfahren erlaubt die Darstellung intrinsischen optischen Gewebekontrastes, sowie einer Vielzahl von Kontrastmitteln bei hoher Auflösung, vergleichbar mit der von Ultraschall. Die vorliegende Dissertation beschreibt entscheidende Methoden und Ergebnisse, die im Laufe des Forschungsvorhabens erreicht wurden. Studien wurden an Mäusen, unter anderem an Modellen für Krebs und Herz-Kreislaufkrankungen, durchgeführt, so konnte die Eignung von MSOT als bildgebendes Verfahren zum Nachweis von Biomarkern *in vivo* bestätigt werden. MSOT stellt sich zusammenfassend als ein Verfahren dar, das eine Reihe wertvoller Anwendungen ermöglicht, angefangen bei Kleintierbildgebungsstudien, wie in dieser Dissertation beschrieben, bis hin zur einer möglichen klinischen Translation.

Abstract

Biomedical imaging today is dominated by modalities informing on structure and morphology, like ultrasound, magnetic resonance imaging (MRI), and X-ray, with limited insight into the biology that underlies disease. Nuclear imaging provides valuable biological measures, but at a low spatial resolution, and at the cost of ionising radiation and decaying tracers. Multi-spectral optoacoustic tomography (MSOT), an emerging imaging technique based on the ultrasound detection of optical absorption via the photoacoustic effect, has the ability to image the biological processes involved in disease. The technique combines rich optical contrast, provided by intrinsic tissue absorbers and a multitude of optical imaging agents, with ultrasound resolution in deep tissues, breaking through the barrier that the high scattering of light raises after the first millimetre under the skin surface. By employing multi-wavelength illumination, MSOT distinguishes absorbers based on their spectral signatures, enabling multichannel imaging of specific chromophores of interest *in vivo* and thus visualisation of a diverse range of disease-related biomarkers. This thesis presents the critical aspects of the methods developed and results obtained during a research effort aimed at investigating the capabilities of MSOT in biomarker imaging. Studies were carried out on mice, including models of cardiovascular disease and cancer. It was possible to demonstrate the decomposition of multispectral measurements into separate channels, showing distributions of oxy- and deoxyhemoglobin, giving insight, for example, into the heterogeneous vascular architecture of tumors, and exogenous agents such as organic dyes and light absorbing nanoparticles, which allow the targeted probing of biological processes, demonstrated in the case of inflammation in myocardial infarction. By exploiting parallel ultrasound detection capabilities, it was further shown that such imaging can be performed at a high rate, enabling dynamic imaging of agent uptake in multiple anatomical regions. Although sufficient challenges remain for further research in this field, MSOT is found to be a method with a multitude of possible applications ranging from the small animal studies presented here, to clinical imaging applications, which will be a focus of future work.

Contents

1	Introduction	1
1.1	Why?	1
1.2	A brief introduction to MSOT	2
1.3	Imaging today	2
1.3.1	The gaps in current biomedical imaging modalities	2
1.3.2	Resolution versus penetration depth in optical imaging	3
1.4	How MSOT works	4
1.4.1	The optoacoustic (photoacoustic) effect	4
1.4.2	The development of biomedical optoacoustic imaging	4
1.4.3	Multispectral optoacoustic tomography	4
1.4.4	A minimal MSOT imaging system	5
1.4.5	An introductory experiment	6
1.5	The laboratory mouse	8
1.6	Objectives of this research	9
1.7	An outline of this work	10
2	The physics of pulsed optoacoustics	12
2.1	Introduction	12
2.2	Light propagation in biological tissue	12
2.3	Optoacoustic signal generation	15
2.4	Optoacoustic wave propagation	17
2.5	Concluding remarks	17
3	Instrumentation	20
3.1	Introduction	20
3.2	Optical excitation	20
3.2.1	Pulse duration for thermal and stress confinement	20
3.2.2	Multiple excitation wavelengths	21
3.2.3	Maximum exposure	21
3.2.4	Overall characteristics	21
3.3	Ultrasound signal detection	22
3.3.1	Detection technology	22
3.3.2	Optoacoustic signals in the frequency domain	22

3.3.3	Consequences of narrow-band optoacoustic signal de- detection	23
3.3.4	Acoustic focusing	27
3.3.5	Spatial resolution	29
3.4	Optoacoustic imaging technologies	30
3.4.1	Tomographic systems	31
3.4.2	Optical backward-mode detection	31
3.4.3	Microscopy	31
3.4.4	Intravascular catheters	32
3.4.5	Endoscopes	32
3.4.6	Flow cytometry	32
3.5	Implementations	33
3.5.1	A single detector small animal MSOT system	33
3.5.2	Real-time small animal MSOT system	35
3.6	Concluding remarks	37
4	Image Reconstruction	40
4.1	Introduction	40
4.2	Optoacoustic image reconstruction	40
4.2.1	Delay-and-sum and backprojection formula	41
4.2.2	Model-based inversion	41
4.2.3	An empirical comparison	43
4.3	Spectral unmixing	44
4.3.1	Linear spectral unmixing with known sources	44
4.3.2	Blind source separation	46
4.4	Light attenuation: effects and correction	47
4.4.1	A multispectral light diffusion tissue model	49
4.4.2	Results without fluence correction	50
4.4.3	Ratio normalisation	55
4.5	Concluding remarks	57
5	Sources of MSOT contrast	58
5.1	Introduction	58
5.2	Contrast in MSOT	58
5.3	Intrinsic tissue absorption	59
5.3.1	Hemoglobin contrast	59
5.3.2	Further tissue-intrinsic sources of MSOT contrast	61
5.4	Exogenous contrast agents	63
5.4.1	Activatable optical agents	70
5.5	Reporter genes	72
5.6	Concluding remarks	72

6	Tracking the fate of optical agents	74
6.1	Introduction	74
6.2	Materials and methods	75
6.2.1	Experimental protocol	75
6.2.2	Image reconstruction and quantification	76
6.3	Experimental results	76
6.3.1	Circulating ICG	76
6.3.2	Liver and gallbladder uptake of ICG	77
6.4	Kidney function	79
6.5	Concluding remarks	79
7	Cardiovascular imaging and disease	83
7.1	Introduction	83
7.2	Disease-relevant vascular imaging	84
7.2.1	Purpose	84
7.2.2	Method	85
7.2.3	Results	85
7.2.4	Discussion	85
7.3	Challenges of cardiac MSOT	87
7.3.1	Introduction	87
7.3.2	Optical attenuation through the mouse heart	87
7.3.3	Ultrasound attenuation in the thorax	88
7.3.4	Motion	89
7.4	Initial imaging of the heart	90
7.4.1	Imaging of the heart with full projection data	90
7.4.2	Real-time imaging of the heart	90
7.4.3	Multispectral imaging of the heart	91
7.5	Clustering for cardiac motion correction	93
7.5.1	Purpose	93
7.5.2	Method	93
7.5.3	Results	94
7.5.4	Discussion	96
7.6	Preclinical cardiovascular disease	98
7.6.1	Purpose	98
7.6.2	Method	99
7.6.3	Results	101
7.6.4	Discussion	103
7.7	Clinical potential	105
7.8	Concluding remarks	105
8	Imaging cancer	107
8.1	Introduction	107
8.2	Dynamic imaging of ICG perfusion in tumors	108
8.2.1	Purpose	108

8.2.2	Method	108
8.2.3	Results	109
8.2.4	Discussion	111
8.3	MSOT imaging of targeted agent distribution in tumors . . .	112
8.3.1	Purpose	112
8.3.2	Method	112
8.3.3	Results	113
8.3.4	Discussion	114
8.4	Imaging of long-circulating gold nanorods in tumors	115
8.4.1	Purpose	115
8.4.2	Method	115
8.4.3	Results	116
8.4.4	Discussion	119
8.5	Gold-enhanced liposomal nanocarriers	119
8.5.1	Purpose	119
8.5.2	Method	120
8.5.3	Results	121
8.5.4	Discussion	123
8.6	Concluding remarks	124
9	Conclusions and future directions	126
9.1	Conclusions	126
9.2	Towards clinical applications	133
A	Fluorescence cryoslicing imaging (FCSI)	134
	Bibliography	136
	Acknowledgements	147

List of Figures

1.1	A minimal MSOT imaging system	6
1.2	Absorption spectrum of Cy7	7
1.3	Schematic of the cylindrical phantom (top view)	7
1.4	MSOT phantom images	8
2.1	Extinction spectra of hemoglobin	14
2.2	Water absorption spectrum	14
2.3	Typical tissue scattering spectrum	15
2.4	Simulation of an optoacoustic source and resulting signal	18
3.1	Magnitude against frequency for signals from uniformly illuminated spherical sources	24
3.2	Originating image with two absorbers.	24
3.3	The optoacoustic signal from one projection angle	25
3.4	Effects of limited detection bandwidth	26
3.5	Sensitivity field of a focused ultrasound transducer	28
3.6	Directions in detection geometry	30
3.7	Block diagram of single transducer MSOT slice scanner	33
3.8	Small animal slice scanner	34
3.9	Mouse images using slice scanner	34
3.10	Artifacts caused by non-constant illumination	35
3.11	Block diagram of real-time small animal MSOT system	37
3.12	Real-time small animal system	38
3.13	Schematic of excitation and detection in real-time MSOT system	38
3.14	A single pulse image through the mouse liver	38
4.1	Steps in the MSOT image reconstruction flow.	41
4.2	Image reconstructions from simulated signals	44
4.3	Negative results using unconstrained least-squares for spectral unmixing	46
4.4	Normalised absorption spectra of hemoglobin and ICG	50
4.5	A multispectral tissue light diffusion simulation model	50
4.6	Absorption spectrum of uniform tissue model	51

4.7	Changes in fluence against wavelength with depth	52
4.8	Changes in initial pressure against wavelength with depth . .	53
4.9	Recovery of hemoglobin oxygen saturation with depth	54
4.10	Model with 3 ICG inclusions	54
4.11	Unmixing of ICG at varying depth	55
4.12	Unmixing of ICG at varying depth for 2 concentrations . . .	55
4.13	Ration normalisation of ICG unmixing results	56
5.1	Blood vessels in the liver of a mouse	59
5.2	Extinction spectra of hemoglobin and oxygenated hemoglobin	60
5.3	Blood oxygenation in veins and artery of a mouse tail	61
5.4	Extinction spectrum of eumelanin	62
5.5	Melanin in the skin of a mouse	62
5.6	Water absorption spectrum	63
5.7	Normalised absorption spectra of ICG and AuNR	67
5.8	Phantom imaging of ICG and AuNR	68
5.9	Detection of circulating gold nanorods	69
5.10	Activation of MMPsense 680 <i>in vitro</i> and detection by MSOT	71
6.1	Normalised absorption spectra of ICG and hemoglobin	75
6.2	Imaging circulating ICG	77
6.3	ICG being removed from the circulation	78
6.4	Imaging of ICG uptake in the liver	78
6.5	Optoacoustic images of the liver before and after ICG injection	79
6.6	Single-wavelength tracking of ICG entering the liver	80
6.7	ICG dynamics in liver and gallbladder	80
7.1	Transverse optoacoustic slices showing arteries in the upper thorax and neck	86
7.2	Determination of ultrasound attenuation through the rib cage	89
7.3	Optoacoustic image of the heart	90
7.4	Optoacoustic heart imaging	91
7.5	MSOT imaging of the heart	92
7.6	Single pulse optoacoustic images of the heart at 860nm exci- tation	95
7.7	Averaged images with and without clustering, taken at 860nm	96
7.8	Motion correction for unmixed deoxyhemoglobin contribution	97
7.9	Areas inside left ventricle after motion correction	97
7.10	Fluorescence showing integrin-targeted agent in excised mouse heart with infarct	99
7.11	Mouse with induced myocardial infarction	100
7.12	Anatomical features in a mouse model of myocardial infarction	102
7.13	Spectrum of dPGS	103
7.14	MSOT of targeted agent in the heart	104

7.15	MSOT reveals inflammation-targeted agent in a heart infarct	104
8.1	Dynamic imaging of ICG perfusion in a tumor	110
8.2	Hemoglobin distributions in tumor	111
8.3	MSOT of a targeted optical agent	114
8.4	Initial imaging of long-circulating gold nanorods in tumors . .	117
8.5	MSOT imaging of accumulation of AuNR in tumors	118
8.6	Optoacoustic image of liposome phantom	122
8.7	Absorption spectrum of gold nanorod-enhanced liposomes . .	122
8.8	Tumor imaging results with gold nanorod-enhanced liposomes	124
A.1	Labelled photograph of fluorescence cryoslicing imaging system	135
A.2	An example FCSI image.	135

Abbreviations

MSOT Multispectral optoacoustic tomography

CT Computed tomography

NIR Near infrared

NIRF Near infrared fluorescence

FWHM Full-width half-maximum

SNR Signal-to-noise ratio

PCA Principle component analysis

ICA Independent component analysis

ICG Indocyanine green

AuNR Gold nanorods

FMT Fluorescence molecular tomography

FCSI Fluorescence cryoslicing imaging

Chapter 1

Introduction

1.1 Why?

A quick look at data from the World Health Organisation tells us that over 17 million died of cardiovascular disease and over 7 million of cancer out of a total of around 56 million deaths world-wide [1]. That is approximately 30% and 13% respectively and far outweighs deaths by accidents, conflicts et cetera. Healthcare spending in developed countries commonly makes up 10% of GDP and is rising. For these reasons, there is a huge motivation for reducing mortality and simultaneously reducing costs. Suitable emerging imaging techniques can contribute in two major ways:

1. Drug discovery is a slow and enormously expensive process with a low success rate [2]. The costs are necessarily paid by healthcare systems and patients when successful drugs reach the market. By giving drug developers methods to see *in vivo*, early on, whether and how candidate drugs are working in animals models of disease, imaging can accelerate the development process towards success or failure by giving early answers to questions of efficacy and side-effects.
2. By allowing accurate and early diagnosis of disease in a clinical setting, imaging can enable earlier and generally less expensive and more effective treatment. Additionally, by monitoring the progress of treatment, imaging can allow early termination of treatments that are not working and replacement with other strategies.

What are the features of an imaging technique that has the potential to make an impact in these scenarios? First, it needs to produce meaningful images of critical biomarkers. (A biomarker is an indication of a particular biological state, such as a disease, which can be measured.) In this sense, it should

go beyond morphological imaging and provide information on biological processes linked to disease. Second, it should be economical enough to allow deployment on a sufficiently large scale to provide high-throughput imaging in pharmaceutical development as well as decentralised early diagnosis of patients. Last, it would be necessary, particularly in clinical scenarios, that the technique be safe for patients. A lack of ionising radiation would give it a significant advantage over X-ray CT or nuclear imaging. A belief that Multispectral Optoacoustic Tomography (MSOT) possesses these features has resulted in an accelerating research effort, of which this work is a part.

1.2 A brief introduction to MSOT

Optoacoustic imaging has emerged over the past several years as a highly promising modality for *in vivo* biomedical discovery and diagnostics. Based on the photoacoustic effect, tissue is excited by pulsed illumination. Energy deposited in optical absorbers within the tissue causes them to undergo thermal expansion, giving rise to broadband ultrasound waves that propagate outwards and can be detected noninvasively. By tomographic detection and inversion, the sources of the ultrasound signals, that is, the optical absorbers, can be resolved in space. The amplitude of the generated ultrasound waves is proportional to the amount of energy deposited, thus providing information about the optical absorption properties of the tissue. Generally, hemoglobin is one of the primary absorbers of light in tissue, meaning that optoacoustic imaging resolves blood and therefore vascular structures. Further light absorbers also give optoacoustic contrast and can be introduced exogenously, for example in the form of organic dyes or light-absorbing nanoparticles, which can be functionalised to highlight specific biological targets. Crucially, contrast originating from different absorbers must be separated so that signals from blood, for example, are not misinterpreted as coming from other sources. For this reason, Multispectral Optoacoustic Tomography (MSOT) uses multiple excitation wavelengths to identify sources of contrast according to their absorption spectra. This results in separate images of specific absorbers of interest, for example the different oxygenation states of hemoglobin, or exogenous optical agents.

1.3 Imaging today

1.3.1 The gaps in current biomedical imaging modalities

A number of unique imaging modalities are used in current biomedical practice. When imaging of anatomy is required, we largely have the choice

between simple X-ray imaging and its Computed Tomography (CT) form, Magnetic Resonance Imaging (MRI), which provides greater soft tissue contrast, and Ultrasound, which is relatively inexpensive and versatile. But imaging of structure alone does not give a complete picture. Nuclear imaging techniques like Positron Emission Tomography (PET) and Single Photon Emission Computed Tomography (SPECT) provide further information on biology, for example glucose metabolism with FDG-PET or myocardial perfusion imaging with SPECT. However, these methods have some drawbacks. Reliance on radioisotope-based tracers results in an exposure to ionising radiation and radioisotope decay may limit serial imaging possibilities. Decay also causes costly logistical problems: short-lived isotopes require on-site synthesis. Additionally, both PET and SPECT have significant acquisition times which limit their temporal resolution. Spatial resolutions in nuclear imaging are generally in the millimetre range, which is also limiting in certain applications. For all these reasons, optical imaging is an attractive option. It involves non-ionising radiation, imaging agents which are in routine use in a number of biological research settings (fluorochromes, for example in histopathology) and in many cases has a high sensitivity to hemoglobin, which enables the extraction of a multitude of functional measures. Macroscopic imaging becomes feasible by moving into the near-infrared (NIR) wavelength range, where tissue absorption is much lower than in the visible spectrum, enabling penetration depths measured in centimetres [3]. Optical tomography, for example, has proven capabilities in resolving fluorescent molecular probes in small animals [4] and intrinsic parameters such as hemoglobin concentration in human breasts [5]. However, such pure optical macroscopic approaches are limited by the scattering of light in tissue, as described in the next section.

1.3.2 Resolution versus penetration depth in optical imaging

The scattering of light is very strong in biological tissue, with typical reduced scattering coefficients in the visible and NIR wavelength range of $\mu'_s \sim 10\text{cm}^{-1}$ [6]. Therefore, at greater depths than about 1mm, photons entering tissue are diffusive, and the lack of directionality leads to rapid degradation of spatial resolution. For example, Fluorescence Molecular Tomography (FMT), a modality based on detection of diffuse light through whole small animals, achieves spatial resolutions in the order of 1mm at depths of approximately 1cm. In general, optical imaging attains high spatial resolution only near the tissue surface. Optoacoustic imaging provides a way around this problem of resolution degradation by optical scattering.

1.4 How MSOT works

1.4.1 The optoacoustic (photoacoustic) effect

The optoacoustic (or photoacoustic) effect, discovered by Alexander Graham Bell in 1880, is the generation of sound waves resulting from the absorption of light in materials. The light energy absorbed causes local heating and the resulting thermal expansion gives rise to pressure differentials. This results in pressure waves (sound) which propagate outwards. The amplitude of the photoacoustic signals generated depends on the amount of light energy absorbed. A more detailed discussion of the physical principles of optoacoustic signal generation and propagation can be found in chapter 2.

1.4.2 The development of biomedical optoacoustic imaging

Photoacoustic spectroscopy emerged in the 1970s as an application of the photoacoustic effect, primarily used in analytical chemistry [7]. Robert Kruger published the first paper in 1994 proposing the use of the photoacoustic effect in imaging optical absorption in a turbid medium, simulating biological tissue [8]. In that work, a Xenon flashlamp was used to excite a tissue-mimicking phantom, resolving an embedded absorber with a resolution of approximately 6mm. In the next years, interest in the technique grew, and experiments moved towards imaging of live specimens. In 2003, structural and functional imaging of hemoglobin in rat brains was demonstrated *in vivo* by Wang et al. [9]. The primary advantage of macroscopic optoacoustic imaging, when compared to purely optical techniques, is that the spatial resolution is not coupled to the scattering of light: ultrasound scattering is orders of magnitude lower in tissue and therefore allows the sources of absorption to be resolved with a high spatial resolution even though the excitation light is diffuse. At present, biomedical optoacoustic imaging is a fast-growing field of research.

1.4.3 Multispectral optoacoustic tomography

Clearly, imaging optical absorption at high resolutions with scattered light is an important achievement. However, the sources of absorption in biological tissue are many. Hemoglobin, whether oxygenated or not, absorbs light over a broad spectrum, and is found in a wide range of concentrations *in vivo*. Melanin is also a strong absorber of light. Introducing exogenous optical agents to the tissue provides new sources of contrast. So, in a single optoacoustic image, the contrast could be coming from a number of different intrinsic or exogenous sources, with no way of distinguishing them, and

therefore little value in studies of function or molecular biology. One common strategy, at least for exogenous agents, is to image the specimen before and after injection or accumulation of the agent, and assume that the agent is the only absorber to change concentration in the region of interest during the experiment. Examples of such approaches have been documented, a salient one being lymphatic mapping, because of the short times over which the contrast enhancement takes place [10]. However, over an extended period of time, obtaining the same image from a subject which moves and changes shape is challenging, to say the least. An example could be the imaging of a subcutaneous tumor in a mouse over a period of days. The tumor is soft, and moves with the skin: obtaining exactly the same image for comparison of different time points is impractical. Thus it is of utmost importance that we can obtain a signal specific to individual absorbers. The original application of the photoacoustic effect, that is, photoacoustic spectroscopy, suggests the method by which to achieve this: absorption can be measured multispectrally to distinguish specific absorbers of interest from one another. This is the aim of multispectral optoacoustic tomography (MSOT). While Kruger et al. suggested dual wavelength imaging and subsequent subtraction to resolve the presence of dyes over background absorption in 2003 [11], the method has a problem: in realistic tissue, the intrinsic absorbers, for example hemoglobin, do not display a flat spectrum which allows their absorption contributions to be cancelled out by subtraction. Even when the two wavelengths are chosen so that one is at the absorption peak of the dye, and the other at a minimum, the dye concentration still has to be strong enough that the change in signal between the two wavelengths is greater than that from hemoglobin. Note that hemoglobin can be present in tissue in very high and therefore strongly light absorbing concentrations.

The solution is to use more spectral information, and specifically resolve each significant absorber. Razansky et al. demonstrated this using a fluorescent dye embedded in an excised mouse leg in 2007 [12]. In 2008, Li et al. showed multispectral detection of an RGD-targeted optical probe *in vivo* [13]. Since then, interest in MSOT has grown as it becomes clear that that specific information on the sources of biological image contrast is essential.

1.4.4 A minimal MSOT imaging system

What is the simplest conceivable MSOT imaging system? For excitation, a pulsed laser with a pulse duration in the nanosecond range is most commonly used. For multispectral imaging, we need the wavelength to be tunable, so an optical parametric oscillator (OPO) or a some other mechanism for varying the wavelength is essential. To detect the ultrasound signals generated by the photoacoustic effect, some sort of ultrasound detector is necessary.

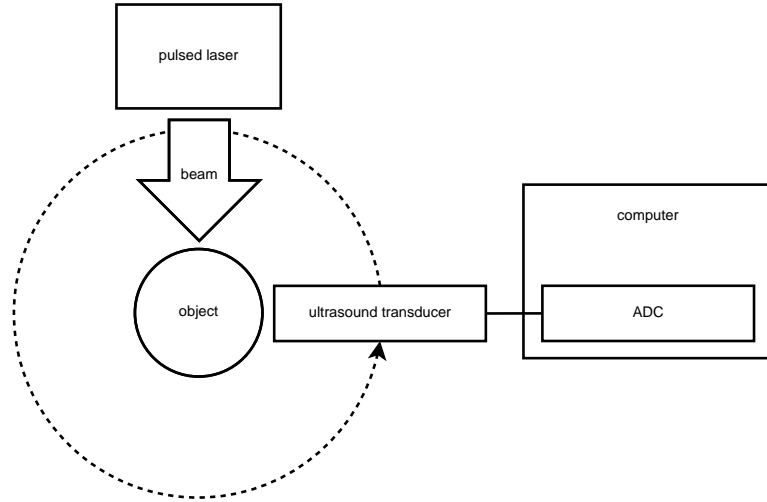


Figure 1.1: A minimal MSOT imaging system.

An analog-to-digital converter digitalises the signals and a computer is used to record them. Since we have to sample the ultrasound waves at multiple points in space to reconstruct a tomographic image, we need some mechanism to move the detector around. Once we've collected all these signals on the computer, we feed them into an image reconstruction algorithm to produce the image. To summarise, there are three main technical tasks in MSOT imaging: illumination, ultrasound detection and image reconstruction.

1.4.5 An introductory experiment

To provide a short introductory overview on how MSOT works in practice, I will briefly describe a simple phantom imaging experiment [14]. The goal is to produce an image of a specific organic dye, Cy7.

1.4.5.1 The phantom

The phantom measured in this experiment consists of a cylinder molded from agar, mixed with Intralipid (a fat emulsion) to produce a background scattering of $\mu'_s \approx 10\text{cm}^{-1}$. The phantom contains two cylindrical inclusions: one with a solution of Cy7 (at a concentration of $1\mu\text{M}$), the dye we want to resolve, and the other with a solution of black ink (absorption coefficient: $\mu_a \approx 0.5\text{cm}^{-1}$). (A schematic of the phantom is shown in figure 1.3.) Cy7 has an absorption spectrum with a characteristic peak at approximately 750nm, and a fast decrease to almost zero absorption from 800nm on (see

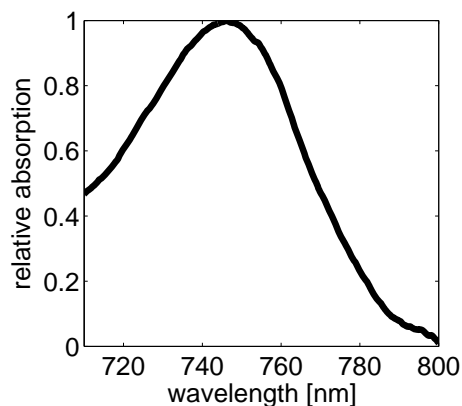


Figure 1.2: Absorption spectrum of Cy7.

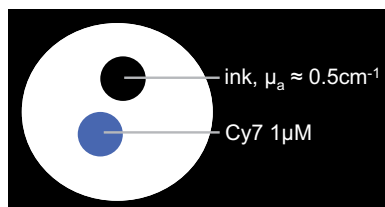


Figure 1.3: Schematic of the cylindrical phantom (top view)

measured spectrum in figure 1.2). In comparison, the absorption of the black ink stays approximately constant with varying wavelength.

1.4.5.2 Experimental method

After phantom preparation, the following experimental procedure was carried out. The phantom was measured in a system quite similar to that shown in figure 1.1. The excitation wavelengths started at 710nm and went up to 800nm in 10nm steps, that is, 10 wavelengths in total. For each of these wavelengths, the tomographic optoacoustic images were reconstructed and then spectral unmixing techniques were then applied to resolve the Cy7 from the multispectral image set. Details of these reconstruction methods will be presented in chapter 4.

1.4.5.3 Results

The resulting images are shown in figure 1.4, which can be compared to the phantom schematic in figure 1.3 for reference. Starting with the optoacoustic image at 750nm (figure 1.4a), you can see that contrast originates from

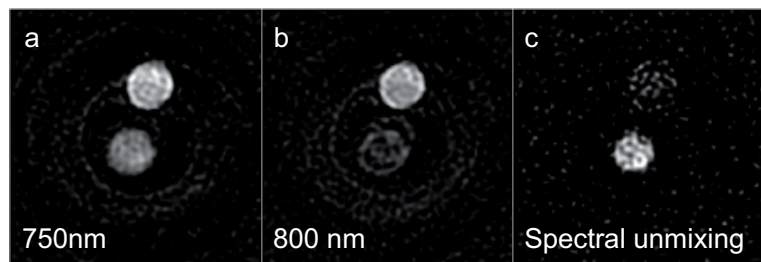


Figure 1.4: MSOT phantom images

the two inclusions, that is, from the ink and the Cy7. There is no significant contrast from the phantom background because it does not absorb light, and the photoacoustic effect depends on absorption. At 750nm the Cy7 is near its absorption peak and produces contrast almost as bright as the ink solution. At 800nm (figure 1.4b) the image changes: while the ink solution still produces similar contrast because of its flat spectrum, the Cy7 inclusion has almost disappeared, corresponding with its much reduced absorption at this wavelength. Finally, after fitting the multispectral data to the spectrum of Cy7 (spectral unmixing), we obtain the image shown in figure 1.4c, where the Cy7 inclusion is separated from other absorption contributions (ink), which is what we wanted in the first place. Thus, this simple example illustrated how MSOT can produce images of specific absorbers of interest, for example an organic dye, by identification of their unique spectral signatures.

1.5 The laboratory mouse

Laboratory mice provide scientists with an invaluable tool for basic research and drug discovery. Countless disease models for pathologies such as cancer [15], cardiovascular disease [16, 17] and others are well established. *In vivo* imaging of mice can be performed using X-ray CT, MRI, PET/SPECT, ultrasound and optical techniques ranging from simple planar NIR Fluorescence (NIRF) to tomographic approaches like FMT. In all of these modalities, specialised small animal imaging systems have been developed and are offered from multiple vendors. Developing MSOT for preclinical imaging of disease in mice enables the visualisation of optical contrast, and thus functional and molecular parameters, at high resolution through entire organisms *in vivo*.

1.6 Objectives of this research

The title of this thesis is *Multispectral optoacoustic tomography for imaging of disease biomarkers*, and it follows that the overall scientific objective is to investigate the ability of MSOT to enable the visualisation of biological indications of disease. A number of questions prompted this work, the first of which relate directly to instrumentation and reconstruction approaches:

- What defining characteristics does MSOT instrumentation require for practical imaging of biomarkers (see chapter 3)?
- To what extent are MSOT results quantitative? Which factors need to be taken into account (chapter 4)?

Concerning image contrast, a wide range of absorbers could potentially produce optoacoustic signals, including tissue-intrinsic chromophores and exogenous agents. The feasibility of MSOT detection of various absorbers must be understood in order to know how to approach specific biomedical imaging problems (see chapter 5).

The remaining objectives relate to requirements in *in vivo* biomedical imaging. First, in general dynamic imaging of optical agents (chapter 6):

- At what rate can MSOT image optical agents as their tissue distributions change?
- How can we extract meaningful metrics from MSOT data that allow us to characterise changes in agent concentrations over time?

Two of the major research fields in which biomedical imaging plays a key role are cardiovascular disease and cancer. In the field of small animal cardiovascular imaging (chapter 7):

- Is imaging of the arteries involved in mouse models of atherosclerosis by MSOT feasible?
- Is it possible to produce meaningful images of the heart?
- Can image blurring due to cardiac motion somehow be corrected for?
- Is the detection of exogenous agents, which could be used for molecular imaging, possible in the heart?
- Can MSOT be used to image heart disease, using appropriate mouse models?

For cancer imaging (chapter 8):

- What can we see in an MSOT image of a tumor? Is it possible to resolve tissue-intrinsic absorbers of interest (for example, hemoglobin) inside tumors?
- Is it feasible to detect exogenous agents (organic dyes, light-absorbing nanoparticles) throughout tumor masses?
- Can we visualise exogenous agents dynamically as they enter tumors using MSOT?
- What are the requirements for imaging drug delivery using MSOT?
- What advantages over currently employed modalities can MSOT bring to imaging of tumors?

1.7 An outline of this work

The chapters that follow serve first to describe the physical principles of optoacoustic imaging and establish an understanding of the technologies and methods developed and applied in this work on preclinical MSOT imaging (chapters 2 to 5), and then to present experimental results divided into relevant application areas (chapters 6 to 8). Theoretical background in the physics of pulsed optoacoustics with respect to deep-tissue imaging is presented in **chapter 2**. **Chapter 3** describes the instrumentation required for MSOT, and the key design considerations of such implementations. A brief survey of the various categories of optoacoustic imaging approaches reported in the literature is given, followed by a description of the instrumentation used for the work presented in this thesis. These systems were developed at the Institute for Biological and Medical Imaging (IBMI) by a group of several people, including myself. **Chapter 4** proceeds with an overview of the image reconstruction and processing methods that led to the successful imaging studies presented in the results. The methods discussed are a combination of established techniques found in the literature and newer methods developed at IBMI. All related simulations and analyses are original work, unless otherwise stated. **Chapter 5** discusses the contrast mechanism of MSOT and demonstrates detection of intrinsic tissue contrast as well as exogenous contrast agents. The remaining chapters present imaging results which consist entirely of original research I conducted with contributions from collaborators. Dynamic imaging of the kinetics and biodistribution of optical agents is investigated in **chapter 6**, showing, for the first time, the ability to track the kinetics of agents in various organs at a high rate

by MSOT. In **chapter 7**, results demonstrating MSOT imaging of the cardiovascular system and cardiovascular disease in mice are presented and discussed. A motion correction method for MSOT imaging of the beating heart is presented, yielding clear images of the mouse myocardium. Furthermore, this chapter shows a number of unprecedented imaging results: the first optoacoustic images of the carotid arteries and aortic arch in mice, the most detailed reported MSOT slices through the murine heart, and the first images showing a targeted agent resolved *in vivo* in a model of myocardial infarction. The imaging of cancer models by MSOT is the topic of **chapter 8**, which shows that MSOT provides unique visualisation of various important tumor parameters. More detailed cross-sections through tumors than those presented have never before been seen in optical imaging *in vivo*, and the first real-time MSOT visualisation of an optical agent entering a tumor as well as the first images characterising tumor nanoparticle accumulation in cross-sections are presented. **Chapter 9** presents conclusions from this work and a look into possible future directions of MSOT in an attempt to map a path from basic research to clinical imaging.

Chapter 2

The physics of pulsed optoacoustics

2.1 Introduction

The optoacoustic (or photoacoustic) effect is the generation of acoustic waves after the absorption of light energy. In this chapter, the physical background of pulsed optoacoustics is introduced, starting with a discussion of light propagation in biological tissue. The focus is on diffuse optics, which is relevant to the deep-tissue imaging presented in this thesis. The principles of optoacoustic signal generation are then introduced, followed by a discussion of optoacoustic wave propagation, which completes the process from optical excitation to acoustic detection.

2.2 Light propagation in biological tissue

The scattering of light in tissue is very strong: typical reduced scattering coefficients at visible and NIR wavelengths are in the range of $\mu'_s \sim 10\text{cm}^{-1}$ [6]. As a consequence, at depths beyond about 1mm, photons distributions can be modelled by a diffusion approximation of the radiative transport equation, which greatly simplifies the problem, as fluence is assumed to be isotropic. (In particular, scattering should be much greater than absorption for the diffusion approximation to be accurate.) Since this work is concerned with macroscopic imaging, discussion is limited to the so-called diffusive photon regime. In the diffusive regime, the relevant optical properties of tissue are the optical absorption coefficient μ_a , and the reduced scattering coefficient μ'_s , which can be thought of as an overall scattering measure after light has lost its directionality. It is defined as $\mu'_s = (1 - g)\mu_s$, where g is the

anisotropy factor and μ_s is the scattering coefficient. The time independent diffusion equation, relevant for pulsed optoacoustics, is then [18]:

$$-\nabla \cdot D\nabla\phi + \mu_a\phi = s_0, \quad (2.1)$$

where ϕ is the fluence (J/m^2), $D = 1/3(\mu_a + \mu'_s)$ is the diffusion coefficient and s_0 is a source term. An approximation which gives useful estimations on the attenuation of light under the broad illumination conditions commonly applied in macroscopic optoacoustic imaging, assumes plane wave illumination and defines an attenuation coefficient $\mu_{eff} = \sqrt{3\mu_a(\mu_a + \mu'_s)}$ which can be substituted into:

$$\phi(z) \approx \phi_0 e^{-\mu_{eff}z}, \quad (2.2)$$

where z is the penetration depth into tissue [18]. To get an idea of the rate at which light is attenuated with depth in realistic imaging scenarios, consider tissue with $\mu'_s = 10\text{cm}^{-1}$ and $\mu_a = 0.4\text{cm}^{-1}$ (values for murine liver region, at 732nm, from Niedre et al. [19]). In this case, $\mu_{eff} = 3.5\text{cm}^{-1}$, which means that the fluence at 1cm depth is only 3% of the incident fluence. We will see in the next section that optoacoustic signal amplitude is proportional to fluence, so we can expect that optoacoustic signals coming from deep tissue have amplitudes which are orders of magnitude smaller than those originating on the illuminated surface. This has implications for dynamic range, which needs to be large enough to detect surface signals and deep-tissue signals, as well as sensitivity, which must be sufficient for detecting small deep-tissue signals.

Note that the optical properties used in the example were valid for 732nm. Optical properties of tissue, especially absorption, vary with wavelength. The dominant absorbers of light in tissue are hemoglobin and water [3]. By inspection of the absorption spectra of hemoglobin (figure 2.1) and water (figure 2.2), we observe a wavelength region with relatively low absorption which is advantageous for optical imaging in deep tissue: hemoglobin absorption in the far red and near infrared is about 2 orders of magnitude less than in the shorter wavelength visible region; furthermore, the absorption coefficient of water, which is insignificant for much of the visible spectrum, rises to prohibitive values with longer near infrared wavelengths. For these reasons, the wavelength range from 650nm to 900nm is most commonly used for deep-tissue optical imaging, with occasional implementations at somewhat longer wavelengths.

The reduced scattering coefficient is frequently modelled as:

$$\mu'_s(\lambda) = A\lambda^{-b}, \quad (2.3)$$

where A , referred to as the scattering amplitude, depends on the concentration of scatterers, and $b > 0$, referred to as the scattering power, models the

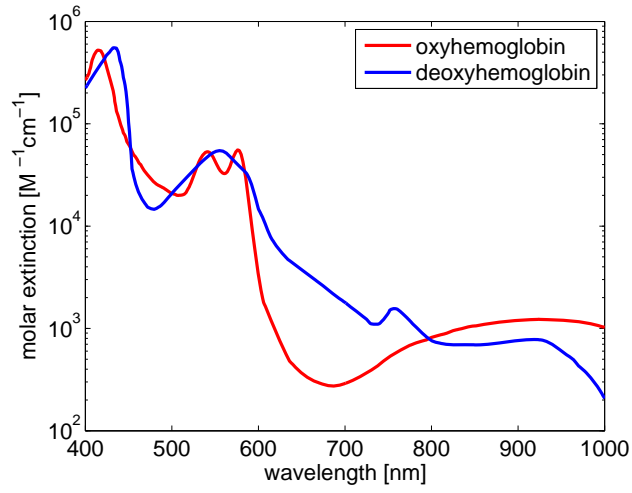


Figure 2.1: Extinction spectra of hemoglobin, showing much reduced absorption in the near-infrared. Data compiled by Scott Prahl, Oregon Medical Laser Center (<http://omlc.ogi.edu/spectra>), from multiple sources.

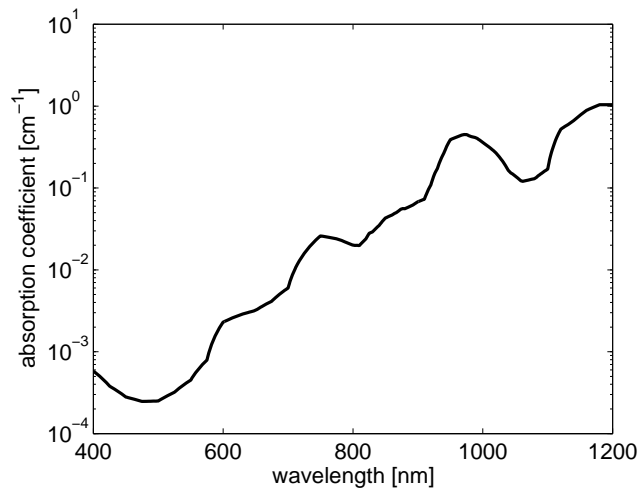


Figure 2.2: Water absorption spectrum. Data compiled by Scott Prahl, Oregon Medical Laser Center (<http://omlc.ogi.edu/spectra>) from [20].

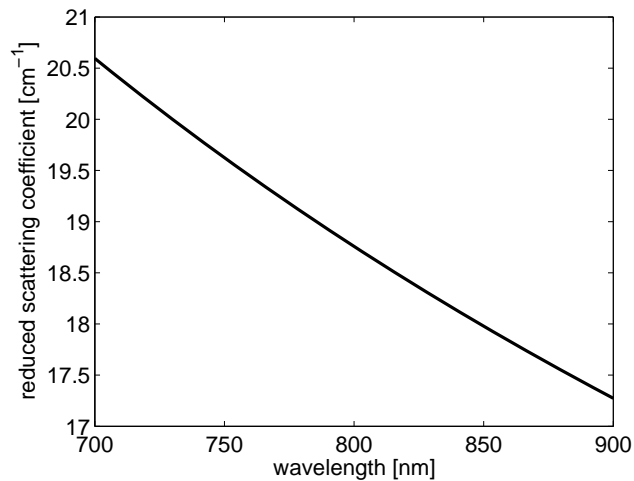


Figure 2.3: Typical tissue scattering spectrum.

decay in Mie scattering from different particle sizes with increasing wavelength [21, 22]. Reasonable values can be derived from the literature [19, 21]. As an example, if we use the values $A = 2020$ and $b = 0.7$ (for units of μ'_s in cm^{-1}), we obtain the curve shown in figure 2.3, which displays a typical, slowly decaying relationship between tissue scattering and wavelength.

2.3 Optoacoustic signal generation

Fundamentally, the optoacoustic effect as applied here can be understood as follows: incident photons from a pulse of light are absorbed by some matter. This absorbed energy, at least part of it, causes a local rise in temperature, that is, the matter is heated by the pulse. Thermal expansion is associated with the local temperature rise. The thermal expansion causes pressure, thus giving rise to acoustic waves propagating through the medium. The following equations are compiled and adapted from Li et al. [23] and Diebold et al. [24].

The energy $h(\mathbf{r})$ absorbed per volume during a pulse of length τ can be defined as:

$$h(\mathbf{r}) = \int_0^\tau \mu_a(\mathbf{r})\Phi(\mathbf{r}, t)dt = \mu_a(\mathbf{r})\phi(\mathbf{r}), \quad (2.4)$$

where $\Phi(\mathbf{r}, t)$ is the fluence rate ($\text{Js}^{-1}\text{m}^{-2}$) and $\phi(\mathbf{r})$ is the fluence (Jm^{-2}), at a point \mathbf{r} in space. Assuming that the pulse duration is short enough that changes during the pulse can be neglected (section 3.2.1 explains when this

is a reasonable assumption), then the local temperature rise is given by:

$$\Delta T = \frac{h}{\rho C_V}, \quad (2.5)$$

where h is the deposited energy, ρ is the density and C_V is the heat capacity at constant volume. The change in pressure due to this change in temperature is given by:

$$\Delta p = \frac{\beta \Delta T}{K_T}, \quad (2.6)$$

where β is the volume thermal expansivity (K^{-1}) and K_T is the isothermal compressibility (m^2/N). By substituting the change in temperature with equation 2.5, we obtain:

$$\Delta p = \frac{\beta h}{K_T \rho C_V}. \quad (2.7)$$

Using $v_s^2 = c_p / (K_T \rho C_V)$, where v_s is the speed of sound in the medium and c_p ($\text{JK}^{-1}\text{g}^{-1}$) is the specific heat at constant pressure, and defining $\Gamma = \beta v_s^2 / c_p$, we have:

$$\Delta p = \Gamma h, \quad (2.8)$$

with Γ a dimensionless constant representing the relevant thermodynamic properties of the absorber, referred to as the Grüneisen coefficient. By substitution of equation 2.4:

$$\Delta p = \Gamma \mu_a \phi, \quad (2.9)$$

which relates the change in pressure to the local optical absorption properties and local fluence. This pressure change is the initial condition that gives rise to (opto)acoustic waves propagating through the medium, and is the quantity that optoacoustic images visualise.

To obtain an estimate of realistic values for pressure and temperature increases in typical optoacoustic imaging scenarios, consider the excitation of oxygenated whole blood at 900nm. Assume a fluence of $50\text{mJ}/\text{cm}^2$: this represents the maximum permissible skin exposure (American National Standard for safe use of lasers, ANSI Z136.1-2007), so the calculation is relevant for a very superficial blood vessel. $\mu_a \approx 6.4\text{cm}^{-1}$, from known values for blood absorption. Using a value of $\Gamma = 0.25$ [23] in equation 2.9, we have: $\Delta p = 0.25 \times 6.4 \times 50 = 80\text{kPa}$. Now, using $K_T = 4.6 \times 10^{-10} \text{m}^2/\text{N}$ (value for water [25]) and $\beta = 4 \times 10^{-4}\text{K}^{-1}$ in equation 2.6, we have a temperature increase of: $\Delta T = 80 \times 10^3 \times 4.6 \times 10^{-10} / 4 \times 10^{-4} = 92\text{mK}$.

2.4 Optoacoustic wave propagation

By considering the change in pressure Δp as the initial condition $p_0(\mathbf{r})$ from which acoustic waves propagate, we can write the wave equation [24]:

$$(\nabla^2 - \frac{1}{v_s^2} \frac{\partial^2}{\partial t^2})p(\mathbf{r}, t) = -p_0(\mathbf{r}) \frac{d\partial(t)}{dt}, \quad (2.10)$$

where $p(\mathbf{r}, t)$ is the acoustic pressure wave at point \mathbf{r} , which is the quantity that can be measured using ultrasound detectors. Solutions for the pressure can be found using Green's functions, yielding [23]:

$$p(\mathbf{r}, t) = \frac{1}{4\pi v_s^2} \frac{\partial}{\partial t} \left[\frac{1}{v_s t} \int d\mathbf{r}' p_0(\mathbf{r}') \delta(t - \frac{|\mathbf{r} - \mathbf{r}'|}{v_s}) \right] \quad (2.11)$$

This means that if we place a detector at a certain position \mathbf{r} , then the pressure signal received will originate from a sphere with radius $v_s t$, which is intuitive since the acoustic wave propagates out from the sources to the detector at the speed of sound.

We can examine the expected pressure signals by simulation, in this case by applying an analytical solution to the governing wave equation. The simulation is performed on a plane (2D) for a circular absorber with a diameter of 2mm and a paraboloid absorption profile. The detector position is at a distance of 10mm away from the centre of the absorber. The simulation is summarised in figure 2.4. The simulated absorption profile (originating image) is shown in figure 2.4a. The time-resolved optoacoustic signal that results from the simulation is plotted in figure 2.4b. Note the bipolar nature of the signal. By changing the time axis to a distance axis (multiplying by the speed of sound), we can visualise this signal as a distance-resolved profile (figure 2.4c). From this signal, we observe that the bipolar signal starts 9mm from the detector and ends 11mm from the detector, as expected from the size of the absorber and the distance from the detector, that is, information about the spatial characteristics of the absorber are contained in the signal. Correspondingly, an absorber with a larger diameter would result in a wider bipolar signal, and a narrower absorber in a narrower signal. In frequency terms, we therefore expect larger features to produce lower signal frequencies and smaller features to produce higher frequencies.

2.5 Concluding remarks

The preceding chapter presented the relevant physical background concerning pulsed optoacoustic imaging. Diffuse optics was justified as a suitable approach for considering light propagation in biological tissue for deep-tissue

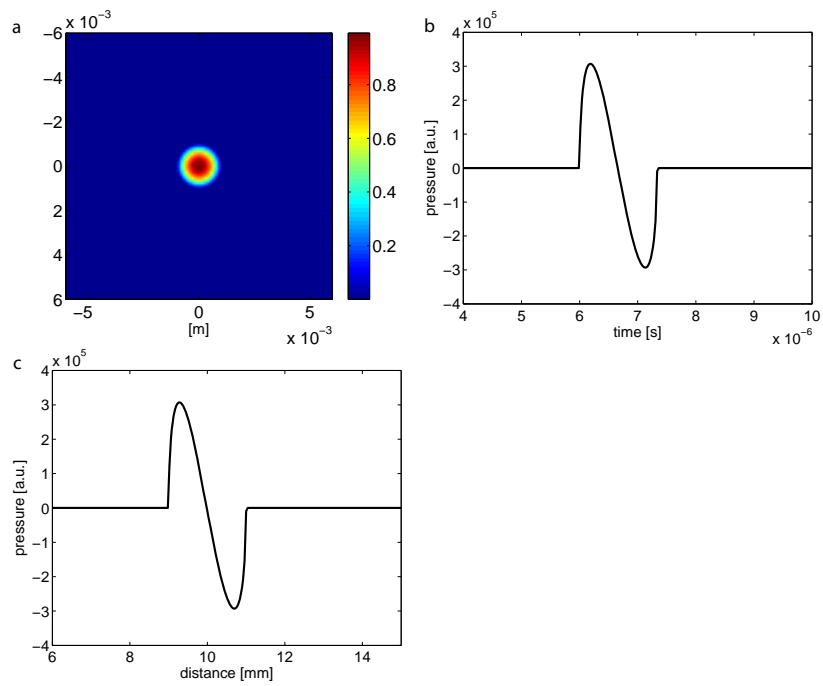


Figure 2.4: Simulation of an optoacoustic source and the resulting signal. a: Originating image, b: Resulting optoacoustic signal, c: The same optoacoustic signal plotted as a function of distance from the detector.

optoacoustic imaging, and the optical properties of tissue in the diffusive regime were introduced. The absorption spectrum of hemoglobin was shown to display a wavelength range of low absorption in the near infrared, presenting an opportunity for optical imaging in this range. The principles of optoacoustic signal generation were discussed, showing that the optoacoustic signal amplitude is proportional to the local light fluence and the local optical absorption. A look at optoacoustic signal propagation described the governing equations and presented some of the properties of optoacoustic signals: their bipolar nature and dependence on the dimensions of the signal sources. In the coming chapters, this foundation will be built upon to explain how the physical principles of optoacoustic imaging, and therefore MSOT, influence the design of suitable imaging instrumentation and image reconstruction techniques.

Chapter 3

Instrumentation

3.1 Introduction

This chapter describes the technical design considerations involved in MSOT imaging instrumentation. It starts with a discussion of the basic requirements for successful MSOT imaging. Since MSOT involves optical imaging and ultrasound, both illumination and ultrasound detection are discussed in turn. A survey of the different types of optoacoustic imaging systems reported in the literature follows. Finally, the instrumentation employed in this work is described, with a focus on the critical design characteristics.

3.2 Optical excitation

Although Xenon flashlamps were proposed for excitation in some of the pioneering work in biomedical optoacoustic imaging [8], the vast majority of implementations reported in the past years used pulsed lasers for excitation. The following sections discuss some of the physical requirements for optical excitation in MSOT imaging.

3.2.1 Pulse duration for thermal and stress confinement

As discussed in section 2.3, the principle of optoacoustic signal generation depends on the excitation pulse approximating a delta function. Since real pulses are finite in duration, some conditions should hold so that the governing equations are good approximations and signal generation is efficient. For one, the pulse duration should be short enough that thermal diffusion during the pulse can be ignored, a condition generally referred to as ther-

mal confinement. This holds for pulse durations $\tau < 1\mu\text{s}$ [26]. A further condition, stress confinement, states that the volume expansion of an absorber during the excitation pulse should be negligible, that is, $\tau < \tau_{st} = \frac{d_c}{v_s}$ where d_c is the characteristic dimension or targeted resolution [23]. For a resolution of $150\mu\text{m}$, this results in $\tau_{st} = 100\text{ns}$. In the work presented here, $t \approx 10\text{ns}$, as nanosecond pulsed lasers are employed.

3.2.2 Multiple excitation wavelengths

Multiple wavelengths are used to separate signals from different absorbers. Wavelength tunable sources are convenient for this. In particular, optical parametric oscillator (OPO) technology provides access to a wide range of wavelengths. For imaging anything deeper than approximately 1mm , the excitation light should be in the red or near infrared (NIR) wavelength range [3].

3.2.3 Maximum exposure

In order to prevent damage to tissue and enable translation into clinical settings, adherence to laser safety standards for skin exposure is desirable. An example is the American National Standard for safe use of lasers, ANSI Z136.1-2007. Permissible fluence values vary according to wavelength. For the NIR wavelength range most commonly used in whole-body small animal imaging, $700 - 900\text{nm}$, maximum permissible fluence values range from $20\text{mJ}/\text{cm}^2$ at 700nm to $50\text{mJ}/\text{cm}^2$ at 900nm according to the formula $20 \times 10^{\lambda-700/1000}$ [13]. The results I show in this thesis come from experiments where the fluence was kept below these maximum permissible exposure values.

3.2.4 Overall characteristics

Since the optoacoustic signal is proportional to the amount of energy deposited in the tissue, it makes sense to use a pulse energy which is as high as possible within the maximum exposure limits. Q-switched Nd:YAG lasers are capable of producing high energy pulses (pulse duration: $\tau \approx 10\text{ns}$) at $\lambda = 1064\text{nm}$. This can be frequency doubled to a wavelength of 532nm and fed into an OPO to give a tuning range in the NIR. Such illumination sources are part of the systems used in this work, described in 3.5.

3.3 Ultrasound signal detection

3.3.1 Detection technology

A wide range of ultrasound detection technologies exist, a result of decades of development for diagnostic ultrasound purposes. Most optoacoustic systems reported in the literature, and all measurements documented here, use piezoelectric detection, which also dominates diagnostic ultrasound devices. In particular, the piezoelectric ceramic lead-zirconate-titanate (PZT) is the most popular material in ultrasound arrays [27], because it combines durability, reasonable cost and good physical properties for the piezoelectric effect (high permittivity). Since PZT is poorly matched to the acoustic properties of tissue, composite materials are often preferred, where posts of PZT are embedded in a better-matched polymer material.

The frequency response of ultrasound transducers is commonly described in terms of centre frequency (MHz), and fractional bandwidth of centre frequency (%). Without going into the physical models used to describe transducers in practice, we can say that they are resonant devices and display strong frequency peaks. For example, the transducer array elements used in the system which will be described in section 3.5.2 have a centre frequency of 5MHz and a fractional bandwidth of the centre frequency of 57% (-6dB), which can be regarded as being in the typical range. That means that the spectrum of the transducer has -6dB points at 3.6MHz and 6.4MHz respectively. The next section on the properties of optoacoustic signals will clarify the limitations involved with this spectrum. New approaches to optoacoustic signal detection, based on optics, exploit the fact that no transmission of ultrasound is required, unlike in established diagnostic ultrasound imaging. Recently, several optical detectors have been reported [28, 29]. Such schemes are very promising for applications where small detectors are needed, for example in minimally-invasive imaging procedures, and possibly offer the opportunity of true backward-mode imaging if the detectors are made transparent to the excitation light.

3.3.2 Optoacoustic signals in the frequency domain

For the successful measurement of optoacoustic signals, it is necessary to understand their properties, which were investigated by Diebold et al. in 1991 [24]. The signal from a uniformly illuminated spherical source in the frequency domain is particularly informative since more complex structures can be considered as combinations of these. From [24], simplified for an acoustically matched case:

$$P(\hat{q}) = \frac{i\mu_a\beta\phi v_s a}{c_p(r/a)} \frac{[(\sin \hat{q} - \hat{q} \cos \hat{q})/\hat{q}^2] e^{-i\hat{q}\hat{\tau}}}{i \sin \hat{q} - \cos \hat{q}}, \quad (3.1)$$

where $P(\hat{q})$ is the pressure as a function of a dimensionless frequency $\hat{q} = \omega a/v_s$ and $\hat{\tau} = (v_s/a)[t - (r - a)/v_s]$ is the dimensionless time from the edge of the sphere. μ_a is the optical absorption coefficient, β is the thermal expansion coefficient, ϕ is the fluence, v_s is the speed of sound, a is the radius of the sphere, c_p is the specific heat and r is the distance from the origin.

Using equation 3.1 it is possible to investigate the frequency content of optoacoustic signals we expect to generate. For example, the signal generated from a spherical source with a diameter of 100 μm (a realistic approximation for a section through a blood vessel of that diameter) displays a peak in its spectrum at around 10MHz (see figure 3.1). The signal is generally broadband; the main lobe is between approximately 0MHz and 21.5MHz. Clearly, if the detection of features of such sizes is a priority, the ultrasound detector should be sensitive in this region. In the case of larger objects, the peak frequency becomes lower, as shown for a 500 μm diameter sphere where the peak is at 2MHz. Therefore, successfully imaging a wide range of feature sizes requires detection with a broad bandwidth, and, in general, transducers with central frequencies suited to the targeted feature sizes should be selected. Note that the main lobes of the spectra shown in figure 3.1 have fractional bandwidths of more than 100% of their centre frequencies: to put that into perspective, common PZT-based transducers have lower fractional bandwidths and can therefore only, at best, detect part of the main lobe with good sensitivity.

3.3.3 Consequences of narrow-band optoacoustic signal detection

By analytically simulating optoacoustic signals from a given absorption map, we can investigate the effects of narrow detection bandwidths on MSOT images. In our example, the originating image contains two circular absorbers of paraboloid absorption profile with diameters of 0.5mm and 5mm respectively (figure 3.2). The analytically derived optoacoustic signal for one projection is shown in figure 3.3a and the corresponding frequency domain representation in figure 3.3b. Note that each absorber produces a bipolar signal contribution with a width corresponding to the width of the absorber, as described in section 2.4. It follows then, from inspection of the time signals and from the frequency domain properties discussed in section 3.3.2, that each absorber contributes signals around a peak frequency dependent on its size. We can estimate these frequencies in this case: the $d = 0.5\text{mm}$

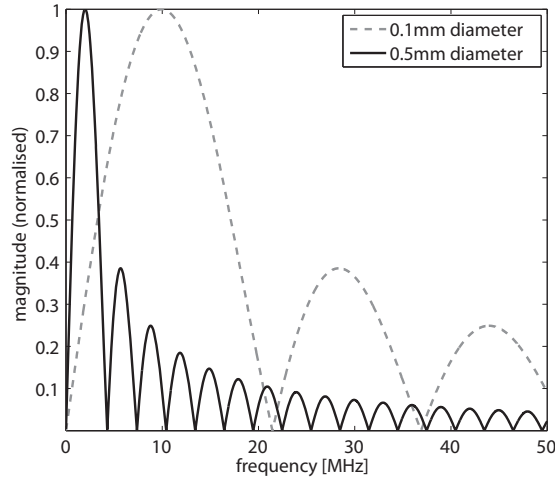


Figure 3.1: Magnitude against frequency for signals from uniformly illuminated spherical sources. Dashed: 0.1mm diameter sphere, solid: 0.5mm diameter sphere.

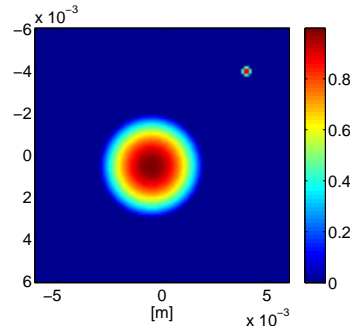


Figure 3.2: The originating image with two absorbers.

absorber will have a peak close to $\frac{v_s}{d} = \frac{1500}{5 \times 10^{-4}} = 3\text{MHz}$, whereas the larger absorber will have a peak near $\frac{1500}{5 \times 10^{-3}} = 300\text{kHz}$ (v_s is the speed of sound, d is the diameter of the absorber). The actual peak frequencies for each absorber, as seen on 3.3b, are slightly lower because the fundamental wavelength is broader than the objects, but our estimates are usefully close to the truth.

Now we consider the effects of limited detection bandwidth. Suppose that the large absorber represents an organ and the small absorber a blood vessel, and suppose that we want to be able to image them both. If we therefore select a transducer for detection with a central frequency of 1.5MHz, that is, near halfway between the peak frequencies emitted by the objects, the

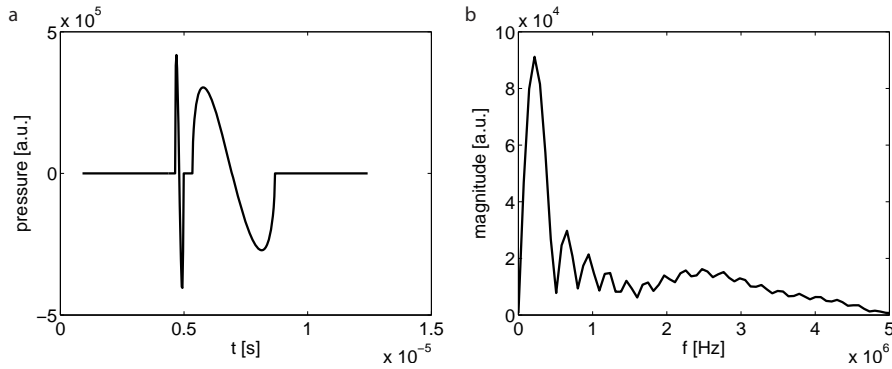


Figure 3.3: The optoacoustic signal from one projection angle. a: The time-resolved signal showing bipolar responses from each absorber. b: The same signal in the frequency domain.

transducer would need a fractional bandwidth approaching 200% to detect both peak frequencies within its -6dB band. Since such bandwidths are not typically available using PZT or piezocomposite transducers, this presents a major challenge. To illustrate the effects of insufficiently broadband detection, the transducer sensitivity spectrum is simulated by filtering the analytical signals produced in the example with third-order butterworth filters. A quantitative model-based algorithm is applied to reconstruct optoacoustic images from the signals, as will be described in more detail in section 4.2.2. Four different cases are considered. In the ideal case, no filtering was performed, that is, the simulated detector was capable of capturing all frequencies and the reconstructed image (figure 3.4a) is a faithful representation of the absorbers (figure 3.2). In the second case a low-pass filter with a -6dB frequency at 2.5MHz was applied. The reconstructed image (figure 3.4b) shows the large absorber, but the smaller absorber almost disappears because of the inability to detect its emitted frequencies. The third image was obtained after band-pass filtering with -6dB frequencies at 0.8MHz and 2.3MHz (figure 3.4c), a frequency range not suited to the dimensions of the imaged absorbers, which are both heavily suppressed in the resulting reconstruction. In the last case, a bandpass between 1.3MHz and 4MHz was applied to better capture the smaller absorber (figure 3.4d), and the larger absorber is hardly visible. On observing the resulting images it becomes clear that the detection spectrum of the transducer must be matched to the target feature sizes, and that conventional ultrasound transducers do not allow a wide range of feature sizes to be detected.

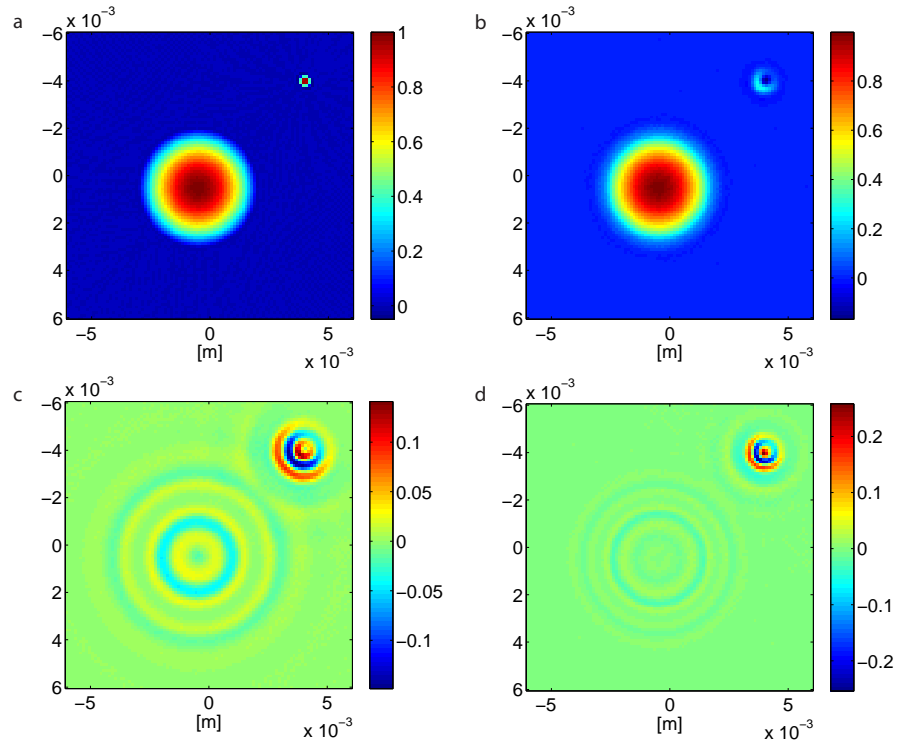


Figure 3.4: Effects of limited detection bandwidth. a: The image reconstructed without any signal filtering. b: Lowpass filter with -6 dB at 2.5 MHz. c: Bandpass between 0.8 MHz and 2.3 MHz. d: Bandpass between 1.3 MHz and 4 MHz.

3.3.4 Acoustic focusing

In terms of spatial dimensions, optoacoustic measurement systems can essentially be divided into three categories:

1. Spherically focused detection configurations where the detector can be considered to be focused on an elongated point, that is, along a line. The signal time provides the z or depth dimension and the x - and y -dimensions can be resolved by mechanically scanning the detector in a plane. This configuration is commonly used in optoacoustic microscopy [30]. A variation of this principle is optical resolution optoacoustic microscopy, where the lateral resolution is defined by the optical focus of the illumination beam [31]. Only one dimension (z) can be resolved from a single pulse. Fast image acquisition requires accelerated mechanical scanning of the detector.
2. Cylindrically focused detection configurations, which aim to detect signals originating from a plane, or slice through the tissue, for each illumination pulse. Multiple projections are required to reconstruct a slice image. The most common implementation of this principle involves scanning a detector in a circle around the object [9, 32], or placing multiple detectors on an arc [33, 34]. Different slices can be imaged separately by scanning the detector in the elevation direction. This principle is used for all the results I present in the chapters that follow.
3. Unfocused detection configurations that extend the previous measurement principle to the third spatial dimension, that is, unfocused detectors are used to measure signals originating from a three-dimensional region. The images are then reconstructed in 3D. This requires spatial sampling, that is, detector positions in all three dimensions. Implementations commonly involve mechanical scanning of detector arrays [35, 11, 36]. Attempts to generate an entire 3D image of reasonable resolution from a single laser pulse would require a large amount of detectors, which could become expensive.

I present the following experimental results in order to illustrate the effects of focused ultrasound detection on spatial resolution. The transducer under investigation was spherically focused (curved face) with a circular active surface of 13mm diameter, a focal length of 2.54cm and a central frequency of 10MHz (V311, Panametrics). The sensitivity field was measured by generating broadband optoacoustic signals using a focused beam illuminating a thin carbon rod. The transducer was translated through a grid on an plane. At each point on the grid, the frequency spectrum of the measured

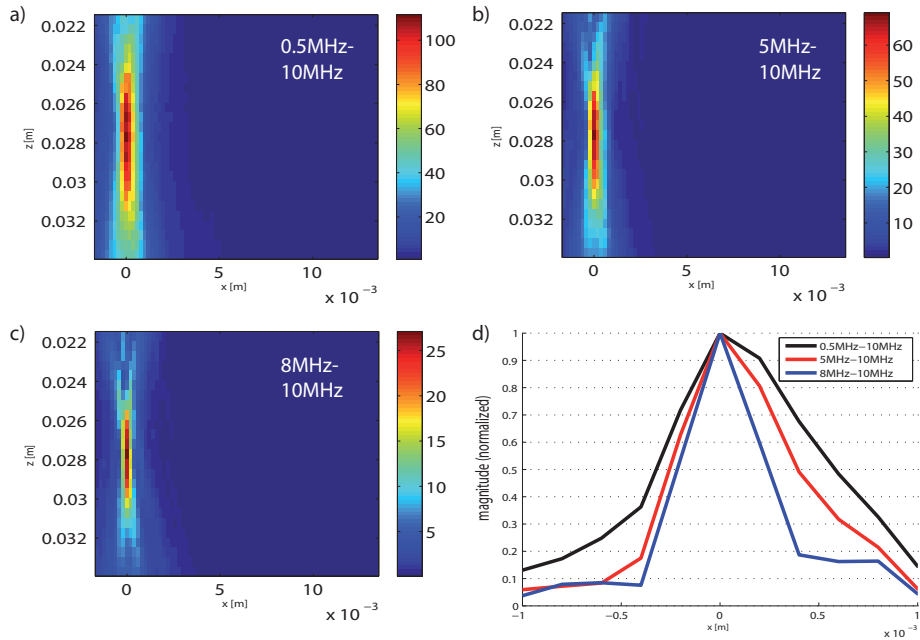


Figure 3.5: Sensitivity field of a focused ultrasound transducer for 3 selected frequency ranges.

signal was calculated. As expected, the beam width increases with decreasing frequency (see equation 3.4 or Szabo's book [27] for details). Consider an optoacoustic imaging system using such a focusing configuration to reject signals from outside the focus. As seen in section 3.3.2, optoacoustic signals are broadband in nature, especially when imaging structures of varying scale. Clearly, the detection should then be as broadband as possible. Figure 3.5 shows results from the transducer characterisation experiments. To illustrate how the sensitivity field changes with frequency, I have included the field for 3 ranges: 0.5MHz - 10MHz (figure 3.5a), 5MHz - 10MHz (figure 3.5b) and 8MHz - 10MHz (figure 3.5c). These represent optoacoustic imaging scenarios where the measured signals have been bandpass filtered to these ranges. Taking a cut through the fields at the focus, we obtain full-width half-maximum values for the beam width of $900\mu\text{m}$, $650\mu\text{m}$ and $475\mu\text{m}$ respectively. Now consider the implications this has on an imaging system: the resolution of focused dimensions degrades as an increasing amount of lower frequencies are included in the data, and is not easily defined. Nevertheless, the only way to avoid using detector focus-defined resolution in deep tissues is to sufficiently sample the acoustic field in all three spatial dimensions and reconstruct in 3D. Since this has high costs in terms of number of detectors or time used in scanning detectors in 3D, it seems that focused detection, at least in one spatial dimension, is a worthwhile compromise.

3.3.5 Spatial resolution

The detection geometries applied in this work use mechanical focusing in the elevational direction and rotational scanning or curved arrays around the imaging plane to produce one 2D slice at a time. In such an implementation, there are three different axes with respect to spatial resolution: the elevational resolution, the axial resolution and the lateral resolution. Figure 3.6 defines the directions of these resolution axes.

The axial resolution is dependent on the cut-off frequency of the detector. This is intuitive, since optoacoustic signals have widths in the time-domain corresponding to the size of the source (see section 2.4), meaning that smaller sources produce narrower signals with higher frequency content, which require detectors sensitive to those frequencies. Xu et al. [37] derived an expression to estimate the axial resolution, defined by the full-width half-maximum (FWHM) of the point spread function:

$$R_{ax} \approx \frac{0.8v_s}{f_c}, \quad (3.2)$$

where v_s is the speed of sound and f_c is the detector cut-off frequency. While this is a robust definition of the resolution, it should be noted that the actual resolution in an optoacoustic image depends on whether the absolute sensitivity of the detector at a given frequency is high enough to detect the relevant signals.

In our case of circular scanning or curved arrays, the lateral resolution can be estimated by the expression (again from Xu et al. [37]):

$$R_{lat}(r) \approx \frac{Dr}{r_0}, \quad (3.3)$$

where r is the distance between the optoacoustic source and the centre of rotation, r_0 is the radius of the detection circle, and D is the diameter of the detector. This means that the lateral resolution degrades towards the width of the detection surface with sources moving away from the image centre, which is intuitive: a concentric circle with a smaller radius has its circumference more finely sampled than one with a larger radius. Note that this expression is specific to circular geometries. In the case of linear scanning or linear arrays, the lateral resolution would not vary with distance, but rather be fixed to the detector diameter. Hence we can see that the principal benefit of curved arrays or circular scanning is a potential improvement in the lateral resolution.

The elevational resolution is dependent on the focusing of the detector, as discussed in section 3.3.4. From Szabo [27], we can estimate the elevational

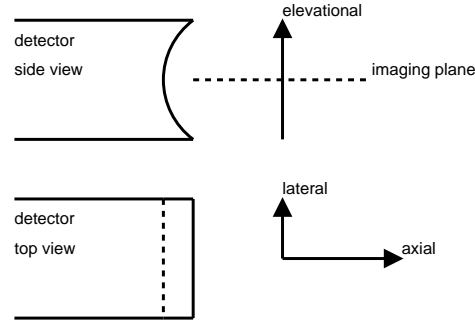


Figure 3.6: Directions in detection geometry. The elevational direction is perpendicular to the imaging plane. The axial and lateral directional are in the imaging plane, where the axial direction is perpendicular to the detector surface and the lateral direction is parallel to the detector surface.

resolution at the focal point by:

$$R_{el} \approx 1.02 \frac{F v_s}{f D_e}, \quad (3.4)$$

where F is the focal distance of the detector and D_e is the detector diameter in elevational direction. This expression is dependent on the frequency f : as discussed in section 3.3.4, the focusing becomes tighter with increasing frequency. The geometrical parameter influencing the elevational resolution is F/D_e , so decreasing the focal distance or increasing the size of the detectors can improve the resolution, however, this comes at the cost of depth of field, since shortening the focal distance will also shorten the focal zone [27].

In summary, the axial resolution of an optoacoustic imaging system depends on the detection cut-off frequency. The lateral resolution depends on the detection geometry, the detector width, and, in the case of circular spatial sampling, the distance from the centre. The elevational resolution in our case depends on the focusing of the detector. In section 3.5.2, the expressions discussed here will be applied to estimate the spatial resolution of the primary MSOT system employed in this work.

3.4 Optoacoustic imaging technologies

In the following sections I will give a overview of the various types of *in vivo* optoacoustic imaging systems that can be found in the literature.

3.4.1 Tomographic systems

Tomographic optoacoustic imaging systems generally rely on sampling the acoustic field in space and then applying an inversion scheme to reconstruct volumetric images. Implementations either rely on scanning single detectors [9, 32], using fixed, multi-element detection arrays [33, 34, 38], or a combination of scanning and multi-element detection [11, 35]. Such systems, depending on geometry, either scan one 2D slice at a time using cylindrically focused detection, or produce 3D volumes, which requires sufficient sampling in all spatial dimensions and therefore either a greater amount of detectors or a longer mechanical scanning time. While the vast majority of reported results from such imaging systems are of small animals, some preliminary examples of studies on human subjects can be found [36, 39].

3.4.2 Optical backward-mode detection

A highly original approach to optoacoustic imaging uses a Fabry-Perot interferometer film that is transparent to excitation light pulses, enabling illumination and detection to conveniently come from the same angle [40]. High quality 3D images result from a broad detection bandwidth and dense spatial sampling. The lack of parallelism in this approach, where an interrogation beam must be scanned over the film to obtain signals from individual sample points, results in disadvantageous acquisition times reported at 15 minutes for single wavelength images.

3.4.3 Microscopy

Optoacoustic microscopy systems produce high resolution images close to the skin surface. There are two major approaches. Optical resolution optoacoustic microscopy, where focused excitation light governs the lateral resolution, has been reported with diffraction limited optical resolutions of less than $1\mu\text{m}$ [41]. Since the resolution obtained depends on the focussing of light, the imaging depth is comparable to laser scanning microscopy (generally less than 1mm [6]) and the commonly cited advantage of optoacoustic imaging, that resolution does not degrade as fast with depth as in pure optical imaging, no longer applies. However, the natural sensitivity of optoacoustic imaging to hemoglobin is still considered sufficiently advantageous to make optical resolution optoacoustic microscopy a worthwhile pursuit. The second approach to optoacoustic microscopy is the use of strongly focused ultrasound detectors to produce images with acoustically governed resolution, that is, without the need for tightly focussed light and therefore attaining a slightly greater penetration depth. An example of such a system has been

reported capable of imaging at depths greater than 1mm and resolutions measured in tens of microns [30]. The chromophores typically visualised by optoacoustic microscopy are oxy- and deoxyhemoglobin as well as melanin, pointing to applications in imaging of functional parameters of melanoma and other skin tumors. Ophthalmic angiography is a further potential application area: contrast-rich images from small animals were reported in 2010 by Hu et al. [42] and Jiao et al. [43].

3.4.4 Intravascular catheters

Early detection and accurate characterisation of atherosclerotic plaques remains one of the primary challenges in imaging [44]. Since optoacoustic signals can reveal the composition of tissues by spectral analysis, a significant effort has been invested in the development of intravascular optoacoustic catheter systems to probe atherosclerotic plaques. The most common approach here is to add an optical fibre for excitation to an intravascular ultrasound (IVUS) system, which represents an established modality for plaque visualisation. This allows IVUS and optoacoustic imaging with the same catheter [45]. One notable development demonstrated the detection of lipid deposits in human coronary artery specimens by multispectral excitation around 1200nm, where lipids display an absorption peak [46]. Currently, reported acquisition times in tens of seconds in the absence of blood highlight the need for further technical improvements before this technology can be used in patients.

3.4.5 Endoscopes

As with catheter systems, optoacoustic endoscopes represent compact imaging systems for probing composition in minimally invasive procedures. Systems in early stages of development employing spinning illumination and ultrasound detection [47] or ring illumination and multi-element detection [48] have been reported.

3.4.6 Flow cytometry

Although *in vivo* optoacoustic flow cytometry is not, strictly speaking, imaging, it is a highly promising method that equally relies on optoacoustic signal generation and detection. In this technique, a superficial blood vessel is illuminated and cells labelled with a targeted optical agent cause optoacoustic signal spikes as they flow past the excitation/detection point. This has been demonstrated, for example, on circulating cancer cells by Galazha et al.

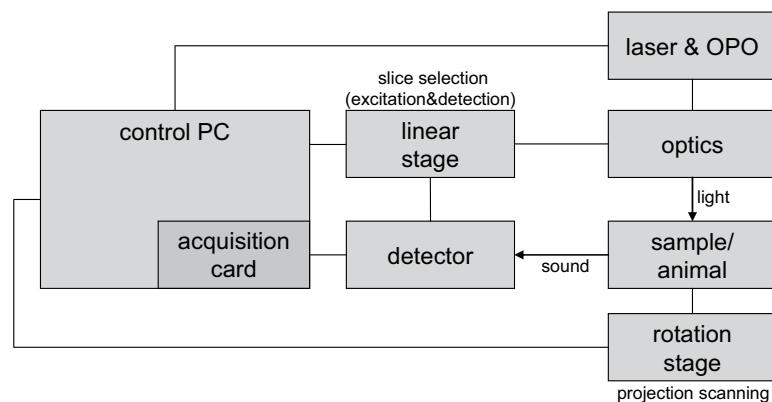


Figure 3.7: Block diagram of single transducer MSOT slice scanner.

in 2009 [49] and can be employed in a theranostic process for monitoring photothermal cell eradication [50].

3.5 Implementations

3.5.1 A single detector small animal MSOT system

An early MSOT implementation for flexible whole-body imaging of various small animals was described in 2009 by Rui Ma and myself et al. [32]. A block diagram of the system is shown in figure 3.7. The system consists of a small water chamber in which the animal is positioned on a rotation stage (see figure 3.8). A single, cylindrically focused ultrasound transducer is employed to detect the optoacoustic signals while the animal is rotated around 360° . This transducer, and the light, which illuminates the animal from two different angles, can be scanned in the elevation direction to enable imaging of selected transverse slices.

The system's acquisition time is reduced by recording signals while the animal rotates, instead of rotating to fixed angular projections and then recording signals. A variety of imaging experiments were performed using this system, including mouse imaging at multiple slices (figure 3.9). By comparing the optoacoustic images obtained (730nm excitation) with CT images using a blood contrast agent (eXIA 160, Binitio Biomedical), we were able to identify a number of anatomical structures, for example, veins in the neck and upper thorax, the heart, ribs and the spine. Other model organisms imaged in this system include zebrafish and drosophila pupae [32].

This implementation is not without limitations. Although the acquisition times are minimised by recording signals during rotation, thus utilising ev-

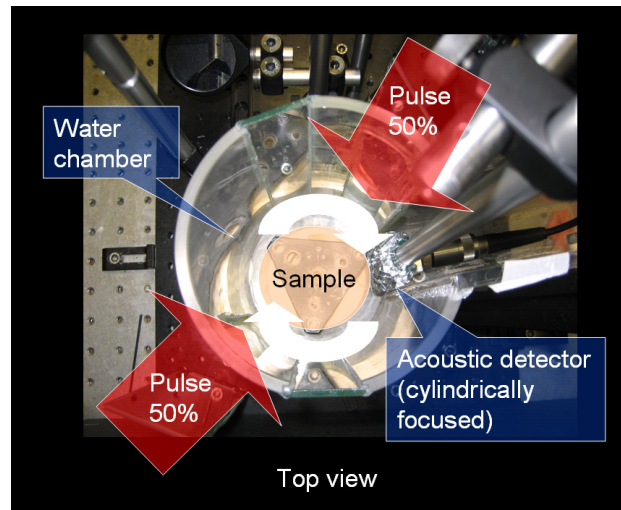


Figure 3.8: Small animal slice scanner.

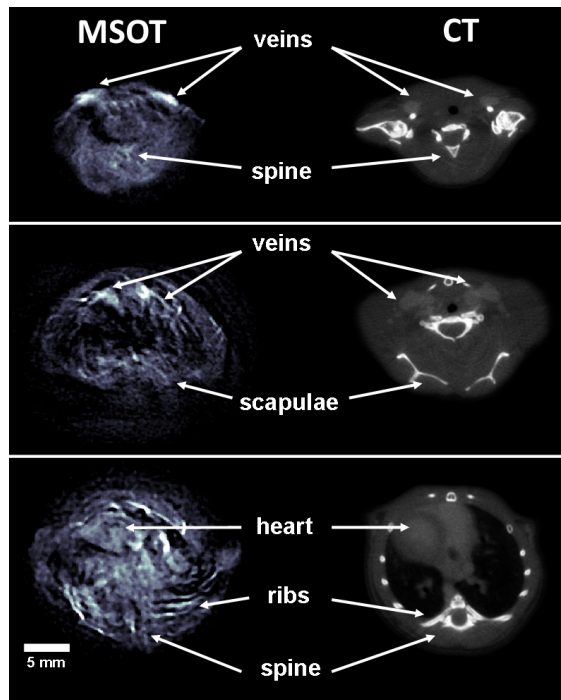


Figure 3.9: Mouse images using slice scanner. Left column: optoacoustic images, right column: X-Ray CT. Reproduced with permission [32].

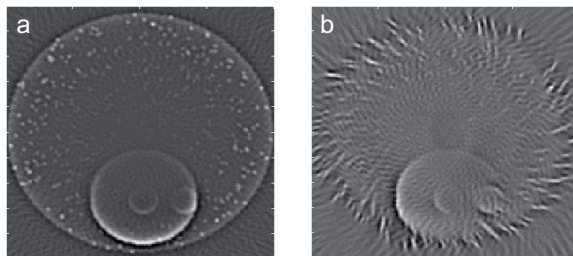


Figure 3.10: Artifacts caused by non-constant illumination. a: Simulated optoacoustic image of realistic tissue model for constant illumination. b: The same image under varying illumination.

ery excitation pulse, the single detector means that spatial sampling must be performed sequentially. In *in vivo* imaging scenarios, acquisition time is a critical parameter since fast changes in the biology of the animal require a high temporal resolution to properly measure. Clearly, moving to multi-element detection parallelises this spatial sampling and can therefore reduce acquisition time by a factor equal to the number of detector elements. Another limitation of this MSOT system is the illumination geometry. For tomographic reconstruction, the generated acoustic field, which is spatially sampled by varying the detector position, should remain the same for all projections. For this assumption to hold, the illumination should be kept constant, a reasonable condition when imaging small objects because the laser beams cover their surface approximately uniformly during rotation. However, when objects of the same diameter or larger than the laser beams are imaged, the illumination on their surface is not uniform and changes during rotation due to incomplete coverage of the object's circumference. This causes reconstruction artifacts. To verify the appearance of such artifacts in cases of projection-variant illumination, simulations were performed that closely modelled the illumination and detection geometry of the system. The results are illustrated in figure 3.10, where the difference between the ideal case of constant illumination (a) and varying illumination (b) is clear: severe smearing artifacts occur in the latter case. The artifacts are more pronounced around the edges of the object. This is intuitive: the diffusive nature of photon propagation evens out the illumination pattern after a few millimetres beyond the surface.

3.5.2 Real-time small animal MSOT system

Building on the success of the previous system, a subsequent implementation was developed to enable real-time slice imaging by parallel multi-element detection. A block diagram of the system is shown in figure 3.11, and the major

system components are shown in photographs in figure 3.12. As can be seen from the block diagram, the major improvement over the single detector system is that the need for rotational scanning of the animal falls away due to multi-element (multi-angle) ultrasound detection. While acquiring a transverse slice in the system described in 3.5.1 generally takes minutes, the parallelism of the multi-element system enables a full slice to be acquired from each laser pulse. Since the laser used for excitation has a pulse repetition frequency of 10Hz, this results in a frame-rate of 10 frames/s. The system was first described in 2010 in the context of dynamic imaging of kidneys by Buehler et al. [33] and imaging of cardiovascular structures by myself [34]. Excitation in the near infrared (700nm-950nm) is provided by a tunable optical parametric oscillator (OPO) pumped by an Nd:YAG laser (Opotek). In order to produce meaningful single-pulse images, the pulse energy should be as high as possible to ensure maximal SNR. In this case, the maximum pulse energy delivered by the OPO is approximately 100mJ (at 740nm). This allows the laser exposure on the skin to be kept just beneath maximum permissible values as is detailed in [34]. The laser pulse duration is below 10ns, which satisfies thermal confinement. The beam is coupled into a custom fibre bundle assembly (CeramOptic Industries). This assembly is divided from one bundle on the input (or laser) side to 10 output arms, which are positioned to illuminate the mouse from multiple angles on the imaging plane. A schematic of the excitation arrangement is provided in figure 3.13.

A custom-made piezocomposite ultrasonic transducer array (Imasonic SAS) with 64 elements and a central frequency of 5MHz and fractional bandwidth of 57% is used for detection. The elements are arranged in one row forming a spherical concave array covering 172° with a mechanical focal distance of 4cm. Each element has dimensions of 1.88mm (lateral) by 15mm (elevational) with an inter-element spacing of 0.1mm. The dimensions of the transducer array allow it to be considered as being cylindrically focused on one cross-sectional slice. A custom-built acquisition system with a total of 64 channels, a sampling rate of 40MSps and 12 bit digital resolution records the time-resolved optoacoustic signals. For coupling of the ultrasound signals, the transducer array and fibre bundle outputs are submerged in a water bath. Mice are placed in a horizontal position (prone or supine) in a holder with a thin polyethylene membrane so that there is no direct contact between water and the mouse. The laser beams and ultrasonic transducer array are in fixed positions, whereas the animal holder can be translated through the imaging plane using a linear stage (NRT 150/M, Thorlabs) so that any transverse slice through the mouse can be imaged. Unless otherwise stated, the MSOT imaging results presented in this thesis were generated using this real-time imaging system. An example *in vivo* image from the system is shown in figure 3.14: this image is generated from a single laser pulse, that

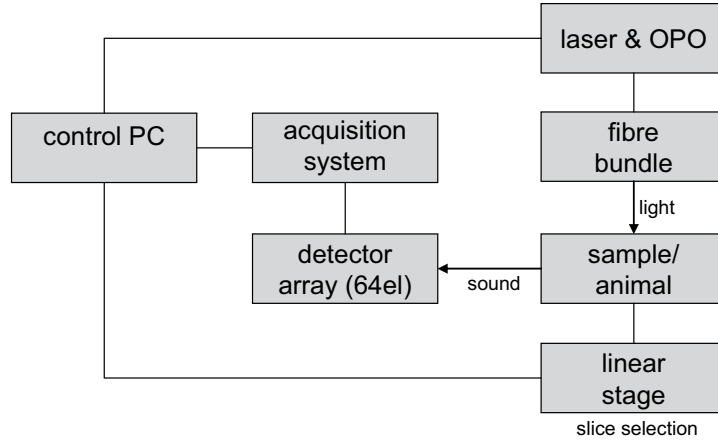


Figure 3.11: Block diagram of real-time small animal MSOT system.

is, the image acquisition time, based on the time it takes the ultrasound signals to reach the transducer array, is measured in tens of microseconds. Vasculature inside the liver is clearly visible.

Applying the expressions discussed in section 3.3.5, we can estimate the spatial resolution of the system as follows. Assuming a cut-off frequency $f_c = 6.4\text{MHz}$ (specified central frequency 5MHz , fractional bandwidth 57%), we apply equation 3.2 to estimate the axial resolution:

$$R_{ax} \approx \frac{0.8v_s}{f_c} = \frac{0.8 \times 1500}{6.4 \times 10^6} = 188\mu\text{m} \quad (3.5)$$

The lateral resolution depends on the distance from the optoacoustic source to the rotational centre of detection. A realistic worst case on the surface of a mouse of diameter 2cm results in sources 1cm from the centre. Applying equation 3.3 yields a worst case lateral resolution:

$$R_{lat}(r) \approx \frac{Dr}{r_0} = \frac{1.88 \times 1 \times 10^{-2}}{4 \times 10^{-2}} = 470\mu\text{m} \quad (3.6)$$

The elevational resolution depends on the focusing of the detector and the signal frequency. For the central frequency of 5MHz , the elevational resolution at focus can be estimated by applying equation 3.4:

$$R_{el} \approx 1.02 \frac{Fv_s}{fD_e} = 1.02 \times \frac{4 \times 10^{-2} \times 1500}{5 \times 10^6 \times 15} = 816\mu\text{m} \quad (3.7)$$

3.6 Concluding remarks

This chapter has given an overview of the critical design requirements and parameters in MSOT imaging instrumentation. Starting with optical excita-

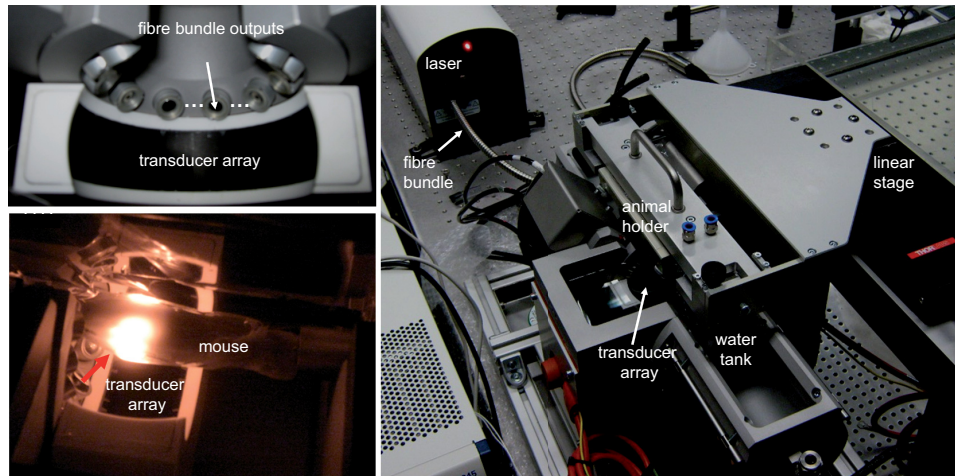


Figure 3.12: Labeled photographs of the real-time small animal MSOT system. Red arrow shows illumination path.

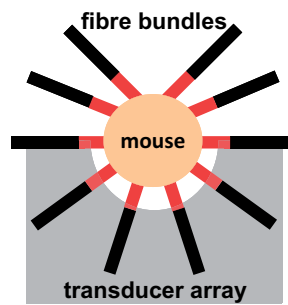


Figure 3.13: Schematic of excitation and detection in real-time MSOT system

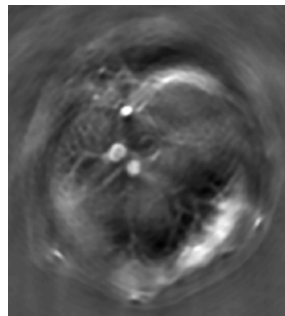


Figure 3.14: A single pulse image through the mouse liver at 850nm excitation.

tion, trading confinement conditions off against energy requirements points to the use of nanosecond pulsed lasers, which for multi-wavelength imaging should also be tunable in the NIR. Suitable ultrasound detection for MSOT should have a frequency response fitting to the targeted resolution and the dimensions of the features to be imaged. Broadband detectors produce higher fidelity images where features vary in size. One of the most important design decisions involves the focussing geometry of detection. Focusing can reduce the dimensionality of the imaging problem, but possibly at the cost of image fidelity. As described in the survey of optoacoustic imaging technologies, there is a wide range of implemented geometries and devices, each suited to particular applications, from surface microscopy, through endoscopy, all the way to deep-tissue noninvasive imaging. The particular implementations described and employed in this work were developed for whole-body small animal imaging. The approach taken is to illuminate the imaged volume and use cylindrically focused detection to capture signals from two-dimensional transverse slices through the animals. This trade-off allows real-time imaging of these slices with a manageable amount of detector elements (64 in the case described). Future developments might employ unfocused detection to reconstruct volumes in three dimensions in real-time, but the amount of detector elements needed to sufficiently sample the acoustic field without mechanical scanning would require significant additional financial investment. In the meantime, the two-dimensional approach yields meaningful images in real-time and allows mechanically practical devices, both for small animal imaging as presented here, or, potentially for future clinical devices based on hand-held ultrasound systems.

Chapter 4

Image Reconstruction

4.1 Introduction

This chapter deals with the methods required to convert optoacoustic measurement data into meaningful MSOT images. Figure 4.1 shows an overview of the steps involved in this process. The first step, image reconstruction, converts time-resolved optoacoustic signals into images. This step is performed per excitation wavelength, that is, each excitation wavelength results in one image. Image reconstruction algorithms are discussed in section 4.2. After reconstructing the single wavelength optoacoustic images, these results are combined and spectral unmixing is performed to resolve specific absorbers by means of their absorption spectra. This step is described in section 4.3. Finally, the effect of light attenuation and a simple approach for correcting it, referred to here as ratio normalisation, is discussed in section 4.4.

4.2 Optoacoustic image reconstruction

I refer to image reconstruction here as the procedure to obtain a single wavelength image from measured optoacoustic signals. Since all the work described in this thesis involves detection from a plane, or transverse slice (see chapter 3), I will restrict the discussion in this chapter to 2D tomography. The methods can generally be extended to the third dimension if necessary. For image reconstruction, two methods are considered here: delay-and-sum-type methods and a linear model-based inversion.

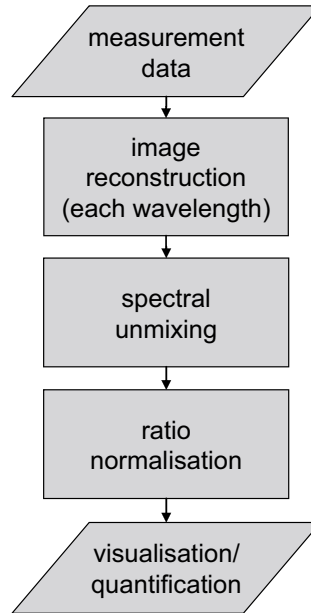


Figure 4.1: Steps in the MSOT image reconstruction flow.

4.2.1 Delay-and-sum and backprojection formula

Whether based on simple beamforming equations [51] or more rigorously derived analytical formulas [26, 52], a very common approach to reconstructing optoacoustic images boils down to summing signals onto a grid which maps the time-resolved signals to distances away from the detectors. This is accompanied by frequency filtering to more accurately approximate the originating image as well as model the detector frequency response. While some weighting factors to account for detection geometry have been proposed [51, 52] there is limited scope for taking complicated, non-uniform detector geometries into account in a holistic way. Additionally, despite efforts to derive exact analytical reconstruction algorithms, [52], results show inaccuracies due to idealised assumptions in their derivations [53]. The primary advantage of delay-and-sum type formulas is their relative simplicity and fast computation times.

4.2.2 Model-based inversion

A model-based optoacoustic image reconstruction method for 2D slice imaging was described by Rosenthal et al. in 2010 [53]. A model of optoacoustic signal propagation is built on a grid. This model can then be inverted and multiplied with the measured signals to give the optoacoustic image. More formally:

$$\mathbf{p} = \mathbf{M}\mathbf{z}, \quad (4.1)$$

where \mathbf{p} is a vector containing the measured optoacoustic signals, \mathbf{M} is the model matrix that describes the imaging system and optoacoustic generation and propagation, and \mathbf{z} is a vector containing the pixels of the originating image, which is the unknown to solve for. \mathbf{M} is calculated for a specific geometry by interpolating analytical solutions of integrals over arcs, which represent the time domain of the optoacoustic signals on the image grid. As with many simple problems in experimental linear algebra, the solution (image) is found by least squares:

$$\mathbf{z}_s = \underset{\mathbf{z}}{\operatorname{argmin}} \|\mathbf{p} - \mathbf{M}\mathbf{z}\|, \quad (4.2)$$

where \mathbf{z}_s is the solution image that minimises the square error. Commonly, the LSQR algorithm is employed to compute the image iteratively [54]. The advantage of the model-based approach is that the model can be adapted to account for non-ideal or non-uniform characteristics in the measurement system. A salient example of the necessity of such modelling is given in scenarios where the spatial sampling of the acoustic field is not uniform: Buehler et al. [55] applied a model-based approach to reconstruct images from such geometries. Since light needs to be delivered to the tissue from somewhere, such non-uniform detection geometries are likely simply for mechanical reasons, as gaps in detectors are needed to let light through. Another assumption in analytical formula-driven reconstructions is that the acoustic field is sampled at points. However, a realistic detector has a finite size, and to obtain adequate SNR, these diameters are often significantly wide. This has a negative effect on lateral resolution [37]. Rosenthal et al. [56] showed how a model incorporating finite-sized detectors could be used to recover lateral resolution. In time, it is highly likely that additional system characteristics will be included in models used for inversion, resulting in increasingly accurate images. A drawback of model-based approaches is, however, an increased computation time over simple analytical formulas. Modelling additional system characteristics further increases this time in many cases. The computation time should be considered to have two distinct parts: first, the model matrix is computed, then image reconstruction is performed by feeding the model matrix and the measurement data into an iterative algorithm. Since the model matrix depends on fixed system characteristics, it can be computed once and used repeatedly after that for reconstructions. The only caveat is that the speed of sound, a parameter of the model, varies with temperature, but this is advisable to keep to a controlled constant value in *in vivo* experiments in any case. Therefore, the reconstruction time for each image does not include the time taken for computing the model matrix.

4.2.3 An empirical comparison

I performed simulations to gain insight into the differences in performance between the image reconstruction algorithms described above. The simulated optoacoustic measurement data was obtained from an analytical solution of the governing wave equation. The simulations are on a plane (2D). The originating image consists of two round absorbers of diameter 2mm and 10mm respectively, inside which the absorption profile forms paraboloids (figure 4.2a). The absorbers have equal maximum values set to one. For the simulated (analytical) signals, the distance from the detector to the centre of the image was set to 10mm. All reconstructions were performed for 200-by-200 pixels and an image width of 12mm; the signal sampling frequency was set to three times the pixel frequency.

The reconstructed images are shown in figure 4.2b-d. The differences in the reconstruction results are clear. The model-based reconstruction (figure 4.2b) displays a faithful representation of the relative absorption values of the two objects, that is, the intensities remain equal to each other. The delay-and-sum reconstruction (figure 4.2c) appears to more heavily weight lower frequencies: the larger absorber is reconstructed with larger intensity. In contrast, the backprojection formula described by Xu et al. [52] produces a reconstruction (figure 4.2d) where the smaller absorber appears with a much higher intensity than the larger one, that is, high frequency signals are given too much weight. In conclusion, the model-based algorithm is capable of producing quantitative images, in theory, whereas simple delay-and-sum and the backprojection formula applied here are not. This, however, comes at a cost: on a standard PC, using Matlab code (The Mathworks), the processing times for model-based reconstruction were 88.8s for building the model matrix and 8.0s for reconstructing the image using LSQR. In contrast, reconstructing the image using the backprojection formula (and delay-and-sum) required 0.3s. Therefore, without using specialised reconstruction hardware, it appears that delay-and-sum type reconstructions are better suited for displaying images on systems during operation (real-time imaging), whereas model-based reconstructions can be used offline to obtain quantitative results. However, this was just a simulation. In reality, ultrasound detectors have a spectrum that is typically anything but flat (see section 3.3.1), and so different absorber dimensions will be weighted differently anyway. The situation is made worse by the reality of finite detector sizes. These physical characteristics have to be taken into account in order to obtain quantitative images from real measurement data, which is a subject of ongoing research [56].

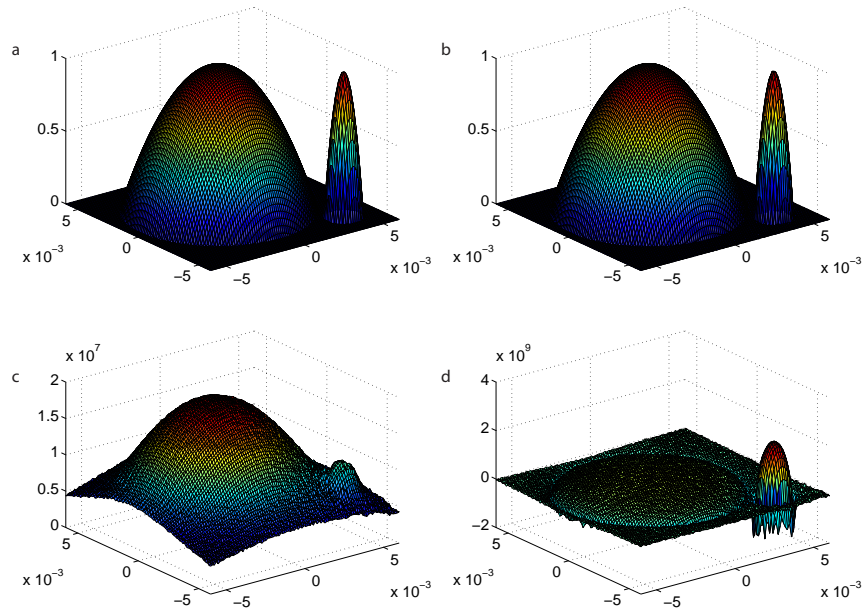


Figure 4.2: Image reconstructions from simulated signals. a: Originating image, b: Model-based reconstruction, c: delay-and-sum, d: backprojection formula. Spatial dimensions are in [m], intensity in [a.u.].

4.3 Spectral unmixing

Spectral unmixing is the process of converting the images, which each correspond to a specific excitation wavelength, into a new set of images where each one corresponds to the distribution of a specific absorber. Two approaches will be described in the following: linear spectral unmixing where the source absorption spectra are known in advance, and blind source separation where the source spectra are determined from the measurement data.

4.3.1 Linear spectral unmixing with known sources

This method works as follows: for each pixel in the image, the total measured optoacoustic spectrum is fitted to the known absorption spectra of the absorption sources expected to be present in the tissue. If a particular absorber makes significant signal contributions, its spectrum should be included, otherwise those contributions may be erroneously attributed to a different absorber. In a typical case, the included source spectra would be that of an exogenous contrast agent, and those of oxy- and deoxyhemoglobin, plus a flat (constant) spectrum to account for measurement offsets or spectrally

flat absorbers. The fitting is performed using least-squares on the set of linear equations resulting from the multispectral measurements (1 equation per excitation wavelength). The initial pressure distribution that underlies optoacoustic images is proportional to local light fluence in addition to the absorption properties, that is (from chapter 2):

$$p_0 \propto \phi \mu_a, \quad (4.3)$$

where p_0 denotes the initial pressure at a point in space, ϕ is the fluence and μ_a is the absorption coefficient. The equations used for spectral unmixing, for each pixel, are then of the form:

$$\phi \mu_a(\lambda_i) = \phi \sum_{j=1}^N \epsilon_j(\lambda_i) c_j, \quad (4.4)$$

where i is the wavelength, $\phi \mu_a(\lambda_i)$ is the optoacoustic response for that pixel, ϵ_j is the wavelength-dependent absorption coefficient per concentration for the absorber represented by the spectral component j , and c_j is the local concentration of that absorber. The unknown quantities solved for by least-squares are then ϕc_j for $j = 1..N$. Note that the images must be corrected for possible wavelength-dependent fluctuations in laser excitation energy, so that ϕ is independent of wavelength. Additionally, the wavelength-dependence of the fluence due to the absorption spectrum of the tissue should either be corrected for or assumed to be negligible if sufficiently near to the skin surface.

To give an impression of the size of a realistic problem, consider an example where 5 chromophores are unmixed with 10 measured wavelengths. This results in a set of 10 equations with 5 unknowns each, that is, a 10-by-5 matrix. Since the matrix is comparatively small, the Moore-Penrose pseudoinverse can easily be applied to find the solution giving the least square error.

4.3.1.1 Nonnegative least squares

The solution giving the least square error can be any linear combination of the input spectra, including negative concentrations, that is, applying inverted spectra. In the presence of measurement errors, this is a realistic pitfall of naively applying least-squares. Figure 4.3 illustrates this problem using *in vivo* imaging data. On the left is an MSOT image of a mouse with a subcutaneous tumor implanted on its back (visible towards bottom of image). The image is the result of unmixing for injected gold nanorods,

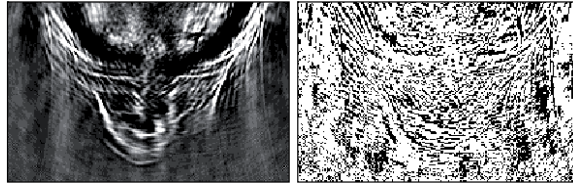


Figure 4.3: Negative results using unconstrained least-squares for spectral unmixing. left: Unmixed image of absorber distribution. right: Pixels in white indicate combinations of negative and positive spectra resulting from least squares fit.

a topic that will be revisited in chapter 8. What is relevant at this point is that the dataset was unmixed by linear spectral unmixing using four input spectra: that of injected gold nanoparticles, oxy- and dexoxyhemoglobin, and a constant spectrum. The image on the right indicates with white pixels where the unmixing resulted in a combination of positive and negative concentrations. Clearly, this is a significant portion of the image.

An intuitive approach to solving this problem is the use of a least-squares algorithm that constrains the solution to positive values. Such an algorithm is implemented in the standard Matlab (The MathWorks) function *lsqnonneg* [57], and was applied for linear spectral unmixing in the results presented in this thesis.

4.3.2 Blind source separation

Blind source separation, that is, spectral unmixing where the source spectra are unknown, was proposed for MSOT by Glatz et al. in 2011 [58]. There are two motivating factors behind this approach:

1. While we think we know that hemoglobin, in its different oxygenation states, and whatever agent we may have injected, are the only significant absorbers in tissue in the wavelength range of interest, there may be other unexpected absorbers contributing to image contrast.
2. Wavelength-dependent light attenuation, discussed in section 4.4, could distort the optoacoustic spectrum generated by absorbers, since the initial pressure is proportional to the local absorption coefficient *and* the local fluence (see equation 4.3).

Both cases are a problem in linear spectral unmixing with *known* sources because the unexpected or distorted signals would be fitted to combinations of the known input spectra. Blind unmixing approaches attempt to find the

significant spectral contributions from the measurement data itself. From Glatz et al. [58], the two proposed methods for blind spectral unmixing are principle component analysis (PCA) and independent component analysis (ICA).

Unmixing by PCA is based on the assumption that the spectral components are statistically uncorrelated. The result of PCA is a linear orthogonal transformation where components are in the order of largest variance. The method can be used for dimension reduction: when the number of excitation wavelengths exceeds the number of source spectra, the remainder of the components may represent noise which can be discarded. ICA, on the other hand, seeks a transformation into source spectra based on components having a maximum statistical independence.

While blind source separation has been reported to resolve unique absorber distributions with a superior SNR to linear spectral unmixing with known sources [58], there are situations where these methods cannot be robustly applied. For example, if the objective is to resolve oxy- and deoxyhemoglobin distribution or hemoglobin oxygen saturation, it is unlikely that either PCA or ICA will identify purely oxygenated or deoxygenated hemoglobin as the source spectra, but rather some combination of the two, since such combinations are likely to be present in the measurement data in higher amounts than the pure states. In general, depending on the imaging data, these approaches might combine or split spectra in unexpected ways. Both linear spectral unmixing with known source spectra, and blind spectral unmixing approaches have been applied in this work, as indicated with the relevant results, depending on which method best suits the given imaging scenario.

4.4 Light attenuation: effects and correction

As described in equation 4.3, the initial pressure distribution, and therefore the optoacoustic image intensity, is proportional to the amount of energy absorbed, which depends on the product of local absorption properties and the local light fluence. The ability to measure the absorption properties would yield powerful quantitative information about the composition of tissue. However, the light fluence, which also contributes to the optoacoustic signal amplitude, is variable and unknown, and therefore poses an obstacle to quantitative imaging of tissue composition. While the absolute value of the fluence is not needed to multispectrally determine absorber distributions, we can only cancel the fluence in the spectral unmixing equations if it does not vary. We can consider the fluence to vary in two ways:

1. The pulse energy from the excitation source almost certainly varies

with wavelength. In an OPO, for example, this wavelength-dependent variation is described by the tuning curve.

2. Light is attenuated as it propagates inwards from the tissue surface due to scattering and absorption. Thus there is a fluence distribution in each single wavelength optoacoustic image which generally falls off rapidly with penetration depth. Since tissue scattering and absorption properties vary with wavelength, the fluence distribution patterns are different for each wavelength.

The first variation is trivial to correct for: the excitation pulse energy should either have a sufficiently stable known wavelength dependence or should be measured in parallel to the imaging using a beam pickup approach or similar. For the results I present in this work, the following source normalisation was applied:

1. Prior to the measurements, the pulse energy was measured over a broad range of wavelengths using a commercial pyroelectric energy sensor to produce a tuning curve for the OPO.
2. To take account of wavelength-dependent absorption through the water path between the illumination outputs and the target, the tuning curve is divided by the attenuation through water (values taken from [20]). For the real-time MSOT system (section 3.5.2), the distance from the fibre bundle outputs to the mouse skin surface is approximately 3cm.
3. After image reconstruction, the images are corrected by dividing each single wavelength image by the corresponding value on the curve.

The second source of fluence variation presents a nontrivial obstacle to quantitative imaging. A variety of attempts have been made at solving this problem. Approaches involving the inversion of nonlinear models of simplified imaging scenarios appear frequently in the literature. A typical example of such an approach by Laufer et al. [40] claims a recovery of absolute chromophore concentrations within and outside of discrete tubes in a phantom with a computation time on a computing cluster of approximately 6 hours for 4 tubes. The practical utility of such methods, developed for simplified scenarios, remains doubtful. A unique method for recovering optical properties using a sparse signal representation was proposed by Rosenthal et al. in 2009 [59], providing a robust, data-driven route to extraction of quantitative information in optoacoustic tomography. The method assumes that optoacoustic images (initial pressure distributions) are composed of smooth fluence variations and sharp fluctuations in optical absorption, a realistic

assumption when considering the highly scattering nature of tissue. Despite the promise of this approach, its utility in the images presented in this work is limited by the lack of well-defined low frequency information resulting from the 2D focusing geometry (discussed in section 3.3.4) of the experimental imaging systems. The properties and implications of fluence variations are discussed in the following, as well as an approach to correct for fluence variations in some cases.

4.4.1 A multispectral light diffusion tissue model

To gain insight into the effects of light propagation in tissue on MSOT imaging, we need a model that is sufficiently realistic, but still as simple as possible, to capture the critical effects. I therefore employ a 2D finite element method (FEM) solver of the diffusion equation, which was developed for other diffuse optical imaging techniques [60]. The simulation model is based on the geometry of a circular mouse slice with a diameter of 2cm. For the wavelength-dependence of optical absorption, we assume that hemoglobin dominates absorption in the NIR wavelength range of interest to us. This allows us to use the well-known absorption spectra of oxy- and deoxyhemoglobin for our model (figure 4.4). We assume a background average tissue hemoglobin concentration of 210 μ M with an oxygen saturation of 70%, values derived from the literature for the mouse thorax [19]. Applying the model described in section 2.2, the values $A = 2020$ and $b = 0.7$ are used for scattering variation with wavelength, where the units of μ'_s are cm^{-1} , again, values derived from the literature [19, 21]. Overall, this gives us a model with wavelength-dependent absorption and scattering in the round shape of a mouse. To this we can add heterogeneities like models of blood vessels or dye inclusions as the application demands. Figure 4.5 shows an example of such a simulation. The modelled scattering is uniform throughout the slice. The distribution of the absorption coefficient, one of the inputs to the simulation, is shown for $\lambda = 790\text{nm}$ (figure 4.5a). Three features have been added to the background model to illustrate a potential simulation scenario: first, a hemoglobin inclusion of 6.4mm diameter with $\mu_a(790\text{nm}) \approx 0.8\text{cm}^{-1}$, to represent an organ of higher absorption than the background, for example, the heart in the thorax. A further hemoglobin inclusion with a diameter of 1.6mm, this time with 100% oxygen saturation and a concentration corresponding to whole blood, was added concentrically to the first inclusion, possibly representing blood inside a heart chamber. Last, an inclusion with a concentration of 200nM of indocyanine green (ICG, see spectrum in figure 4.4), a common organic dye, was placed on the edge of the first inclusion to represent an exogenous agent to be detected. The fluence distribution calculated by the FEM solution of the diffusion equation is shown in figure 4.5b. Note that the distribution is smooth despite the sharp absorption fea-

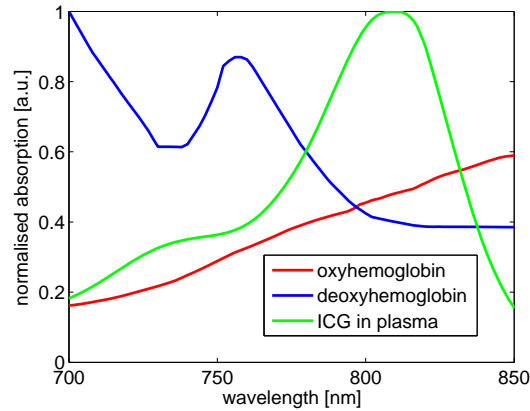


Figure 4.4: Normalised absorption spectra of hemoglobin and ICG. Data compiled by Scott Prahl, Oregon Medical Laser Center (<http://omlc.ogi.edu/spectra>), from multiple sources.

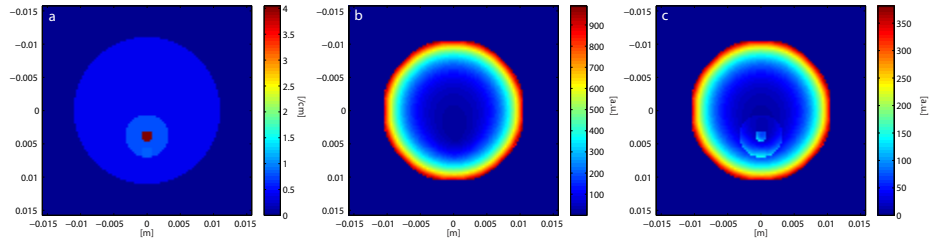


Figure 4.5: An example multispectral tissue light diffusion simulation model. a: μ_a at 790nm, b: the calculated fluence distribution, c: the calculated fluence distribution multiplied by μ_a to give the ideal optoacoustic image (initial pressure distribution).

tures, a typical property of solutions to diffusion equations. The image in figure 4.5c is the product of the previous two images, that is, the absorption coefficient multiplied by the fluence, which represents the ideal optoacoustic image (from equation 2.9 assuming variations of the Grüneisen coefficient can be neglected). Note that there is no noise added to the simulation data and detection is assumed ideal: the model’s only purpose is to show the influence that light attenuation has on MSOT results.

4.4.2 Results without fluence correction

There are cases in which no correction for the light attenuation in tissue is necessary for reasonably accurate quantitative results, for example, in relatively superficial structures that are broadly illuminated, so that the fluence

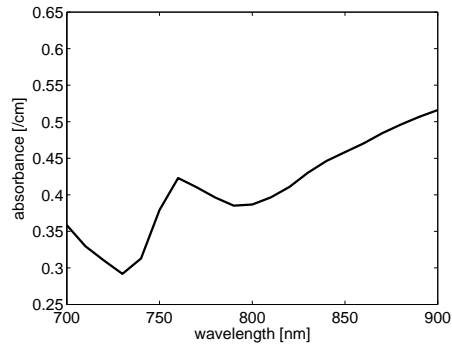


Figure 4.6: Absorption spectrum of uniform tissue model.

distribution can be considered as relatively constant. Convex subcutaneous tumors of millimetres in diameter are a further example. Clearly, the need for fluence correction also depends on how accurate or absolute the results should be. Relative quantification is less sensitive to incorrect assumptions on fluence than absolute quantification: a study by Maslov et al. shows, for example, that the hemoglobin oxygen saturation in subcutaneous blood vessels can be seriously affected by the wavelength dependence of fluence whereas the difference between neighbouring blood vessels is more robustly quantifiable [61].

Consider how the wavelength dependence of absorption and scattering produces different fluence attenuation for each wavelength. A look at the fluence per wavelength at different depths in a multispectral tissue model is revealing. We apply the 2cm diameter model from section 4.4.1 without any heterogeneity, that is, only the background. The absorption spectrum of the tissue (70% oxygen saturation) is shown in figure 4.6. Figure 4.7a plots the calculated fluence against wavelength from depths starting at the surface and ending in the centre (1cm depth). Overall, the fluence drops with depth. But not only does the overall fluence level decrease with depth, the differences over wavelength also become relatively greater. This is not immediately obvious from the absolute scale in figure 4.7a, but if we plot the fluence against wavelength at the surface relative to its maximum value, and do the same for a point in the centre, as in figure 4.7b, the difference is clear. While the values near the surface have minimal relative variation, the fluence at the centre displays a variation of over 60%. Notice how the wavelength-dependent fluence here closely resembles the inverted absorption spectrum of the simulated tissue (figure 4.6): the absorption is attenuating some wavelengths more than others.

To examine the effect this has on the resulting optoacoustic images, we multiply the fluence by the absorption coefficients to obtain the simulated

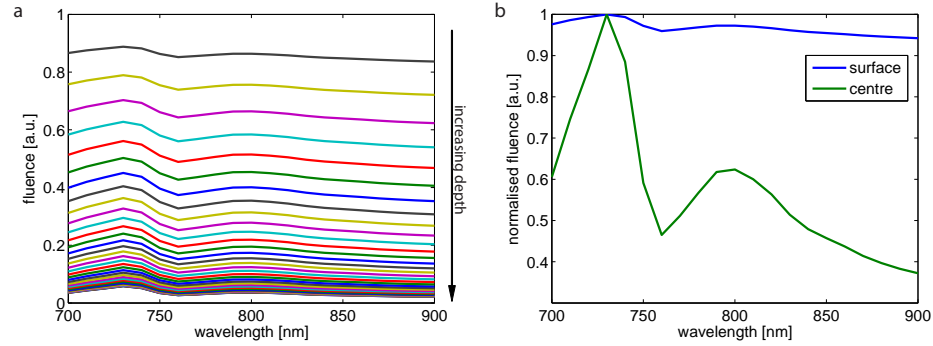


Figure 4.7: Changes in fluence against wavelength with depth. a: Fluence plotted against wavelength for each pixel in the uniform tissue model moving from the surface (top) to the centre (1cm, bottom). b: Fluence against wavelength normalised to respective maxima for the surface compared to the centre.

optoacoustic images (initial pressure distributions). When we then plot the initial pressure against wavelength for varying depths, we obtain the curves shown in figure 4.8. Figure 4.8a shows the curves for each pixel going from the surface into the centre of the circle. It is apparent that the optoacoustic signal at the surface correctly traces the expected absorption spectrum of the tissue (figure 4.6), however, with increasing depth, the spectrum becomes flatter as the fluence is increasingly affected by wavelength-dependent absorption. At some depth, the spectrum becomes inverted as the wavelength-dependent fluence dominates over the tissue absorption spectrum. To illustrate this more clearly, figure 4.8b compares the curves of initial pressure against wavelength for the surface and centre, where both curves have been normalised to their respective maxima. The curve from the centre is clearly inverted because of the wavelength-dependent fluence. Not properly correcting for this variation at such a depth (depending on the overall optical properties) could cause unreliable MSOT results.

An example of the effects on absorber quantification is given in figure 4.9, where the hemoglobin oxygen saturation is recovered from spectral unmixing results for the uniform tissue model. The formula used to calculate this value is:

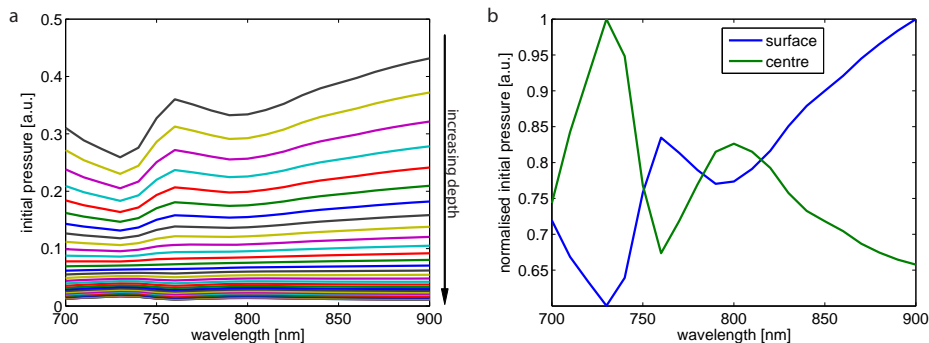


Figure 4.8: Changes in initial pressure (optoacoustic image intensity) against wavelength with depth. a: Initial pressure plotted against wavelength for each pixel in the uniform tissue model moving from the surface (top) to the centre (1cm, bottom). b: Initial pressure against wavelength normalised to respective maxima for the surface compared to the centre.

$$S_{O_2} = \frac{HbO_2}{HbO_2 + Hb}, \quad (4.5)$$

where S_{O_2} is the hemoglobin oxygen saturation, HbO_2 is the oxyhemoglobin concentration and Hb is the deoxyhemoglobin concentration. The simulated value is 70%, which is correctly recovered near the surface. However, with increasing depth the amount of unmixed deoxyhemoglobin decreases because of the spectral flattening phenomenon shown in figure 4.8, causing the calculated S_{O_2} values to increase. (The same decrease occurs for oxyhemoglobin, albeit slower.) Finally, we reach depths where the spectral components of deoxyhemoglobin and then oxyhemoglobin become inverted: from then on the nonnegativity constraint in the spectral unmixing algorithm (see section 4.3.1.1) sets the respective components to zero, causing the two flat parts of the plot. Since, in this particular case, the spectra we are unmixing for (oxy- and deoxyhemoglobin) are the same ones causing wavelength-dependent fluence attenuation, the problem is rather extreme. Note also that the hemoglobin concentrations used in the simulation were chosen for the heart region, which is highly absorbing. For tissue with lower overall hemoglobin values, the results would be accurate up to a greater depth.

If instead we are unmixing for a spectrum which has little influence on the

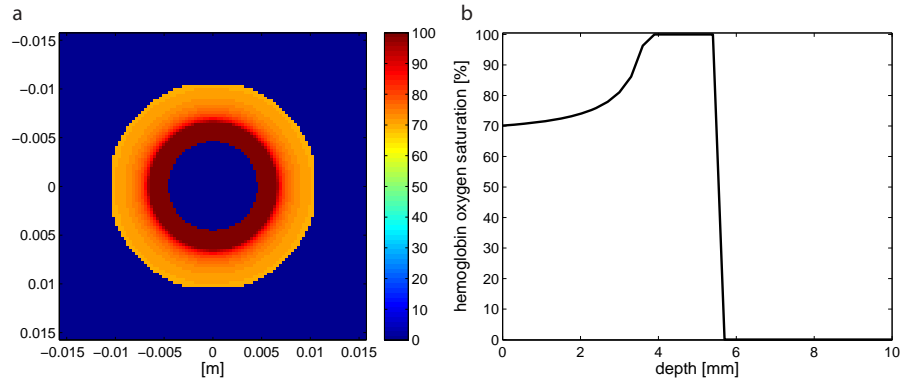


Figure 4.9: Recovery of hemoglobin oxygen saturation with depth without fluence correction. a: Image of hemoglobin oxygen saturation. b: Recovered value against depth.

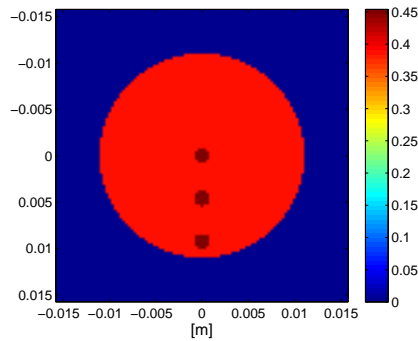


Figure 4.10: Absorption coefficient of model with 3 ICG inclusions (200nM concentration) at 790nm. Values on colour scale are in $[\text{cm}^{-1}]$.

overall fluence attenuation, the results are better. Consider 3 inclusions of ICG (200nM concentration) in the previous tissue background. Figure 4.10 shows the input model. As can be seen from the spectral unmixing result in figure 4.11, it is possible to detect all three inclusions despite wavelength-dependent light attenuation, because the characteristic peak of the absorption spectrum of ICG (see figure 4.4) is narrow, and situated in a region where hemoglobin absorption does not rapidly change with wavelength.

By doubling the ICG concentration to 400nM and again performing spectral unmixing, we obtain the results shown in figure 4.12. The inclusions display close to double the original intensity. We can thus conclude that despite wavelength-dependent light attenuation, it is possible, in theory, to make accurate comparisons between concentrations of chromophores at similar depths, *without any fluence correction*, as long as the absorber’s spectrum is

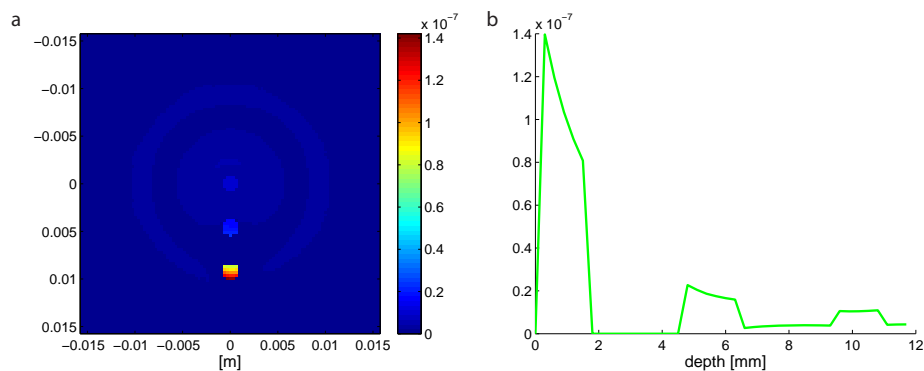


Figure 4.11: Unmixing of ICG at varying depth. a: Unmixed ICG image, b: Profile through ICG inclusions.

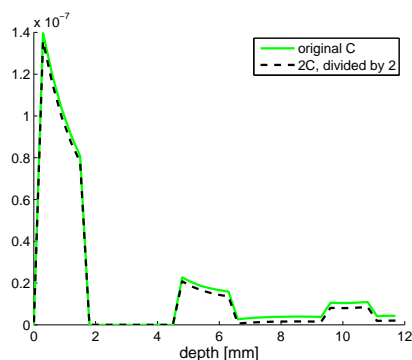


Figure 4.12: Unmixing of ICG at varying depth for 2 concentrations. Profile through ICG inclusions comparing double concentration (400nM) scaled down to level of original concentration (200nM).

sufficiently different to the tissue background, such as ICG in tissue. Note though that the presence of a high background concentration of ICG would negatively affect the results.

4.4.3 Ratio normalisation

Ratio normalisation brings a number of advantages in the extraction of quantitative measures from MSOT data. In order to make a meaningful comparison of agent concentration across measurements spanning over a longer time period, or at varying depths, we normalise the results from the unmixing algorithm by the total signal strength per pixel, that is:

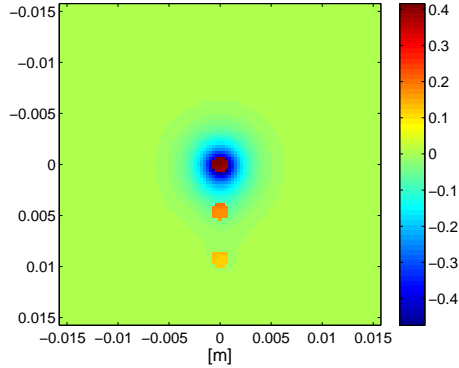


Figure 4.13: Ration normalisation of ICG unmixing results.

$$\frac{\phi c_{agent}}{\phi \sum_{j=1}^N c_j} = \frac{c_{agent}}{\sum_{j=1}^N c_j}, \quad (4.6)$$

where c_{agent} is the concentration of the target absorber. The result is a measure of the relative agent concentration, independent of differences in signal because of overall fluence variations due to light attenuation in tissue. Wavelength-dependent light attenuation is not corrected by this approach. Returning to the multispectral simulation model with three ICG inclusions (figure 4.10), the unmixing results showed a strong decrease with depth due to the overall attenuation of light. By applying ratio normalisation in this case we obtain the image shown in figure 4.13. As is apparent from the image, the two inclusions closest to the surface now have similar intensities, although one is about 5mm deeper than the other. The effects of wavelength-dependent attenuation cause the centre inclusion to have a higher intensity. Therefore, we can conclude that ratio normalisation corrects for the overall attenuation of light, but does not correct for wavelength-dependent attenuation changes. In real experiments, ratio normalisation of unmixing has additional advantages: changes in laser excitation energy over time are corrected for, as are spatial differences in detector sensitivity, since the normalisation results are relative measures. The values extracted using this method can readily be compared to each other, as long as they come from regions with the same background absorption, for example, regions in the liver, or kidneys. For examples of experimental results where ratio normalisation was applied, see chapter 6.

4.5 Concluding remarks

This chapter has described the steps needed to produce meaningful MSOT images of specific absorbers from raw optoacoustic measurement data, as well as limitations involved with multi-wavelength excitation in deep-tissue. For image reconstruction, linear model-based approaches that take the system characteristics into account are recommended for producing quantitative results. Fast delay-and-sum methods are ideal for live displays in real-time imaging because they allow image reconstruction in the time between individual laser pulses, even on inexpensive personal computing hardware, and give valuable qualitative feedback during experiments. For quantitative deep-tissue imaging, wavelength-dependent light attenuation poses a challenge; suitable correction techniques are a subject of ongoing research. However, targets at similar depths can be compared based on MSOT intensities, and relative measures can be obtained using ratio normalisation approaches that correct for overall light attenuation with depth and other possible measurement imperfections. Overall, the methods presented in this chapter provide a procedure for converting raw optoacoustic measurement data into information-rich MSOT images from which a number of quantitative measures can be extracted.

Chapter 5

Sources of MSOT contrast

5.1 Introduction

This chapter discusses sources of image contrast in MSOT. A brief discussion of the contrast mechanism in pulsed optoacoustics is followed by sections on the different contrast sources. First, tissue-intrinsic absorbers of light that can be imaged by MSOT, including hemoglobin, melanin and water, are investigated, to give an idea of what can be visualised in untreated tissue. Original results demonstrating hemoglobin contrast from liver vasculature and blood oxygen saturation in the mouse tail are shown. The focus then turns to exogenous contrast agents, providing salient examples of agents that have been demonstrated in imaging applications in the literature, and then describing original research methods and experimental results for the visualisation of indocyanine green, gold nanorods and an MMP-activatable fluorescent agent by MSOT. Finally, the imaging of reporter genes by MSOT, a topic of growing research interest, is briefly discussed.

5.2 Contrast in MSOT

From chapter 2, we know that optoacoustic image intensity (initial pressure) is given by:

$$p_0 = \Gamma \phi \mu_a \quad (5.1)$$

where Γ is called the Grüneisen coefficient, which describes the thermodynamic properties of the material being heated, ϕ is the light fluence, and μ_a is the absorption coefficient. We see that the initial pressure is proportional to the product of the local light fluence and light absorption coefficient, that is, the optoacoustic image represents the amount of optical energy absorbed at each point in space. The fluence at each point depends on the illumination

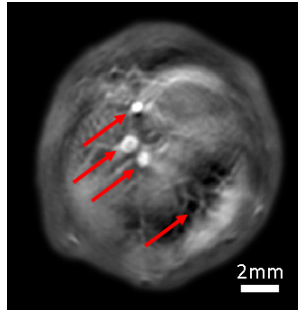


Figure 5.1: Blood vessels (indicated by arrows) in the liver of a mouse.

sources that we set, as well as the optical properties of the tissue. Spatial variations in fluence are relatively smooth due to the high scattering of light in tissue. As a result, the factor providing, by far, the most defined (high frequency) image contrast, is μ_a , the local absorption coefficient. Contrast sources are therefore materials that absorb light.

5.3 Intrinsic tissue absorption

5.3.1 Hemoglobin contrast

To appreciate why optoacoustic imaging is capable of producing high contrast images of blood vessels, consider the difference in absorption coefficients between blood and surrounding tissue. As an example, at a wavelength of 800nm, hemoglobin, whether oxygenated or not, has a molar extinction coefficient of approximately $800\text{cm}^{-1}\text{M}^{-1}$. (Using data compiled by Scott Prahl, Oregon Medical Laser Center (<http://omlc.orgi.edu/spectra>), from multiple sources.) A typical value of hemoglobin concentration in whole blood is 150g/l, resulting in an absorption coefficient of $\mu_a = 2.3\text{cm}^{-1}$. Assume the tissue surrounding the blood vessel has an absorption coefficient in the region of 0.2cm^{-1} [19]. Taking into account the fact that the optoacoustic signal amplitude is directly proportional to the absorption coefficient, we have an order of magnitude more signal from blood than from the surrounding tissue. As a result, vascular imaging is a natural application of optoacoustic imaging. To illustrate this point, figure 5.1 shows an optoacoustic image through the liver of a mouse *in vivo* taken at an excitation wavelength of 850nm without any signal averaging, that is, produced from a single laser pulse (real-time system from section 3.5.2). Several blood vessels of various sizes are clearly visible, even though the liver tissue surrounding the blood vessels is quite absorbing compared to other tissue types [62].

In addition to simply producing images of vasculature at single wavelengths,

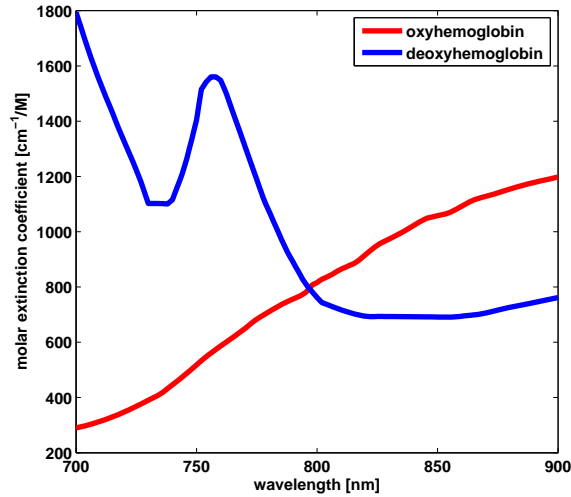


Figure 5.2: Extinction spectra of hemoglobin (blue) and oxygenated hemoglobin (red). Data compiled by Scott Prahl, Oregon Medical Laser Center (<http://omlc.ogi.edu/spectra>), from multiple sources.

we can gain further information by multispectral imaging: hemoglobin displays a change in absorption spectrum based on its oxygenation state. The corresponding extinction spectra are plotted in figure 5.2. By MSOT, it is thus possible to resolve the concentrations of the two oxygenation states and therefore related measures, such as blood oxygen saturation. The relevant formula is as follows:

$$S_{O_2} = \frac{HbO_2}{HbO_2 + Hb}, \quad (5.2)$$

where S_{O_2} is the oxygen saturation to be calculated, HbO_2 is the concentration of oxygenated hemoglobin and Hb is the concentration of deoxygenated hemoglobin. This functional imaging capability has been demonstrated in different variations over the past years, including the use of two visible wavelengths in microscopic imaging of superficial vasculature [63] and deep tissue sensing [64].

Figure 5.3 shows blood oxygen saturation in blood vessels in the tail of a mouse as an example of functional imaging by MSOT. The experimental protocol and processing steps used in this example are as follows:

1. MSOT imaging (real-time system from section 3.5.2) was performed at multiple wavelengths: 700nm, 730nm, 760nm, 790nm, 810nm, and 850nm.

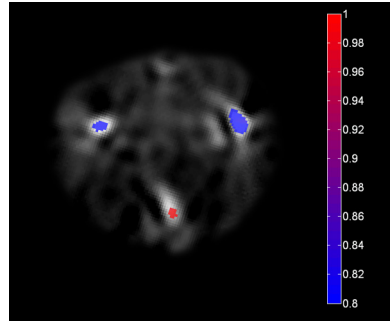


Figure 5.3: Blood oxygenation in veins and artery of a mouse tail. The scale bar indicates blood oxygen saturation (S_{O_2}) as a fraction.

2. The spectral contributions of oxy- and deoxyhemoglobin were computed per pixel by linear spectral unmixing.
3. A minimum threshold was applied to the hemoglobin image (sum of both oxygenation components) to select only pixels belonging to blood vessels.
4. Equation 5.2 was applied to each selected image pixel to obtain the S_{O_2} values.

The image is composed of two layers. In the background, using a greyscale to represent intensity, is a single wavelength optoacoustic image taken at 850nm. This image provides anatomical structures of the tail. The overlay, in a colour scale from blue (less oxygenation) to red (maximum oxygenation) shows the functional information, in this case oxygen saturation. Potential applications of such measurements are numerous: for one, blood oxygen saturation in arteries is a measure of hypoxemia.

5.3.2 Further tissue-intrinsic sources of MSOT contrast

Melanin is a biological pigment found in the skin and hair, and represents a strong absorber of light which has been exploited in optoacoustic imaging. For example, Oh et al. used the absorption of melanin to produce microscopic optoacoustic images of melanoma [65], an application that can be found several times in the literature in various forms. An absorption spectrum taken from the literature of eumelanin, a common form of melanin, is shown in figure 5.4. Note that melanin is present in large enough concentrations in pigmented skin for large optoacoustic signals to be generated, even in the near infrared (see figure 5.5).

Water concentration in tissue is of much interest as a pathophysiological

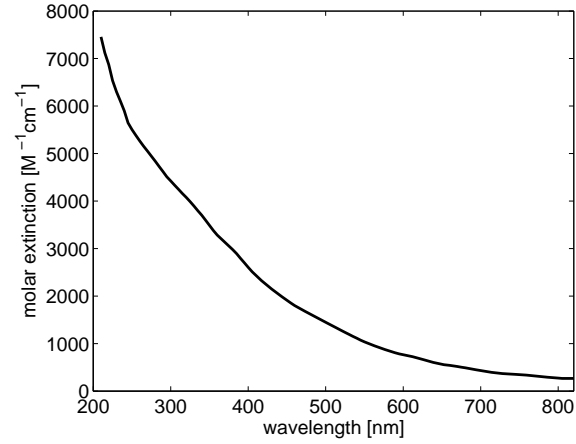


Figure 5.4: Extinction spectrum of eumelanin. Data compiled by Steven Jacques, Oregon Medical Laser Center (<http://omlc.ogi.edu/spectra>) from [66].

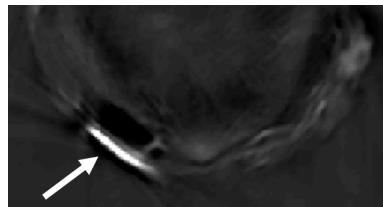


Figure 5.5: Strong optoacoustic contrast produced by melanin, indicated by arrow, in the skin of a mouse (black 6). Excitation at 900nm (real-time system from section 3.5.2).

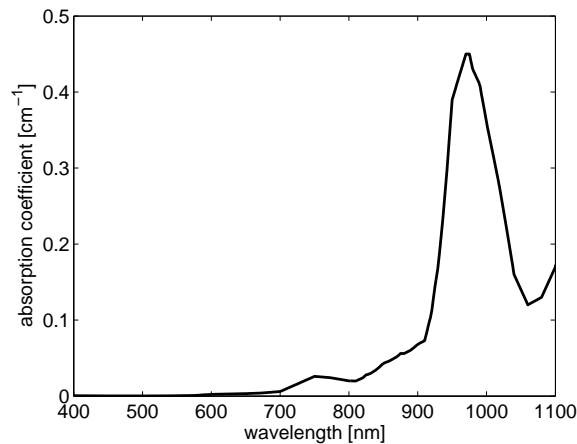


Figure 5.6: Water absorption spectrum. Data compiled by Scott Prahl, Oregon Medical Laser Center (<http://omlc.ogi.edu/spectra>) from [20].

biomarker, displaying elevated levels in tumors, and has been reported to be distinguishable by MSOT in initial studies by Xu et al. [67]. Water has an absorption spectrum as shown in figure 5.6, with a local peak around 975nm. A challenge in imaging water is its relatively high normal tissue concentration, which could serve to attenuate the excitation light on its way to the target. However, water does represent a promising additional intrinsic tissue parameter which can potentially be extracted by MSOT.

Lipids display an optical absorption peak at around 1200nm, which has values an order of magnitude lower in NIR wavelengths up to 1100nm [68]. Since lipids form an important component of atherosclerotic plaques, some efforts at their detection by intravascular optoacoustic imaging have been reported [46, 69]. The high absorption of water in this wavelength range, however, makes it challenging to perform lipid detection noninvasively at macroscopic scales.

5.4 Exogenous contrast agents

Table 5.1 provides several examples of light absorbing contrast agents that have been reported in the literature for use in optoacoustic imaging applications. Contrast agents for MSOT are generally application driven, however, some essential properties are universal. Obviously, in order to generate an optoacoustic signal, the agent must absorb light. Typically, for imaging at depth, this absorption should occur in the NIR, so that light can reach the agent. Absorption in the NIR would be sufficient if the imaging was

performed in a time series where an increase (or decrease) in contrast over time is measured in an unchanging background. A number of examples of such imaging, which can be performed at a single wavelength, have been documented. Salient examples include the use of gold nanocages for imaging of the sentinel lymph node in rats [10] and imaging of tumors in mice using targeted carbon nanotubes [70]. However, an unchanging background (or unmoving tissue) is not always realistic. In *in vivo* experiments where imaging agents should be visualised over the course of several hours or days, it is impractical to position the tissue in exactly the same way during each imaging session. As soon as the tissue background changes, there is a problem distinguishing the imaging agent from the intrinsic background tissue absorption discussed in section 5.3. Therefore, to detect signal specific to the contrast agent in question, that is, to suppress the background signal, it is essential to image at multiple wavelengths and unmix the resulting images to obtain the various spectral signatures, including that of the agent. This adds another requirement for suitable MSOT contrast agents: they should have an absorption spectrum that uniquely distinguishes them from intrinsic tissue absorbers. In the ideal case, an MSOT contrast agent would have an ultra-thin peak in its absorption spectrum: when imaging at the applicable wavelength, the agent would absorb a lot of light and generate a high optoacoustic signal; when slightly changing the wavelength, so that the background absorption does not significantly change, the agent would not absorb any light or generate any signal at all. The two images could be subtracted from one another to obtain a spatial map of the contrast agent, without significant background. In reality, the absorption peaks of potential contrast agents are generally too wide to allow such an approach: in the wavelength range from peak to off-peak absorption there is usually a significant change in the spectra of tissue intrinsic absorbers, therefore making more sophisticated spectral unmixing approaches mandatory. However, it still holds that the narrower the absorption peak, the easier it is to uniquely identify to agent. So we have, from a technical view, a set of requirements for MSOT contrast agents: they should display high absorption in the NIR with a narrow absorption peak.

Note that not all of the agents listed in table 5.1 display very sharp absorption peaks: for example, carbon nanotubes have a relatively flat characteristic spectrum. Generally, many of the reported imaging results in the table employed single wavelength imaging with some sort of reference threshold to detect contrast enhancement after agent injection or accumulation. Since the concept of MSOT is based on separation of specific absorbers based on their spectra, agents that have been used in this manner are not necessarily ideal for MSOT imaging. Ntziachristos et al. introduced a measure of absorption, corrected for quantum (fluorescence) yield, per unit of mass concentration, in an attempt to compare the optoacoustic efficiency of different

contrast agents [71]. The results show that near infrared fluorescent dyes display higher values than a range of other agents, such as gold nanorods. However, it is difficult to compare such a range of vastly different agents when characteristics like weight and pharmacokinetic profiles may vary by orders of magnitude. The selection of agents for real-world imaging applications depends on many other factors than signal efficiency, such as whether the agent is approved for use in patients (ICG is, gold nanoparticles are not), whether the dimensions of the molecules or particles are suitable for certain physiological effects (gold nanoparticles can be made in the right size range to accumulate by enhanced tumor vascular permeability, for example), whether the agent can be conjugated to targeting ligands (ICG has no available reactive group for this purpose) et cetera. Other characteristics should also be considered in the context of efficient generation of optoacoustic signals. For example, plasmonic nanoparticles can undergo coupling when brought close together, a fact which was exploited by Mallidi et al. by targeting gold nanospheres to closely packed receptors [72]. However, this could be a major disadvantage: gold nanorods can also be coupled *in vivo*, for example when taken up by inflammatory cells, causing their absorption spectrum to change unpredictably. Additionally, gold nanorods are known to change shape (and therefore absorption spectrum) due to melting from the heating energy of pulsed lasers [73, 74] which could limit the fluence and number of pulses used for quantitative optoacoustic imaging, an issue that requires further investigation. On the other hand, organic dyes are well known to undergo photobleaching under intense illumination, also resulting in alterations to their absorption spectra. All these factors need to be taken into account when selecting MSOT contrast agents.

I will discuss two different types of contrast agents in the following: organic dyes and gold nanorods. Organic dyes are in very widespread use in biomedicine, in particular for use as fluorescent agents in imaging ranging from microscopy using immunofluorescence to deep-tissue diffuse optical techniques such as Fluorescence Molecular Tomography [6]. They are available in various wavelength regions, including the NIR. Additionally, they have been incorporated into a multitude of molecular imaging agents, by adding targeting ligands or by dequenching mechanisms upon specific enzymatic action (activatable probes). Many of these molecular imaging agents are commercially available. A further advantage of organic dyes is their clinical potential, for example, indocyanine green (ICG), is clinically (FDA) approved. In fact, ICG has been established as a tool to investigate a variety of different clinical endpoints such as hepatic function [82].

As for gold nanorods, they are an example of nanostructures with high absorption in the NIR region and tunable longitudinal plasmon resonances dependent on their aspect ratio. Due to their well established surface con-

Contrast giving agent	Absorption features	Reported applications
Methylene blue	677nm peak	Lymphatic mapping in 2008 by Song et al. [75].
Indocyanine green (ICG)	810nm peak (in plasma)	Brain angiography in 2004 by Wang et al. [76] and numerous other applications.
IRDye 800CW (Licor)	774nm peak	Conjugated with RGD peptide to target brain tumors in 2008 by Li et al. [13].
Gold nanorods	Tunable NIR	Multispectral identification in the circulation in 2010 by Taruttis et al. [34].
Gold nanospheres	Increase in NIR absorption when closely coupled	Tumor targeting and subsequent resonance coupling by antibody conjugation in 2009 by Mallidi et al. [72].
Hollow gold nanospheres	Tunable peak in NIR	Contrast enhanced imaging of the brain vasculature in 2010 by Lu et al. [77].
Gold nanocages	Tunable peak in NIR	Bioconjugated to target melanoma in 2010 by Kim et al. [78].
Gold-enhanced carbon nanotubes	Increased NIR absorption	Optoacoustic and photothermal flow cytometry in 2009 by Kim et al. [79].
Silver nanoplates	Absorption in 1000nm region	Demonstrated as contrast agent for imaging at 1064nm in 2010 by Homan et al. [80].
Single-walled carbon nanotubes (SW-CNT)	Relatively flat spectrum	Conjugated with RGD peptide for tumor targeting in 2008 by de le Zerda et al. [70].
ICG-enhanced single-walled carbon nanotubes	Spectrum defined by ICG	Conjugated with RGD peptide for tumor targeting in 2010 by de le Zerda et al. [81].

Table 5.1: A selection of contrast agents reported in the literature for optoacoustic imaging.

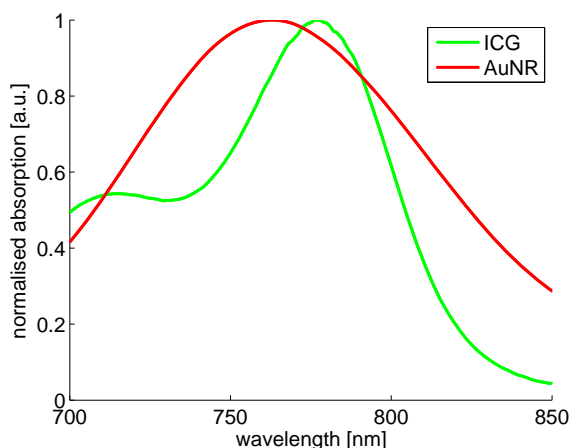


Figure 5.7: Normalised absorption spectra of ICG and AuNR (spectrometer measurements).

jugation chemistry, gold nanorods can be easily linked to specific ligands in order to target molecular entities such as cell receptors [83]. In addition, the intense photothermal properties due to the conversion of optical energy into heat via non-radiative electron relaxation dynamics, can be used for therapeutic purposes [84] and allow light-mediated drug release [85].

As a specific example, I will show imaging results using ICG and gold nanorods (AuNR). The particular AuNR employed (Ntracker 30-PM-780, Nanopartz Inc.) have an absorption peak in the NIR around 780nm, and a per-particle width of 10nm and length of 38nm. A proprietary methyl-polymer coating gives the nanorods lengthened circulation times. The absorption spectra of ICG (in water) and AuNR, normalised to their maxima, are plotted in figure 5.7 (measured in a VIS-NIR spectrometer, Ocean Optics). From the plot we can see that both agents display an absorption peak in the NIR. The ICG peak is narrower: it drops to under 10% of its peak absorption within 50nm. The AuNR also drops in absorption away from its peak, but slower than ICG, not reaching values lower than 20% in the wavelength range shown. From this information we can conclude that both could be suitable MSOT contrast agents, but the ICG is likely to be easier to distinguish from tissue background because of its narrower absorption peak.

The next step in the evaluation of MSOT contrast agents is multispectral phantom imaging. I performed such imaging to show that these agents can be detected by MSOT. Tissue-mimicking cylindrical phantoms of 2cm diameter were prepared by moulding 1.3% weight of agar powder (Sigma-Aldrich) mixed with 0.22% black India ink (Higgins) and 6% of Intralipid

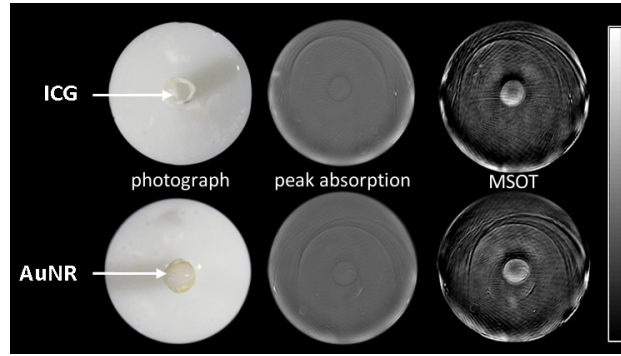


Figure 5.8: Phantom imaging of ICG and AuNR.

20% emulsion (Sigma-Aldrich) to obtain a background with an optical absorption coefficient of $\mu_a \approx 0.2\text{cm}^{-1}$ and a reduced scattering coefficient of $\mu'_s \approx 10\text{cm}^{-1}$. A cylindrical inclusion with a diameter of approximately 3mm in the centre of the background cylinder additionally contained either $0.8\mu\text{M}$ ICG or $1.4\mu\text{g/ml}$ AuNR, corresponding an additional absorption of $\mu_a \approx 0.2\text{cm}^{-1}$ as determined using a spectrometer. MSOT data sets of the phantoms were recorded between 720nm and 850nm with 10nm steps using 100 signal averages (real-time system from section 3.5.2). The results are summarised in figure 5.8. Images acquired near the peak absorption wavelengths of 790nm and 780nm for ICG and AuNR respectively (figure 5.8, middle column), display no clear contrast from the inclusions because of strong light attenuation inside the phantoms and low concentrations of the agents. However, by imaging at multiple wavelengths and employing spectral unmixing, the ICG and AuNR could be resolved with high contrast (figure 5.8 right column): the target-to-background ratios (TBR) of the inclusions increased from approximately 1 to 2.6 and 3.0 respectively. The location of the inclusions was at approximately 1cm depth from the phantom surface, representing a challenging imaging scenario and indicating the feasibility of spatially resolved detection of these agents by MSOT.

Finally, contrast agents should be evaluated *in vivo*. I will show results here of MSOT imaging (real-time system from section 3.5.2) of circulating AuNR in mice [34]. $200\mu\text{l}$ of AuNR at a number density of 7.8fl^{-1} was injected via the tail vein. During agent injection, data from a slice through the neck were continuously acquired (live imaging) over 110s at 780nm. Selected frames from the live imaging sequence show increasing contrast in the jugular veins as the AuNR enters the circulation (before injection: figure 5.9a, during injection: figure 5.9b, and after injection: figure 5.9c). We can conclude from the contrast increase that the injected dose of AuNR produces detectable contrast for dynamic imaging.

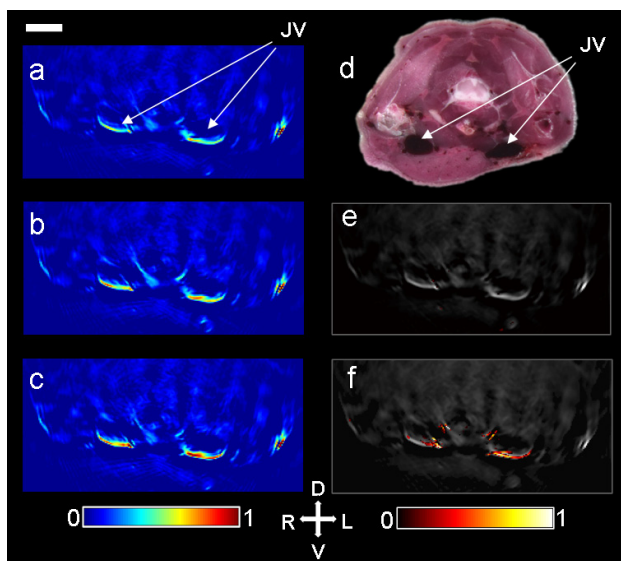


Figure 5.9: MSOT detection of circulating gold nanorods. JV - Jugular veins. a: Single-pulse transverse slice through neck prior to injection. b: The same slice during injection of AuNR. c: And 10 s after finishing the injection of AuNR. d: Photograph of cryosection showing anatomical correspondence. e: MSOT image before injection. f: MSOT image post injection showing multispectrally resolved distribution of AuNR overlaid on a single wavelength image. Scale bar 3mm. Reproduced from [34].

However, we still want to see whether MSOT detection of the AuNR at a single time point based on its spectral profile is feasible. To this end, the same slice imaged in the live sequence was scanned at 5 excitation wavelengths (725nm, 750nm, 775nm, 800nm, 825nm) using 10 signal averages both before and after the injection of AuNR. MSOT images where the AuNR signal, resolved using linear spectral unmixing, was overlaid in pseudo-colour on single wavelength (anatomical) images are shown for both time points (before injection: figure 5.9e, after injection: figure 5.9f). As can be seen on the resulting images, MSOT was able to specifically detect circulating AuNR after injection. The spatial location of the resolved AuNR signal corresponds well to the regions of increased contrast in the live imaging results during injection. This result highlights the ability of MSOT to resolve the AuNR *in vivo* at high resolution without need for a baseline measurement, based on their distinct spectral profile over the background tissue absorption spectrum. An estimation of the average AuNR concentration in the bloodstream can be calculated by multiplying the initial concentration injected by the injected volume and dividing by a typical value for the volume of blood in a mouse: $\frac{7.8\text{fl}^{-1} \times 200\mu\text{l}}{2\text{ml}} = 0.78\text{fl}^{-1}$.

5.4.1 Activatable optical agents

Activatable fluorescent agents, which are initially optically silent but become fluorescent when cleaved by enzymes, have proven to be a uniquely powerful tool for imaging specific protease activity [17, 86]. These probes work by positioning multiple fluorochromes close enough together that their fluorescence is quenched; cleaving by proteases then separates the fluorochromes which can then be seen by fluorescence imaging. Since the dequenching is also associated with a change in the absorption spectrum of the probe in question, detection by MSOT could be feasible.

Figure 5.10 shows the results of a feasibility study on MSOT detection of a matrix metalloproteinase (MMP) activated fluorescent probe (MMPSense 680, PerkinElmer) [87]. The experimental method was as follows:

1. MMPSense was prepared in a concentration of $1\mu\text{M}$.
2. Of this solution, part of it was activated using Trypsin at a concentration of $100\mu\text{M}$. The rest was left in the inactive state to serve as a control.
3. After 4hrs at room temperature, the extinction spectra of the two samples was measured in a VIS-NIR spectrometer.
4. Using a self-built planar fluorescence imaging system, the NIR fluorescence of the two samples was measured to verify successful activation.

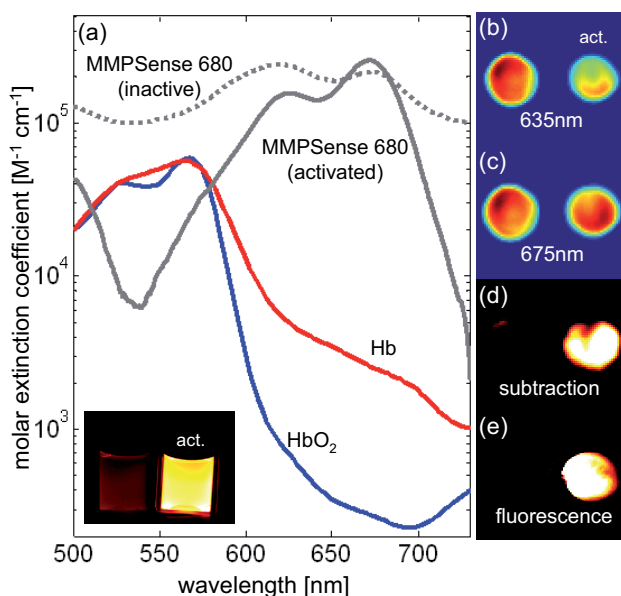


Figure 5.10: Activation of MMPsense 680 *in vitro* and detection by MSOT. a: Extinction spectra of MMPsense in its active and inactive states, compared to hemoglobin spectra. Inset shows comparison of the fluorescence signal between the two activation states. b: Optoacoustic image at 635nm excitation. c: Optoacoustic image at 675nm. d: Subtraction image 675nm-635nm. e: Planar fluorescence image of the phantom from above. Reproduced from [87].

5. A cylindrical phantom of 14mm diameter was molded from agar with Intralipid added to give a scattering coefficient of $\mu'_s \approx 20\text{cm}^{-1}$. Two cylindrical inclusions of 3mm diameter inside the phantom held the probe solutions in active and inactive states respectively.
6. The phantom was imaged at 675nm and 635nm in the single detector MSOT imaging system described in section 3.5.1.
7. After MSOT imaging, the phantom was imaged in the planar fluorescence system for further validation.

The measured spectra from the samples (figure 5.10a) confirm that there is a change after activation. In particular, a more pronounced absorption peak appears near 675nm, and the previous peak at around 620nm drops when compared to the inactive probe. MSOT imaging also detects this change: in the image at 635nm excitation, the inactive probe inclusion is brighter than that of the active probe (figure 5.10b); at 675nm the active probe inclusion increases in intensity. By subtracting the two images (figure 5.10d)

it is possible to enhance the active inclusion and suppress the inactive inclusion and background absorption because of the presence of the absorption peak at 675nm. Figure 5.10e confirms the location of the active probe by fluorescence.

This ability to detect an activatable fluorescent probe by MSOT based on the change in its absorption spectrum on activation was exploited in MSOT imaging of MMP activity in human carotid plaque specimens by Razansky et al. in 2011 [87].

5.5 Reporter genes

For the sake of completeness, MSOT imaging of reporter genes should be mentioned. Fluorescent proteins in particular are in daily use in biological research, and efforts are continuing to shift their excitation and emission wavelengths into the NIR to enable imaging in deeper tissues [88]. In the meantime, Razansky et al. demonstrated MSOT detection of fluorescent proteins, largely in the red wavelength range, in model organisms such as zebrafish in 2009 [89]. Additionally, recent work has led to reporter gene imaging specifically conceived for optoacoustic imaging: by introducing the gene encoding tyrosinase, which is responsible for producing melanin (a tissue absorber, see section 5.3.2), cells have been reported to produce an order of magnitude more optoacoustic signal [90]. These advances suggest a role for MSOT imaging of reporter genes in basic biological research, allowing a higher resolution in deep tissue than the fluorescence approaches employed thus far.

5.6 Concluding remarks

The purpose of this chapter was to provide an overview of the contrast mechanism and the sources of such contrast for MSOT imaging. We have seen that the optoacoustic signal amplitude is proportional to absorption, and concluded that absorption is the critical parameter in imaging of intrinsic and exogenous contrast. In the context of intrinsic contrast, results demonstrating the imaging of blood vessels in the liver, and multispectral determination of blood oxygen saturation in blood vessels in the tail, show the performance of such imaging by MSOT. The suitability of further intrinsic contrast sources, melanin, water and lipids, was also discussed. The development and assessment of exogenous contrast agents for optoacoustic imaging is an active research topic, as shown by the numerous examples of different light-absorbing agents found in the literature. However, it is important

to distinguish between agents suitable for single wavelength contrast, like carbon nanotubes, and those with narrow absorption peaks that are more easily identified by multispectral imaging. Overall, decisions about which agent to employ are entirely application dependent, due to vast differences between agents in many respects. Original MSOT imaging results using ICG and gold nanorods were presented. *In vivo* imaging of gold nanorods in the circulation showed the advantage of multispectral imaging: no reference measurements are required to obtain images specifically resolving the agent above background contrast. Further, the feasibility of MSOT detection of an MMP-activatable fluorescent agent was demonstrated, promising imaging of specific enzyme activity. A brief discussion of reporter gene imaging by MSOT revealed recent research activity in that direction, as the ability for high resolution imaging in deeper tissues than possible with fluorescence could be of great interest in biological research.

Chapter 6

Tracking the fate of optical agents

6.1 Introduction

The characterisation of pharmacokinetic and biodistribution profiles is an essential step in the development process of new candidate drugs or imaging agents. Simultaneously, the assessment of organ function related to the uptake and clearance of drugs is of great importance. The use of optical imaging, particularly near-infrared fluorescence (NIRF), has become widespread because of the ease with which compounds can be tagged with fluorochromes and subsequently imaged. However, as discussed in chapter 1, optical scattering in tissue conceals the true underlying agent distribution. Furthermore, when tomographic techniques are applied, acquisition times run into several tens of minutes [60]. Since MSOT is capable of visualising blood vessels and organs (liver, kidneys, et cetera), and further enables the extraction of measures of relative optical agent concentrations, it suggests itself for a role in assessing pharmacokinetics. Parallel ultrasound detection has allowed imaging rates of 10 frames/s (see section 3.5.2). Rapid changes in excitation wavelength allow high-rate multispectral measurements. Overall, this ability of MSOT to rapidly image exogenous agents in various organs prompted us to investigate the performance of the method in dynamic imaging of pharmacokinetics and biodistribution. In particular, MSOT was employed to characterise the removal of indocyanine green (ICG) from the systemic circulation and its time-resolved uptake in the liver and gallbladder. Overall, such imaging performance introduces previously undocumented capabilities of fast, high resolution *in vivo* imaging of the fate of optical agents for drug discovery and basic biological research. The contents of this chapter have been submitted for publication under the title

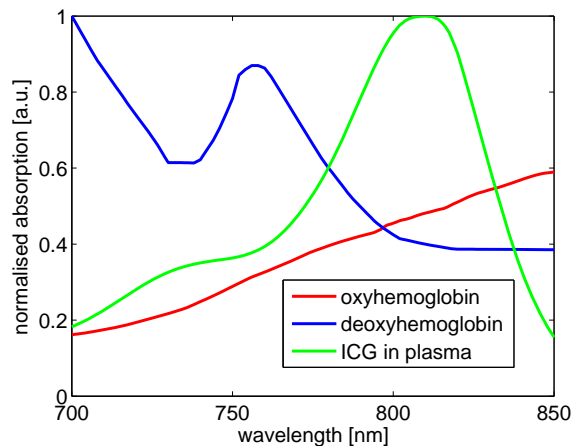


Figure 6.1: Normalised absorption spectra of ICG and hemoglobin. Data compiled by Scott Prahl, Oregon Medical Laser Center (<http://omlc.ogi.edu/spectra>), from multiple sources.

Fast multispectral optoacoustic tomography (MSOT) for dynamic imaging of pharmacokinetics and biodistribution in multiple organs.

6.2 Materials and methods

6.2.1 Experimental protocol

Indocyanine green (ICG, Pulsion Medical Systems) was selected for this study due to its well-known characteristics. It is an FDA approved, water-soluble, inert anionic tricarbocyanine dye that has been established as a tool to investigate a variety of different clinical endpoints such as hepatic function [82]. The absorption spectrum of ICG (figure 6.1) shows a peak in the near infrared (NIR) wavelength range.

We used adult CD1 mice, anaesthetised with 2% Isoflurane throughout the experiments. The real-time MSOT system (see section 3.5.2) was employed. We chose 5 excitation wavelengths per experiment based on the maxima and minima in the absorption spectra of the imaging agents and tissue absorbers: 700nm, 730nm, 760nm, 800nm, and 850nm. MSOT imaging was performed according to the following experimental protocol:

1. Multispectral imaging prior to injection.
2. Imaging at peak agent absorption wavelength during injection.

3. Multispectral imaging post injection continuously for 20-30 minutes.

Multispectral imaging was performed with 50 signal averages (laser pulses) per wavelength for liver imaging and 10 signal averages for circulation imaging to allow a more finely resolved time axis during the fast decay. We injected doses of 40nmol of ICG. The imaged slices were a region in the lower abdomen with visible blood vessels for the characterisation of ICG in the circulation, and the liver at a slice where the gallbladder is also visible.

6.2.2 Image reconstruction and quantification

The single wavelength images were reconstructed using filtered delay-and-sum (see section 4.2.1). The resulting images were then spectrally unmixed (section 4.3.1) using the known absorption spectra of oxy- and deoxyhemoglobin and ICG as well as a constant (flat) spectrum as input. To obtain relative chromophore concentration measures, ratio normalisation (section 4.4.3) was applied by dividing the unmixed image for ICG in each case by the sum of all unmixed images. This approach ensures that changes over time in laser energy are cancelled out, and that pixels where the overall attenuation of light with depth causes the optoacoustic signal to decrease are again comparable. The values from which signal curves were generated were then obtained by selecting relevant regions-of-interest (ROI) and calculating the mean values of the normalised images inside each of these ROIs.

6.3 Experimental results

6.3.1 Circulating ICG

The experimental MSOT imaging results are rich in information. In the case of characterising the kinetics of ICG in the circulation, there are several blood vessels in the images to choose from. As shown in figure 6.2, we arbitrarily chose a small blood vessel in the lower abdomen of a mouse from which to extract our metrics. The blood vessel is visible in single-wavelength optoacoustic images, as shown in the greyscale image, because blood absorbs light and thus produces optoacoustic signals. The vessel is also visible in the MSOT image unmixed for ICG (green), because ICG remains in the vasculature before being removed by the liver. The ICG signal curve obtained by MSOT is shown in figure 6.3. Each point represents a multispectral measurement with 10 laser pulses per wavelength; the time between each of these multispectral measurements was approximately 17s. This time includes the laser pulses, which were 10 at each of 5 wavelengths,

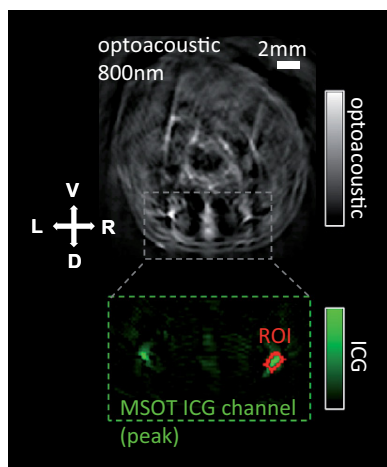


Figure 6.2: Imaging circulating ICG. The optoacoustic image at 800nm is shown for anatomical reference. Below, the resulting image after unmixing for ICG at its signal peak is shown in green, with the manually segmented ROI indicated in red.

taking 5s, and therefore the remaining 12s for wavelength changes. The curve is obtained by fitting an exponential decay function. In this, case, using the selected blood vessel, the value obtained for the circulation half-life is 1m32s.

6.3.2 Liver and gallbladder uptake of ICG

Systemically injected ICG binds to plasma proteins and is removed from the circulation by the liver. We imaged this uptake in two ways: before, during and until shortly after injection, images at 800nm excitation (close to the excitation peak of ICG) were acquired at the full rate of 10 frames/s. Following this, multispectral measurements were taken over a time of approximately 30 minutes to capture changes in the specific ICG signal over a longer time. Two ROIs were selected: one in the liver and another in the gallbladder, which is also resolvable in the optoacoustic images. Figure 6.4 shows the ROIs on an optoacoustic image, as well as a corresponding fluorescence cryosection showing uptake in the liver and gallbladder.

Figure 6.5 shows two optoacoustic images taken at 800nm excitation, one before injection, and one after 11 minutes. These images show that the absorption at this wavelength increases as expected with the injection, and also, in the later image, shows that the gallbladder becomes clearly visible after uptake of ICG. By plotting the optoacoustic image intensity at 800nm during the course of the injection (figure 6.6), we gain a clear picture of

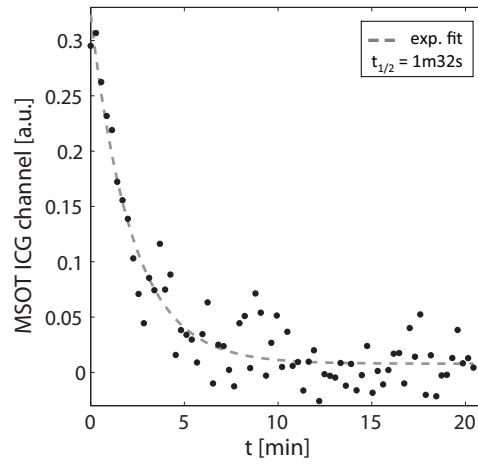


Figure 6.3: ICG being removed from the circulation, as characterised by MSOT imaging

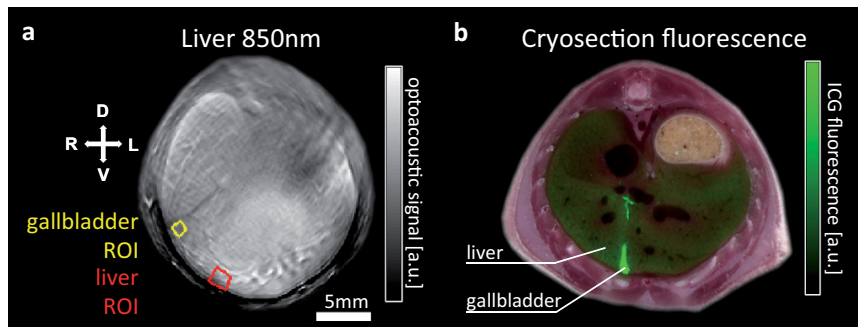


Figure 6.4: Imaging of ICG uptake in the liver. a: Optoacoustic image of the liver showing the ROIs selected for the gallbladder and liver signal curve extraction. b: A corresponding fluorescence cryosection of a mouse sacrificed 10 minutes after injection, where the fluorescence from ICG is overlaid in green on the colour image (see appendix).

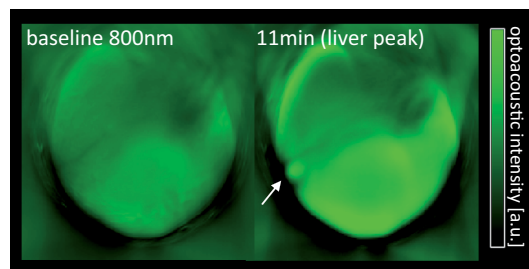


Figure 6.5: Optoacoustic images at 800nm excitation of the liver before (left) and after (right: 11min) ICG injection. White arrow indicates the gallbladder.

the signal increase due to ICG entering the liver: the injection was started at time $t = 20$ s on the time axis, and the signal increases after that time. Strong oscillations are visible in the curve. This is not measurement noise, but rather the effect of movement due to respiration, as verified by inspecting the individual frames corresponding to the time series. As the sampling rate in this case is much higher than the breathing rate, it is possible to neglect the values where movement influenced the values.

From the multispectral data, after applying ratio normalisation, the signal curves specific to ICG in the liver and gallbladder over 30 minutes after injection are shown in figure 6.7. In these plots, the individual measurements, consisting of 50 laser pulses (signal averages) at each of the 5 measured wavelengths are represented as points and the lines represent smoothed versions of this data. Each curve is normalised to its own maximum and shows the profile of ICG uptake in the selected ROIs.

6.4 Kidney function

In related results not shown here, similar experiments in the kidney region established the feasibility of tracking optical agent distributions in separate parts of the kidney. The kidney represents a further crucial organ for assessing pharmacokinetics and possible side effects of novel agents.

6.5 Concluding remarks

The results in this chapter show the potential of MSOT as a tool for fast pharmacokinetics and biodistribution imaging of optical agents. The use of fluorescence in biomedical research is ubiquitous, ranging from fluorescent proteins through targeted agents to enzyme-activatable probes. Epi-

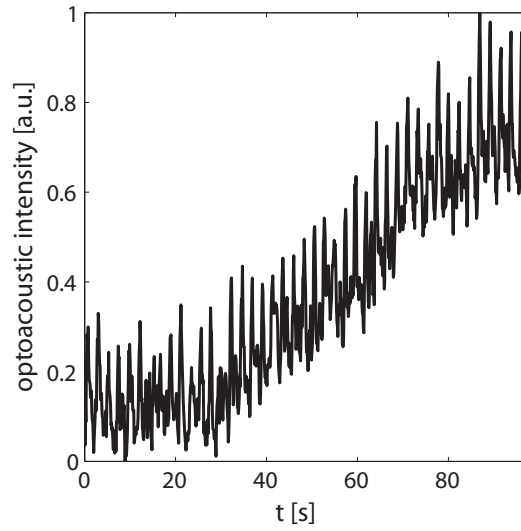


Figure 6.6: Single-wavelength tracking of ICG entering the liver. The injection of ICG starts at $t \approx 20$ s. Strong oscillations in the signal are due to respiration.

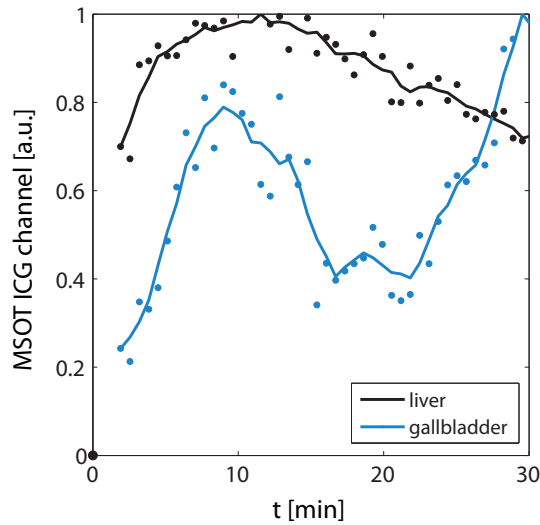


Figure 6.7: ICG dynamics in liver and gallbladder. Each point represents one multispectral acquisition with 50 laser pulses at 5 wavelengths. The lines are smoothed representations of this data.

illumination NIRF imaging is commonly used for biodistribution studies *in vivo*. However, such methods produce surface-weighted images where the high degree of photons scattering in tissue obstructs the true agent distribution, particularly in deeper organs. Tomographic approaches like fluorescence molecular tomography (FMT) solve this problem by producing quantitative 3D images in mice, but serial data collection results in long acquisition times of several tens of minutes per image [60]. In our implementation of MSOT we are able to capture single wavelength images at 10 frames/s and multispectral data sets within seconds: in our experiment measuring ICG in the circulation, we needed 1s per wavelength using 10 signal averages and approximately 3s per wavelength change. This time could be further reduced: the OPO wavelength is tuned by mechanically scanning a crystal; faster scanning would reduce the acquisition time. The amount of signal averaging to use is a matter of further investigation. In the experiments shown in this chapter, signal averaging was primarily used to avoid excessive waiting times for wavelength changes. Ideally, one multispectral data point would be captured within such a short time that significant changes in agent concentration cannot occur. Thereafter, multiple points could be binned or smoothed together to increase the detection sensitivity to the required level. A further application area for MSOT in biodistribution studies could be the imaging of non-fluorescent photo-absorbing materials, in particular those with absorption in the near-infrared, for example, gold nanorods [34] or carbon nanotubes [70].

The ratio normalisation approach used to generate the signal curves has the advantages that variations in fluence, whether resulting from changing laser output energy or overall attenuation of light in tissue, cancel out. While the measure is then a relative one, estimates of absolute concentration, or comparisons in concentrations across organs, could be obtained using knowledge of absorption properties of each organ (or whole blood, in the case of the circulation).

The method is not without limitations, in particular related to the geometry of the experimental MSOT implementation. Probably the most significant of these involves the 2D nature of the imaging system: it is capable of imaging only one transverse slice at a time. While the animal holder can be translated to a different slice position automatically for imaging of different regions, doing this during experiments sacrifices temporal resolution in cases where more than one organ should be imaged simultaneously. Future development work in small animal MSOT imaging systems could aim to image a larger volume at a time, potentially solving this problem using more detector elements in a 3D arrangement.

One of the critical steps in the drug discovery process is the safety and toxicity evaluation of novel pharmaceuticals. As the major metabolic and

excretory organs, liver and kidneys are of major concern in these trials. It is therefore highly important to develop a fast, non-invasive tool to assess liver and kidney function. MSOT can be used to not only determine the biodistribution of a multitude of injected agents, but it can be used in conjunction with organ-specific dyes such as ICG to acquire a general assessment of organ function. Comparisons between the kinetics of ICG clearance before and after drug treatment, for example, could be used to quickly assess organ function and drug-related acute toxicity. Clinical applications of high speed MSOT imaging are realistic: it is worth noting, for example, that the characterisation measurements of ICG in the circulation could be performed on superficial blood vessels in humans with minimal additional effort.

Chapter 7

Cardiovascular imaging and disease

7.1 Introduction

This chapter describes MSOT imaging of the cardiovascular system with a focus on the visualisation of cardiovascular disease. It starts by describing imaging of cardiovascular disease-relevant structures in mice, showing how important arteries and the heart itself can be resolved, a prerequisite for preclinical studies of cardiovascular disease. Particular attention is paid to imaging of the heart, where an approach for dealing with motion-related image blurring is presented. Further, results from imaging studies performed on a preclinical mouse model of heart disease are discussed, indicating the potential of MSOT as a tool for wider application in preclinical research and drug development in this domain. Molecular imaging of cardiovascular disease using exogenous contrast aims at improved diagnosis and risk stratification, selection and assessment of potential therapies, conversion of invasive techniques (for example, biopsies) to noninvasive *in vivo* imaging, and evaluation of new drugs [91]. Preclinical molecular imaging additionally plays an important role in basic biological research of cardiovascular disease. Some previous efforts at optoacoustic imaging of the cardiovascular system in small animals should be mentioned. Song et al. showed optoacoustic imaging of the heart and arteries in the thoracic cavity of a rat in 2008 [92]. In this case, a scanning, backward-mode, spherically focused detection scheme was used. The acquisition time of the rat thorax was over 10 minutes, practically limiting the implementation to *post mortem* imaging. Kruger et al. [11] and Brecht et al. [35] each described small animal optoacoustic imaging systems capable of producing three-dimensional images of mice, including cardiovascular structures such as the heart and abdominal

aorta. In both cases however, the systems require mechanical scanning of transducers to generate complete datasets, thus requiring acquisition times measured in minutes. Zemp et al. demonstrated real-time imaging of cardiovascular dynamics by optoacoustic microscopy with a frame-rate of 50 frames-per-second in 2008 [93]. This resulted in images showing unidentified cardiac absorbers that moved with the heartbeat of the mouse; the frame-rate was fast enough to resolve this motion. However, no previous results have shown the type of detailed, macroscopic images of the heart that will be demonstrated in the following, including real-time views of the cardiovascular system, and the first MSOT images of molecular agent uptake in heart disease.

7.2 Disease-relevant vascular imaging

7.2.1 Purpose

Since blood vessels provide strong optoacoustic contrast, MSOT imaging seems suited for imaging cardiovascular disease. In particular, atherosclerosis, an increasingly prevalent and silently progressing disease, presents an unexploited early detection window to modalities capable of probing its biology [44]. A number of studies involving optical imaging of atherosclerosis in mice have been reported. Fluorescent molecular imaging agents have shown promising potential in revealing the biological processes underway in atherosclerosis, for example, a cathepsin activated agent reported by Chen et al. [94] and an integrin targeted agent reported by Waldeck et al. [95]. However, *in vivo* optical imaging using such agents has only resulted in robustly identifiable signal sources when the fluorescence imaging is combined with anatomical imaging, such as the study using FMT-CT reported by Nahrendorf et al. in 2009 [96], where contrast-enhanced CT provides images of the arteries onto which the fluorescence signals are overlaid. A further challenge in the use of purely optical *in vivo* imaging for preclinical studies of atherosclerosis is the limited spatial resolution. Carotid arteries, one of the primary locations of atherosclerotic plaques, are very small in mice, displaying typical diameters of less than 1mm. They are also several millimetres from the skin surface, where the scattering of light severely degrades the spatial resolution of optical techniques. In contrast, MSOT promises improved spatial resolution in deep tissue, as well as label-free images of blood vessels, combined with the ability to detect a variety of exogenous optical agents. The purpose of this study was to investigate the feasibility of MSOT imaging of arteries of interest in atherosclerosis, in particular the aorta and the carotid arteries. The results of this study were published in 2010 [34].

7.2.2 Method

Adult mice (CD-1 and CD-1 Nude, Charles River Laboratories) imaged *in vivo* were anaesthetised using ketamine/xylazine, shaved (if necessary) prior to imaging in the real-time MSOT system (section 3.5.2) and placed for imaging in a prone position. The mice were linearly translated through the imaging plane in order to image different slices through the neck and upper thorax at multiple wavelengths. Directly after imaging the mice were euthanised and frozen. For anatomical validation of the optoacoustic images, colour photographs were taken during cryoslicing (see appendix).

7.2.3 Results

Figure 7.1 shows optoacoustic images of arteries of the thorax and neck in mice. The images reveal clear signals from the aortic arch and the carotid arteries captured in transverse slices. In particular, figure 7.1a shows a slice through the top of the aortic arch and figure 7.1b shows a slice approximately 2mm above the aortic arch, revealing the innominate artery and the left common carotid artery. Figure 7.1c shows the carotid arteries near the point of bifurcation, a frequent location for atherosclerotic plaque formation [97], approximately 10mm in the cranial direction from the aortic arch. Here the carotid arteries are at a depth of approximately 5mm from the ventral skin surface. Figure 7.1d-f show colour photographs of cryosections at corresponding slices confirming the anatomical structures seen in the optoacoustic images. The optoacoustic images also show strong contrast from blood vessels apart from the arteries mentioned, for example the superior vena cava.

7.2.4 Discussion

The carotid arteries in mice have a diameter on the order of hundreds of micrometers and are shielded by absorbing structures, such as the large veins of the neck, therefore presenting a challenging imaging target. Nevertheless, as evident in the results, these structures, as well as the aortic arch, are within the imaging capabilities of MSOT, which, in the particular implementation applied, has sufficient sensitivity and resolution. Combined with the proven ability of MSOT to detect exogenous optical agents, molecular imaging studies of atherosclerosis in mice have a promising future with clear advantages over the pure optical imaging modalities employed today.

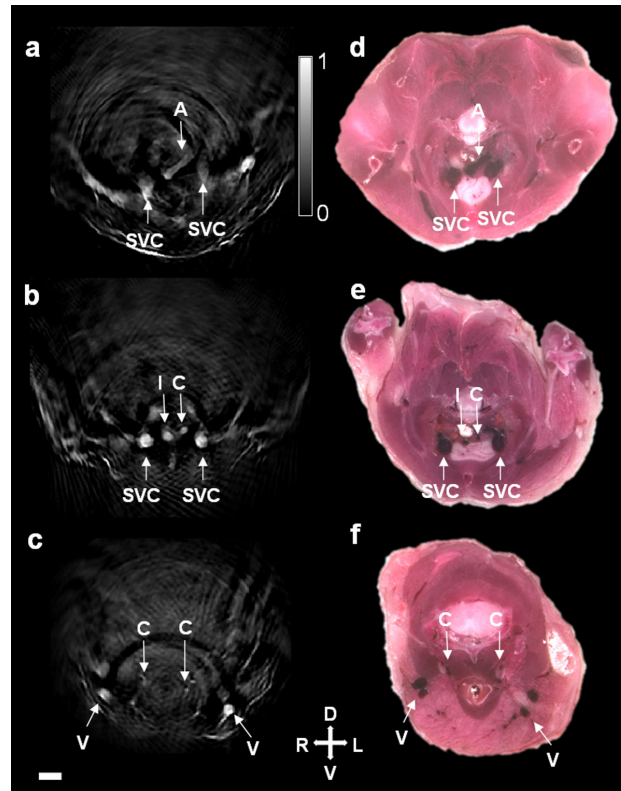


Figure 7.1: Transverse optoacoustic slices showing arteries in the upper thorax and neck (750nm excitation). a: Slice through top of aortic arch. A - Aortic arch. SVC - Left and right superior vena cava. b: Slice showing arteries just above aortic arch. I - Innominate artery, C - left common carotid artery, SVC - left and right superior vena cava. c: Slice approximately 10mm cranially from aortic arch showing carotid arteries near bifurcation. C - Carotid arteries, V - veins branching from external jugular vein. Scale bar: 2mm. d-f: Photographs of cryosections showing corresponding anatomical structures to the images in a-c respectively. Reproduced from [34].

7.3 Challenges of cardiac MSOT

7.3.1 Introduction

The heart presents a crucial but highly challenging imaging target. The major challenges of the heart are:

- Since the heart is filled with blood, and the myocardium itself has a high hemoglobin content, the organ as a whole displays a high optical absorption. This limits the penetration depth of optical imaging approaches.
- The heart is adjacent to the lungs, which strongly attenuate ultrasound propagation.
- The heart is a moving target. In mice the heart beats at a rate of hundreds of beats per minute. Additionally, respiration motion in the region of the heart is strong because it shares the thoracic cavity with the lungs. This motion can lead to blurring in almost all imaging modalities if it is not dealt with in some manner.

The following sections will discuss each of these challenges in turn.

7.3.2 Optical attenuation through the mouse heart

The first challenge, strong optical absorption, dictates the use of a sufficiently high dynamic range optoacoustic measurement system to be able to record the strong signals originating from the ventral side of the heart as well as the weaker signals from the dorsal side where the light has already undergone much attenuation. Using numbers for optical properties derived from the literature [19], and an estimation that the dorsal boundary of the mouse heart is approximately 6mm deeper from the skin surface than the ventral boundary, we can roughly estimate the light attenuation through the heart. Applying $\mu_a = 0.4\text{cm}^{-1}$ and $\mu'_s = 25\text{cm}^{-1}$ to the approximation for plane wave illumination (equation 2.2), we have: $\mu_{eff} = \sqrt{3\mu_a(\mu_a + \mu'_s)} = \sqrt{3 \times 0.4(0.4 + 25)} = 5.5\text{cm}^{-1}$ and at 6mm depth: $\frac{\phi(6\text{mm})}{\phi_0} \approx e^{-(5.5 \times 0.6)} = 0.037$, meaning that the dorsal side of the heart only experiences roughly 4% of the fluence at the ventral side. This calls for instrumentation which is highly sensitive and has a sufficient dynamic range.

7.3.3 Ultrasound attenuation in the thorax

Ultrasound detection through the lungs is impractical: huge differences between the acoustic impedance of tissue and air result in almost no transmission at boundaries. Experimental results in the literature have confirmed that the ultrasound attenuation in lung tissue is vastly higher than in other tissue [98]. Thus, optoacoustic signals from the heart must be acquired from detectors on the ventral side of the animal.

However, a further unknown acoustic obstacle remains: the optoacoustic signals must be detected through the rib cage. While clinical diagnostic ultrasound of the heart typically entails detection through gaps between individual ribs, the dimensions involved in mouse imaging require detection through the rib cage as a whole. To characterise the ultrasound attenuation of the murine rib cage, I performed *ex vivo* measurements in an optoacoustic testbed (figure 7.2a). (These results were reported in 2010 [34].) The goal was to identify to what extent the rib cage could hinder MSOT imaging of the mouse heart under conditions close to those of *in vivo* experiments. Intact rib cages (pictured in 7.2b) were excised from two freshly sacrificed adult CD-1 mice and placed in the testbed. A broadband ultrasound signal was generated by illuminating a carbon rod of approximately 0.5mm diameter with a nanosecond laser pulse. The signals were measured using a piezoelectric ultrasound transducer (Model V382, Panametrics NDT) with a central frequency of 3.5MHz, a bandwidth of 76%, cylindrical focus (focal length 3.8cm) and an element diameter of 13mm. This wide diameter allowed for the signal to be measured simultaneously through a range of different regions in the rib cage in a similar way to the expected experimental conditions. The time-resolved signals detected by the transducer were digitized and averaged (2000 times) by an embedded oscilloscope card (NI PCI-5122, National Instruments) at 100MSamples/s.

The recorded signals in the presence (figure 7.2c solid line) and the absence (figure 7.2c dotted line) of a murine rib cage in the acoustic path provide the first insights into the feasibility of cardiac MSOT in mice. The signal acquired through the rib cage demonstrates slight attenuation compared to the baseline measurement, but is otherwise very similar in amplitude and shape. A more quantitative picture is provided by the insertion loss of the rib cages calculated from the measurement data (figure 7.2d). Even at a frequency of 3.5MHz, corresponding to a spatial resolution of 215 μ m, there is only an attenuation of approximately 3dB. This shows that only moderate attenuation is expected from the rib cage, leading to the conclusion that *in vivo* MSOT of the mouse heart is not expected to suffer from insufficient signal-to-noise ratio as long as signals from the heart are acquired on the ventral side, that is, not through the lungs.

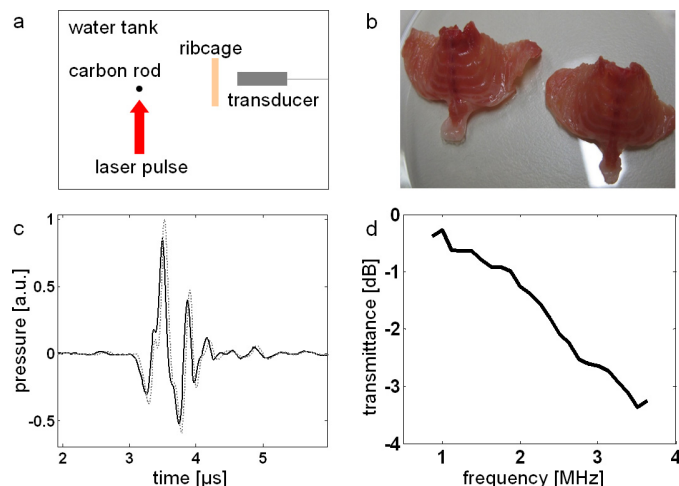


Figure 7.2: Determination of ultrasound attenuation through the rib cage.

7.3.4 Motion

Two major sources of motion complicate imaging of the thorax: respiration and heartbeat. Independent of imaging modality, if the object being imaged moves on a scale higher than the imaging resolution during data acquisition, the resulting images will be blurred. Generally, this problem can be overcome by triggering or synchronisation schemes linked to monitoring of the animal's heartbeat and respiration. In MSOT, and in particular in the implementation under discussion here, an entire 2D slice image is acquired at once. The acquisition time is essentially the time it takes the relevant ultrasound signals to propagate from the animal to the transducer array. With a 4cm focal distance, additionally assuming a mouse radius of 1cm and a speed of sound in water or tissue of 1500m/s, all the information in a slice through the mouse can be acquired within $\frac{(4+1) \times 10^{-2}}{1500} = 33.3\mu\text{s}$. This fast acquisition time allows single wavelength imaging virtually free of motion artifacts. However, detection of functional or molecular parameters requires several such images taken at different times, either to show a change in contrast over time, or when using multiple excitation wavelengths to resolve specific spectral signatures. Motion certainly occurs between single pulse images: in our implementation the pulse repetition rate, and therefore the frame rate, is 10Hz, meaning that 100ms pass between individual images. Changes in wavelength demand even more time: in OPO implementations the mechanical rotation required could take seconds. Nevertheless, the fact that entire slice images are generated per pulse makes possible alternative, data-driven schemes for solving problems related to motion. There are many conceivable automated processing techniques that can be applied to this problem, an example of which is described in section 7.5.

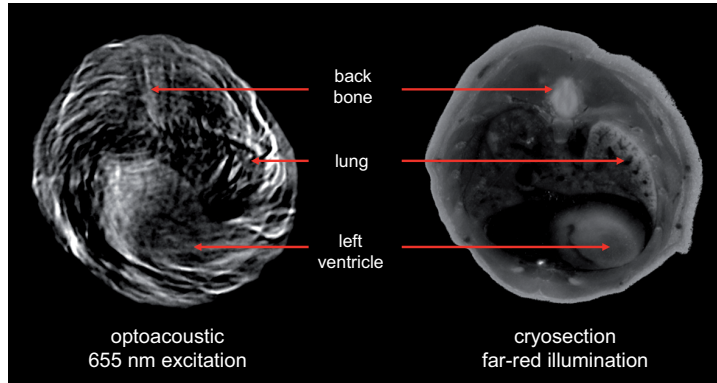


Figure 7.3: Optoacoustic image of the heart from single detector system.

7.4 Initial imaging of the heart

7.4.1 Imaging of the heart with full projection data

To initially investigate the potential of macroscopic MSOT imaging of the heart, which at the time had not been reported except for a low-detail image by Kruger et al. [11], we imaged mice, *post mortem*, in the thorax region, employing the single detector MSOT system (section 3.5.1). Signals were acquired at 2500 angular projections per slice during continuous rotation of the mice around 360° , resulting in an acquisition time of 83s per slice and wavelength. A representative example image is shown in figure 7.3. Encouragingly, several important anatomical structures are visible in the image. The myocardium of the left ventricle can be distinguished, as it absorbs less light than the adjacent blood pool. Overall, the anatomical features correspond well to the reference cryosection shown in the same figure. Interestingly, although the lungs should pose an almost impassable barrier to ultrasound propagation, the whole cross-section through the mouse is visible. This is due to the use of full 360° sampling of the acoustic field: the optoacoustic signals are detectable from at least one side, where the lungs are behind the signal sources. The lungs themselves are largely dark: as expected it is not possible to detect signals from them.

7.4.2 Real-time imaging of the heart

As discussed in section 7.3.3, capturing optoacoustic signals from the heart is only practical from the ventral side. As such, the newly developed real-time small animal MSOT system (section 3.5.2) has a well-suited detection geometry: by placing the mouse in a prone position, the detector array faces the ventral side of the thorax. This opened up the possibility of *in*

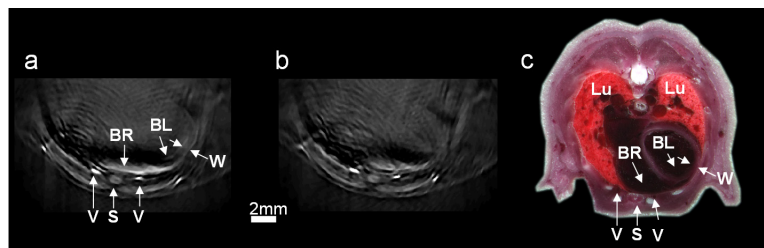


Figure 7.4: Optoacoustic heart imaging at 740 nm excitation. a: Single-pulse image showing heart wall (W). Also visible are signals from blood inside the left and right ventricles (BL and BR) and the sternum (S) and veins (V). b: Single-pulse image taken during ventricular systole. c: Photograph of cryosection through the heart of a mouse showing features corresponding to optoacoustic images.

in vivo real-time optoacoustic imaging of the heart, for which there was no known precedent. Mice were imaged by the same procedure as described in section 7.2. The imaging results showed that it was possible to image anatomical features of the heart from single laser pulses, that is, that real-time imaging was feasible. The results are summarised in figure 7.4. The following facts are notable:

- Among other anatomical features, it is possible to distinguish the wall of heart, in particular on the ventral side of the left ventricle, from the surrounding tissue (see figure 7.4a). This is understood to be possible because of the lower hemoglobin concentration in the myocardium compared to in the blood pool inside the heart chambers.
- Each frame produced from a single laser pulse produces a snapshot of a particular stage of the cardiac cycle. The individual frames can be distinguished from another, for example, those originating during diastole (figure 7.4a), and those from ventricular systole (figure 7.4b).

Note also the difference in acquisition time to the experiments described in the previous section: the image shown in figure 7.3 took 83s to acquire, whereas 10 images like those shown in figure 7.4a&b were acquired per second in the real-time system. The potential for MSOT visualisation of the heart was thus established.

7.4.3 Multispectral imaging of the heart

The next logical step was to perform multispectral measurements of the heart to give an indication of the information that can be extracted from

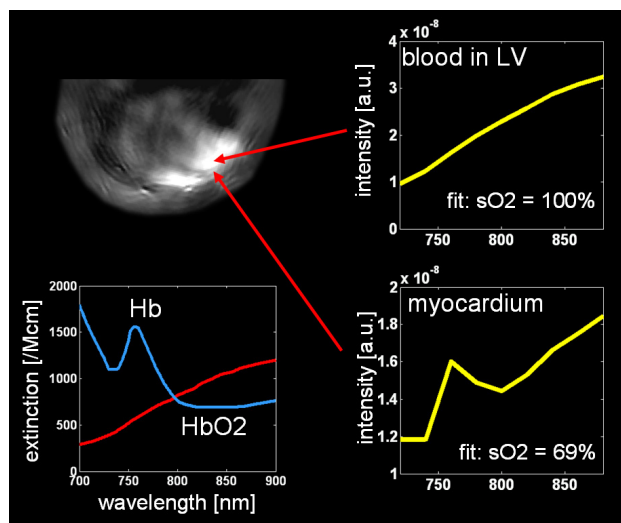


Figure 7.5: MSOT imaging of the heart: hemoglobin contrast. Combinations of oxy- and deoxyhemoglobin fitted to the measured data are shown for two representative pixels.

this important organ by adding the spectral dimension. To this end, mice were imaged in a prone position in the real-time MSOT system at wavelengths from 720nm to 880nm in steps of 20nm with 100 frames averaged per wavelength. Figure 7.5 shows an MSOT image through the ventricles (excitation 860nm). The myocardium can be distinguished as the darker walls around the bright areas corresponding to the blood pools inside the ventricles. This contrast becomes clearer at wavelengths longer than 800nm, as the absorption of oxyhemoglobin increases over the absorption of deoxyhemoglobin, resulting in less signal from the less oxygenated myocardium compared to the blood inside the ventricles. Using linear spectral unmixing and applying the formula for hemoglobin oxygen saturation (equation 4.5), it is possible to see whether the resulting spectra fit our expectations. The results for two representative single pixels are shown: one in the myocardium of the left ventricle, and a second inside the blood pool of that chamber. The results are encouraging: as expected, the blood pool inside the left ventricle displays an MSOT spectrum that fits to oxygenated hemoglobin, whereas the tissue of the myocardium displays a mixed spectrum yielding a fit of 69% hemoglobin oxygen saturation. While there is no simple way to validate these results, the values are highly plausible and indicate the potential of MSOT imaging of the heart.

7.5 Clustering for cardiac motion correction

7.5.1 Purpose

While parallel multi-element ultrasound detection enables real-time optoacoustic imaging, the added spectral dimension needed for MSOT imaging of specific contrast requires the same images to be separately acquired at multiple wavelengths. A naive approach where single frames from each wavelength are used for spectral unmixing would yield unpredictable results because of the arbitrary combination of stages of the cardiac cycle from which the images originate. A more robust uncorrected approach is to acquire several frames for each wavelength and average them, producing a blurred representation of all stages of the motion, on which spectral unmixing can then be applied. The resulting motion-blurred MSOT images are the baseline from which we aim to improve in this work, by automatically grouping or clustering images according to their similarities prior to spectral unmixing. The approach, along with the results that follow, have been submitted for publication under the title *Motion clustering for deblurring multispectral optoacoustic tomography (MSOT) images of the mouse heart*.

Several established imaging modalities (PET, SPECT, CT, MRI) employ triggering/gating or synchronisation schemes that only activate data acquisition during the same stage of the cardiac cycle. This would be possible in MSOT imaging too. But it would require heart monitoring systems and external triggering of the laser source, causing added complexity, and increased acquisition times because the laser would not fire at the maximum possible rate. A more suitable solution is therefore not to change the acquisition protocol, but rather group together sets of images corresponding to similar stages in the cardiac cycle. To this end we can apply a clustering algorithm, k -means in this case, to separate single pulse images acquired at each wavelength according to the stage of the cardiac cycle to which they belong.

In the following, I will describe the method and show experimental results.

7.5.2 Method

Algorithms for k -means seek to minimize the sum of the distances from each data point to the mean of the cluster it is assigned to, that is [99]:

$$\operatorname{argmax}_S \sum_{i=1}^k \sum_{x_j \in S_i} [1 - \operatorname{corr}(x_j, \mu_i)], \quad (7.1)$$

where S is the set of clusters S_1, S_2, \dots, S_k , x_j is the data point in question, and μ_i is the mean of the points in the cluster S_i . Note that the distance measure used in this case is 1 minus the correlation. We used the standard Matlab (The MathWorks) implementation of the algorithm (function *kmeans*), which uses heuristics since the problem is generally NP-hard. While it is possible to set initial mean values or *seeds* according to manual selection of images, this was not done here. Initial values were chosen at random from the dataset, that is, the algorithm is fully automatic. The clustering was performed with $k = 2$. This value is intuitive because the motion of the ventricles has two turning points: when the left ventricle is most contracted during ventricular systole, and when it is most relaxed during diastole. The experimental protocol was as follows:

1. We recorded 100 frames (single pulse images) of the heart at each of the following excitation wavelengths: 700nm, 730nm, 760nm, 800nm and 860nm (real-time system section 3.5.2).
2. Each of the single pulse images, 500 frames in total, were reconstructed using delay-and-sum.
3. Prior to clustering, the images were reduced to a manually selected region-of-interest (ROI) corresponding to the location of the heart. This was performed for two reasons: first, so that the motion of the heart would be the major contributor to clustering distances, and second, to reduce computation time.
4. A k -means clustering algorithm was applied per wavelength to partition each of the 100 images into $k = 2$ clusters.
5. The images belonging to each resulting cluster were then averaged so that this separated data could be compared to the uncorrected case where all 100 frames were averaged.
6. Finally, spectral unmixing using the known spectra of oxy- and deoxy-hemoglobin was applied to the two data sets formed by averaging the frames belonging to each cluster.

7.5.3 Results

It is the quality of the single pulse images that allows motion to be resolved on a frame-by-frame basis. The heart is visible and it is possible to distinguish the myocardium from the blood pool inside the ventricles in these images (figure 7.6). By inspection, it is possible to distinguish those frames where the left ventricle is relaxed (diastole) from those where it is contracted

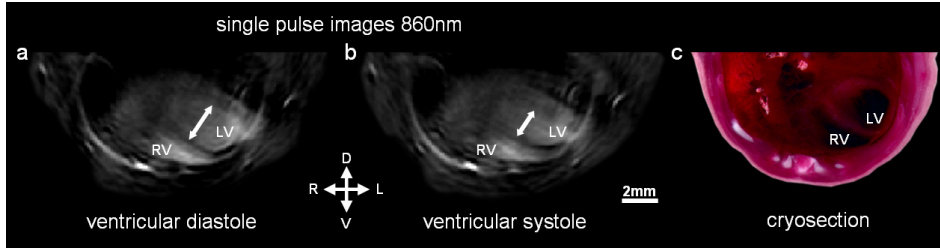


Figure 7.6: Single pulse optoacoustic images of the heart at 860nm excitation. LV: left ventricle, RV: right ventricle. a: Selected image during diastole. b: Selected image during systole. c: Corresponding cryosection through the ventricles.

	700nm	730nm	760nm	800nm	860nm
large cluster	55	59	59	59	57
small cluster	45	41	41	41	43

Table 7.1: Amount of frames assigned to each cluster per wavelength.

(systole), as can be seen in the comparison of two selected frames in figure 7.6. The images agree well with the corresponding *ex vivo* cryosection.

Clustering for each of the 5 wavelengths resulted in assignments where one cluster contained, on average, 57.8% of the total frames (results summarized in table 7.1). On inspection it was found that the cluster to which the majority of the frames was assigned represented the diastole stage. This result is expected since it is well known that the duration of diastole is longer than systole.

After clustering and subsequent averaging over each cluster, for each wavelength, the myocardium is still easy to distinguish from the blood pool in the ventricles and the averages for each of the clusters represent diastole and systole respectively (see figure 7.7). When compared to the averaged image over all frames (figure 7.7c), the separately averaged images display a clearer delineation of the left ventricle, that is, reduced motion blurring.

Of greater importance, however, are the results after spectral unmixing, where all wavelengths are taken into account. As expected, after separately unmixing each of the two clusters, we obtain MSOT images for distinct stages in the cardiac cycle with reduced motion blurring as compared to the images when all frames are averaged (figure 7.8). From the images of deoxyhemoglobin contributions, we can resolve the outline of the left ventricle from the more oxygenated blood pool. By comparing the unmixed images from the large cluster (figure 7.8b) with the smaller cluster (figure 7.8c), it is clear that clustering for each wavelength and subsequent spectral

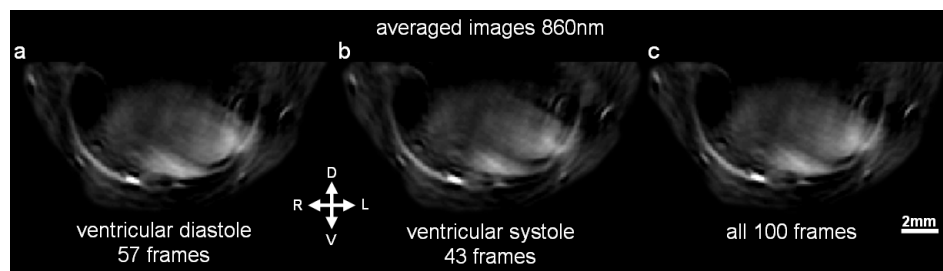


Figure 7.7: Averaged images with and without clustering, taken at 860nm. a: Averaged image over cluster corresponding to diastole. b: Averaged image over cluster corresponding to systole. c: Averaged image over all 100 frames.

unmixing produced distinctive images of diastole and systole respectively. The corresponding image without clustering (figure 7.8a) is a combination of both and is consequently more blurred. From a profile through these images (figure 7.8d) we observe that the averaged MSOT image over all frames is a mix of diastole and systole and loses some sharpness in the edges of the left ventricle compared to the images after clustering. Additionally, since the wall of the left ventricle is clearly defined in the MSOT images, we can segment the areas inside the chamber for comparison between the uncorrected case and the two clusters. As shown in figure 7.9, the segmented area in the uncorrected case has a value between the areas found from the separated clusters.

7.5.4 Discussion

The results in mice show that this method can cluster images according to the stage of the cardiac cycle to which they belong, allowing subsequent spectral processing to be performed separately for each stage, therefore resulting in images with reduced motion blurring compared to when no clustering is performed. The additional processing of 100 frames each at 5 wavelengths took approximately 7s, indicating that the method has potential to be adapted for use during experiments: new frames could be clustered as they arrive, allowing high resolution results to be displayed immediately. There are some compromises and limitations involved in resolving motion in MSOT imaging by clustering. Dividing frames into 2 clusters is the simplest case possible. Increasing the number of clusters could further reduce motion blurring, but reducing the amount of frames per cluster would simultaneously reduce the signal-to-noise ratio, as less signal averaging would occur. Also, the ability of an algorithm to successfully perform clustering based on motion would be reduced with an increasing amount of clusters, because

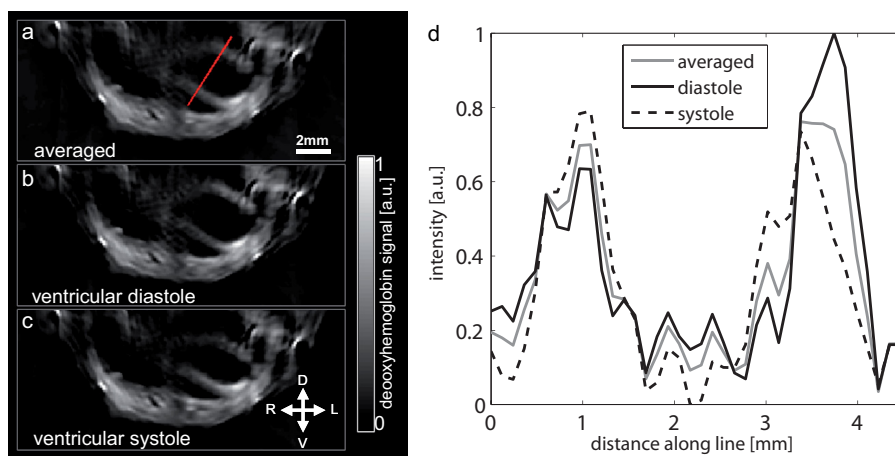


Figure 7.8: Motion correction for unmixed deoxyhemoglobin contribution. a: Unmixed image after all 100 images were averaged for each wavelength. b: Unmixed image after averaging only the larger clusters for each wavelength. c: Unmixed image after averaging only the smaller clusters for each wavelength. d: Profile along red line through left ventricle on a, comparing the images after clustering to the averaged (no clustering) image.

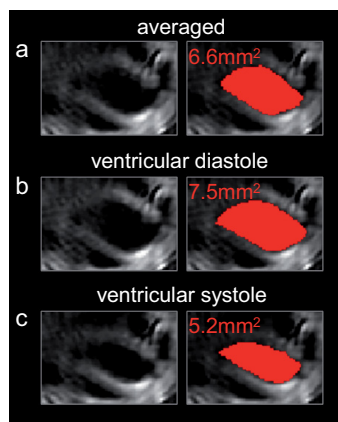


Figure 7.9: Areas inside left ventricle after motion correction. The red filled regions represent manual segmentations.

the distances between the clusters would drop. Generally, in an intuitive approach the number of clusters would be chosen to reflect the amount of motion and the number of components of motion (for example, two clusters for heartbeat and one for respiration) in the particular imaging scenario in question.

The quality of the MSOT images of the heart, in particular the unmixed images in figure 7.8, where the entire myocardium of the left ventricle is visible, points to applications in studies of myocardial infarction where multichannel, high resolution measures of the pathology could be extracted *in vivo*. While I have demonstrated the method in the context of cardiac imaging and motion from the heartbeat, it can be more generally applied to other anatomical regions and other sources of motion, such as respiration. Similarly, there is no reason to restrict this method to small animal imaging: clinical applications of MSOT can equally be affected by motion from respiration, heartbeat and pulse. Motion correction should be considered an essential part of MSOT imaging, since one of the primary advantages of the modality is its high spatial resolution, which can be degraded *in vivo* because of motion blurring.

7.6 Preclinical cardiovascular disease

7.6.1 Purpose

Several examples of optical molecular imaging of cardiovascular disease can be found in the literature. FMT studies of myocardial infarction have shown macrophage infiltration using magneto-fluorescent nanoparticles [16]. FMT imaging contributed to the finding that the spleen is a significant reservoir for monocytes deployed to myocardial infarction, reported in 2009 [100]. Plainly, *in vivo* optical imaging already plays a major role in cardiovascular disease research. MSOT has the potential to add to these technological capabilities by allowing higher resolution, and imaging of functionally important tissue-intrinsic absorbers like hemoglobin. Consider, for example, the site of a heart infarct. Perfusion can be measured by the concentration of oxyhemoglobin in that region. Organic dye or nanoparticle-based molecular probes could give information on biological processes. Cell labelling could give insights into basic biology or enable tracking of cell therapy. The following specific aims were investigated in studies using a mouse model of myocardial infarction:

- What information can be extracted from MSOT images of myocardial infarction? Note that these were, to our knowledge, the first *in vivo* optoacoustic studies on a model of myocardial infarction, so the

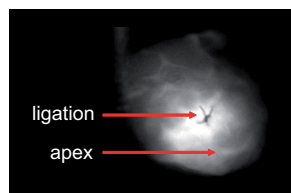


Figure 7.10: Fluorescence reflectance image showing integrin-targeted agent in excised mouse heart with infarct.

outcomes were highly uncertain.

- Is it feasible to resolve the distribution of a molecular imaging agent relevant to infarction in an injured myocardium by MSOT? What distinguishes the results from those obtained by other optical imaging methods?

7.6.2 Method

7.6.2.1 Mouse model

In the imaged mouse model, myocardial infarction is induced by permanent ligation of the left coronary artery. A representative example of a mouse heart which has undergone this procedure is shown in figure 7.10. In this case, the mouse was injected with an integrin targeting fluorescent agent (IntegriSense680, PerkinElmer) a week after inducing the infarct. 24 hours after injection, the heart was excised and imaged using near-infrared fluorescence (NIRF) in a planar reflection geometry. The image thus shows fluorescence resulting from the injected agent, which highlights the infarcted tissue. The ligation can be seen in the image. Elevated fluorescence levels can be observed around the ligation, and going down towards the apex of the heart, where infarction was induced. The surgery involved is a standard procedure and is described by Nahrendorf et al. [101] (also in the context of optical imaging). A significant but unavoidable drawback of this method is that it leaves behind a wound (figure 7.11 shows a representative example). This wound, which goes from the skin surface through the ribcage to the heart, can itself lead to molecular agent accumulation due to the biological processes involved in wound healing. The increased optical attenuation due to hemoglobin accumulations in the wound and increased thickness of the tissue between the skin surface and the heart, as well as possible acoustic mismatches from hardened blood on the surface of the wound, could cause a decrease in MSOT image quality when compared to untreated mice.



Figure 7.11: Mouse with induced myocardial infarction (*post mortem*).

7.6.2.2 Inflammation-targeted agent

To investigate MSOT imaging of an optical agent in myocardial infarction, we employed an agent consisting of dendritic polyglycerolsulfate (dPGS) with covalent ICG-derived dye. The agent was described in a therapeutic (anti-inflammatory) application by Dervedde et al. in 2010 [102], where it was shown to bind to L- and P-selectin. Approximately 5 dyes were attached per polymer, resulting in a high optical absorption and thus a strong MSOT response. While the fluorescence efficiency is low due to quenching (claimed quantum yield less than 1%), there is enough fluorescence to serve as a validation method. The following steps were taken to validate specific MSOT detection of the dPGS:

1. The absorption spectrum of the agent was measured in a spectrometer.
2. The optoacoustic spectrum was characterised by imaging an inclusion of the agent in solution inside a cylindrical, optically scattering phantom. Measurements were performed with excitation from 695nm to 900nm in steps of 5nm. After image reconstruction, the mean pixel values in the agent inclusion were used to obtain the intensity values for each wavelength.
3. The spectra recorded from the above measurements were compared to spectra obtained using blind source unmixing in subsequent *in vivo* experiments which will be described in the following section.

Note that the dPGS was measured in solutions containing 10% albumin (a plasma protein) to simulate *in vivo* conditions. As with ICG, dPGS appears to bind to albumin to some extent, causing a change in its absorption spectrum.

7.6.2.3 Mouse imaging protocol

Heart infarcts were induced by surgery as described in section 7.6.2.1. The imaging studies were performed two days later as follows:

1. Each mouse was positioned in the real-time MSOT imaging system (section 3.5.2) in a prone position, and live images were used to determine the region to scan, going from the liver up to the top of the heart.
2. An MSOT reference scan (prior to injection) was captured at the following eight wavelengths: 710nm, 730nm, 760nm, 790nm, 800nm, 820nm, 850nm, 900nm. 100 frames (laser pulses) were acquired per wavelength and slice. Slices covering the scan region were acquired at 1mm intervals in the elevational direction. The acquisition time per slice was approximately 100s.
3. Approximately 8mg/kg of dPGS was injected intravenously (tail vein).
4. Further MSOT measurement data was acquired as described for the reference scan at times of 5-20 minutes, 1 hour and 2 hours after injection.
5. The mouse was then euthanised, frozen at -80°C and later sliced using FCSI (see appendix) for validation.

The following steps were taken to reconstruct the MSOT images:

1. Each frame was reconstructed separately using delay-and-sum.
2. For each slice and wavelength, clustering was performed to separate frames by motion as described in section 7.5.
3. Blind source unmixing by Independent Component Analysis (ICA, section 4.3.2) was performed on each cluster to obtain images of the distribution of dPGS or other selected absorbers.

In this way, MSOT images corrected for cardiac motion were obtained.

7.6.3 Results

Initial imaging results show that while there is a decrease in MSOT image quality of the heart compared to untreated animals caused by the operation wound, the obtained images nevertheless reveal critical morphological information useful to studies of myocardial infarction. Figure 7.12 shows

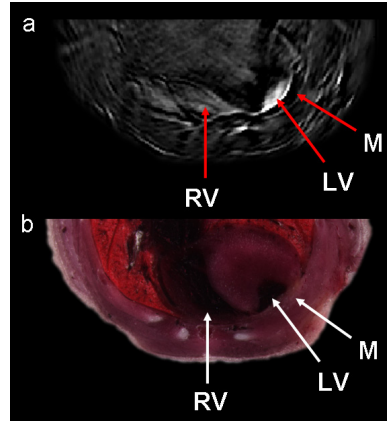


Figure 7.12: Anatomical features in an MSOT image of a mouse with myocardial infarction. a: MSOT image unmixed for oxyhemoglobin. LV - left ventricle, RV - right ventricle, M - visibly thinned myocardium at site of infarct. b: Corresponding cryosection.

intrinsic MSOT contrast gained from a mouse with a severely thinned myocardium due to infarction. The MSOT image unmixed for oxyhemoglobin (figure 7.12a) is confirmed by a corresponding cryosection (figure 7.12b). In particular, the thinned myocardium at the site of infarction is visible in the MSOT image, clearly distinguishable from the oxygenated bloodpool in the left ventricle adjacent to it. This difference in contrast between the myocardium at the site of infarction and the surrounding tissue in this mouse model is an important prerequisite for MSOT imaging studies where agent distributions should be localised to specific anatomical regions.

Figure 7.13 summarises the results from spectroscopic measurements of the inflammation targeted agent, dPGS. The spectrometer measurement shows two characteristic absorption peaks in the near-infrared, the larger one being in the vicinity of 800nm. The MSOT phantom measurement provides data points at 5nm steps that yield an overall shape closely resembling that of the spectrometer reading. The unmixed *in vivo* MSOT spectrum was obtained from imaging data described below, using ICA. Again, the spectrum closely resembles the spectrometer reading and the optoacoustic spectrum measured in the phantom, serving to validate the performance of MSOT using blind source unmixing to resolve the targeted agent. Slight differences in the curves are thought to be a result of differences in the amount of agent bound to plasma proteins in the different experiments, as well as differences in the spectrum of the incident light in the case of the MSOT measurements due to wavelength-dependent light attenuation with depth.

The *in vivo* imaging results (figure 7.14) demonstrate the feasibility of detecting optical molecular agents in heart infarcts by MSOT. Most impor-

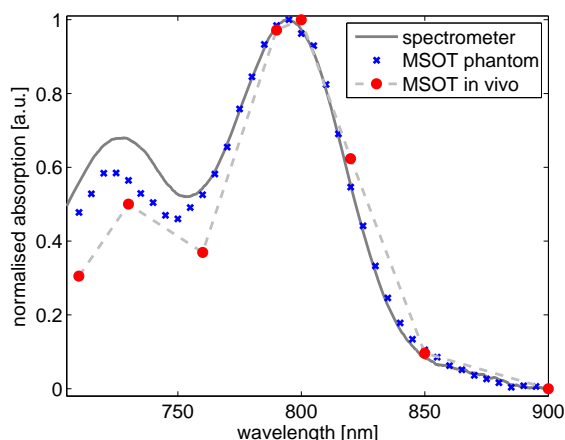


Figure 7.13: The spectrum of dPGS measured in a spectrometer, in a cylindrical MSOT phantom, and extracted by ICA from an *in vivo* measurement on a mouse model of myocardial infarction.

tantly, signals are detected from corresponding locations in the myocardium of the left ventricle in both the MSOT image (figure 7.14b) and the NIRF cryosection (figure 7.14d). From the 900nm image (figure 7.14a) it is possible to distinguish the myocardium of the left ventricle from the surrounding tissue, as validated by the colour cryosection image (figure 7.14b). An area around the ligation visible in the cryosection appears darker in the 900nm image than other parts of the myocardium: a possible explanation for this could be reduced perfusion in this region, leading to a lack of contrast-producing hemoglobin.

Figure 7.15 shows MSOT results from multiple imaging time points for a further experimental subject. As can be observed from the MSOT images, there is already some signal originating in the myocardium as early as 15 minutes after injection (figure 7.15a); at the later times (figure 7.15b&c) it shows a strong increase. Because we are able to identify the heart wall in the MSOT images (900nm grey-scale backgrounds), we can distinguish between probe signals from the infarcted myocardium, and the inflamed operation wound. Such distinctions are difficult to make at the lower spatial resolutions typical of deep-tissue optical imaging today.

7.6.4 Discussion

The MSOT imaging results presented above in the context of myocardial infarction show, for the first time, that it is possible to resolve optical molecular agents in the injured myocardium. Many factors led to these successful

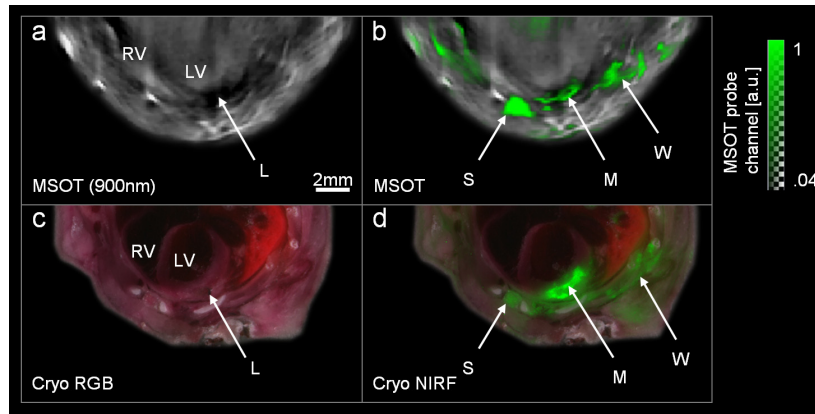


Figure 7.14: MSOT of targeted agent in the heart (2h post injection). a: Anatomical MSOT image taken at 900nm. L - region of reduced optoacoustic signal in myocardium, presumably from lower hemoglobin levels. b: MSOT overlay showing dPGS signal in green. M - signal from myocardium, S - signal from sternum. W - signal from wound. c: Colour photograph of corresponding cryosection. L - injured region around ligation corresponding to area of reduced optoacoustic signal. d: Near-infrared fluorescence overlaid in green on colour image. Labels correspond to those on MSOT image.

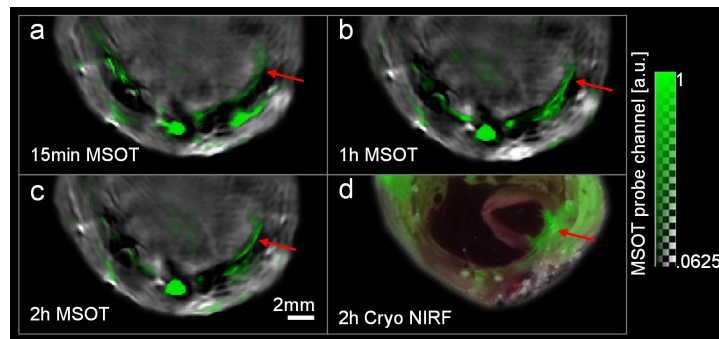


Figure 7.15: MSOT reveals inflammation-targeted agent in a heart infarct. a: MSOT image showing dPGS signal 15 minutes after injection overlaid on 900nm image for anatomical reference. b: The same image 1 hour after injection, and c: 2 hours after injection. d: A corresponding fluorescence cryosection image for validation. The red arrows point to signal on the anterior left ventricle, believed to be infarcted.

results. A geometry suitable for detection of optoacoustic signals from the ventral side of the animal, as employed here, is essential to avoid ultrasound attenuation through the lungs. Real-time imaging allows the motion of the heart to be resolved, which can then be corrected for using the presented clustering technique, resulting in higher quality images. Suitable spectral processing methods, such as ICA, are required to resolve the presence of the spectral signature of the optical agent in the complex tissue background. Although the operation wound resulting from the particular animal model employed here reduces the quality of the images, it is still possible to identify the anatomy sufficiently well to robustly distinguish between agent signals originating from the infarcted myocardium, and the wound. Overall, such performance in optical imaging of disease biomarkers will surely be applied to further studies, not only of myocardial infarction, but a range of disease models in which high resolution images of optical contrast would provide valuable new insights.

7.7 Clinical potential

There is no conceivable reason to restrict the cardiovascular imaging capabilities of MSOT to preclinical small animal imaging. A number of research efforts have been directed to the development of multispectral optoacoustic catheter systems for the diagnosis of atherosclerosis (Sethuraman et al. [45] and Jansen et al. [46] are salient examples). Also, the feasibility of detecting matrix-metalloproteinase activated optical agents in human atherosclerotic plaque specimens has been shown by Razansky et al. [87] at our institute in 2011. Noninvasive clinical imaging of cardiovascular disease by MSOT will almost surely become an active research topic in the coming years. For example, Khalil et al. have recently demonstrated the potential of pure optical tomography in diagnosing peripheral artery disease by vascular dynamics [103]: this kind of imaging scenario seems ideally suited for MSOT imaging, which would enable a higher resolution as well as real-time visualisation.

7.8 Concluding remarks

This chapter has investigated MSOT as a method to image several important aspects of the cardiovascular system macroscopically and noninvasively in mice, including the aorta, the carotid arteries, and the heart *in vivo* and in real-time. A number of unprecedented results were unveiled: the first high resolution MSOT images of the aortic arch and carotid arteries in mice, detailed multispectral slices through the ventricles of the heart, motion corrected images separating the major phases of the cardiac cycle,

and the first MSOT imaging resolving a targeted agent in a mouse model of heart disease *in vivo*. The ability of MSOT imaging to resolve anatomical structures which feature in the research and diagnosis of cardiovascular disease enables promising applications of the technique in this field. In the thorax, the problem of high ultrasound attenuation posed by the lungs is overcome by acquiring the optoacoustic signals through the front of the chest where the rib cage has been experimentally shown to pose no great obstacle to ultrasound. The results show the heart in detail, able to clearly distinguish the anterior heart wall from blood inside the heart chambers. For multispectral imaging of the heart, where motion (due to respiration or heartbeat) between different wavelengths requires, in the absence of cardiac or respiratory synchronisation or triggering methods, averaging of multiple signals, anatomical structures can still be recognized. Selection of images at similar points in the cardiac cycle improves averaged image quality, and a clustering algorithm has been demonstrated to perform such separations automatically. In addition to the possibility to extract morphological information and intrinsic tissue chromophores from the images, exogenous contrast agents highlighting biological targets in the myocardium provide a powerful method for molecular imaging of the heart. The results demonstrating the ability of MSOT to resolve a targeted optical agent in a model of myocardial infarction show the potential of such applications as visualisation of infarct healing or inflammation in atherosclerotic plaques. Furthermore, the macroscopic imaging performance attained in the demonstrated mouse experiments indicates the possibility of applying these methods to clinical diagnosis of cardiovascular disease, for example on such targets as the carotid arteries in the human neck, or in peripheral artery disease in the legs or feet.

Chapter 8

Imaging cancer

8.1 Introduction

This chapter describes original work related to the imaging of cancer by MSOT. The capabilities of the method are highlighted by experimental results on tumor-bearing mice. Optical imaging plays an important role in tumor visualisation for basic biological research and drug discovery. Fluorescence intravital microscopy is essential in understanding the tumor micro-environment and treatment mechanisms [104], and has allowed significant insights into tumor vasculature and the micro-pharmacokinetics of therapeutics by means of fluorescent tags. But despite the important benefits, microscopy suffers from superficial penetration: imaging depths rarely reach beyond a few hundred microns [6]. Macroscopic near-infrared fluorescence (NIRF) imaging of entire tumor volumes could reveal parameters not captured by microscopy methods, for example, the overall distribution of drug delivery. However, optical macroscopy methods are limited by photon diffusion and are mainly applied as qualitative two-dimensional approaches that conceal information on intra-tumoral biodistribution [6]. The emergence of optoacoustic imaging brings a new ability to tumor studies by allowing high resolution deep-tissue optical contrast and real-time operation. To date, tumor imaging based on the optoacoustic phenomenon has been applied in a limited manner, for example for detection of photo-absorbing nanoparticles [70], developing vascular networks [105, 106], and blood oxygenation saturation in tumors [13].

The hypothesis of this chapter is that MSOT could be employed for real-time high resolution imaging through whole tumors *in vivo*, revealing their heterogeneous vascular characteristics and distributions of specific molecules of interest. Experiments are described in which the ability to image dynamic contrast enhancement of tumor vasculature using a fluorescent dye, and

the visualisation of targeted fluorescent agent distribution was investigated. Additionally, the accumulation over time of long-circulating gold nanorods as well as intratumoral patterns of hemoglobin oxygenation, was imaged, to gain insight into the enhanced permeability and retention (EPR) effect [107], which provides an opportunity for selective drug delivery to tumors. This chapter also presents results demonstrating initial MSOT imaging of gold nanorod-enhanced liposomal nanocarriers for the delivery of therapeutics, highlighting the potential such methods have for pharmaceutical development. The contents of this chapter, excluding the section on gold nanorod-enhanced liposomes, have been submitted for publication under the title *Optical imaging of cancer heterogeneity by means of multispectral optoacoustic tomography (MSOT)*. Results relating to the gold nanorod-enhanced liposomes are currently planned for submission under the title *Multispectral optoacoustic tomography of gold nanorod-enhanced liposomes delivering siRNA*.

8.2 Dynamic imaging of ICG perfusion in tumors

8.2.1 Purpose

The aim of this study was to investigate whether we could resolve a common organic dye dynamically as it enters and leaves the tumor vasculature, and to establish, from the imaging results, any advantages that MSOT detection of organic dyes in tumors might have in comparison to the methods commonly applied today for such imaging: namely intravital microscopy and macroscopic NIRF imaging.

8.2.2 Method

Indocyanine green (ICG) was used in this experiment. ICG is an FDA approved dye in established clinical use [82]. Following intravenous injection, ICG rapidly binds to plasma albumin and b-lipoproteins and leaves the circulation [108]. The experimental protocol was as follows:

1. Adult female nude mice were inoculated subcutaneously on the lower back with 0.8 million 4T1 mouse mammary tumor cells (ATCC CRL-2539) each.
2. Once the tumor reached a diameter of approximately 8mm, the imaging experiments were initiated. The mice were kept under isoflurane anesthesia for the duration of the experiments.

3. A catheter was placed in the tail vein prior to positioning in the real-time MSOT imaging system (section 3.5.2).
4. Guided by real-time optoacoustic images displayed on the system, the mice, in a supine position, were translated so that transverse slices through the tumor could be recorded.
5. Reference images were recorded at multiple slice positions through the tumor. The imaged wavelengths were 725nm, 750nm, 775nm, 800nm, 825nm and 850nm. 100 single pulse images were averaged at each wavelength resulting in an acquisition time of approximately 10s per wavelength.
6. A series of single pulse images was recorded at 790nm, near the absorption peak of ICG. During this acquisition, 97nmols of ICG were injected into the tail vein.
7. After injection, multispectral imaging was performed as described for the reference images. This data was recorded repeatedly at the following time points after injection: immediately afterwards, 20 minutes, 4 hours and 24 hours.
8. The tumor was imaged using planar reflectance NIRF imaging near the 24 hour time point.
9. Images were reconstructed and the individual spectral components (ICG, oxyhemoglobin, deoxyhemoglobin) were resolved using linear spectral unmixing.

8.2.3 Results

The imaging results are summarised in figure 8.1. A photograph (figure 8.1a) shows the subcutaneous tumor allograft: the approximate imaged slice location is indicated by the dashed white line. The results show that the ICG could be detected in two distinct ways. First, during injection of the dye, single pulse images (frames) recorded near the absorption peak of ICG show an increase in contrast in and around the tumor as the dye enters the tumor vasculature. This localised contrast increase is clear when comparing figure 8.1b, taken before the injection starts, to figure 8.1c, taken 30s after the start of injection. Thus it is possible by imaging at a single wavelength in real-time to observe changes over time in absorption, caused here by intravenous injection of a dye. Note that a reference image without the dye is required in this case, since it is impossible to determine which contrast originates from the ICG compared to contrast from tissue absorbers (say hemoglobin) by only considering a single image.

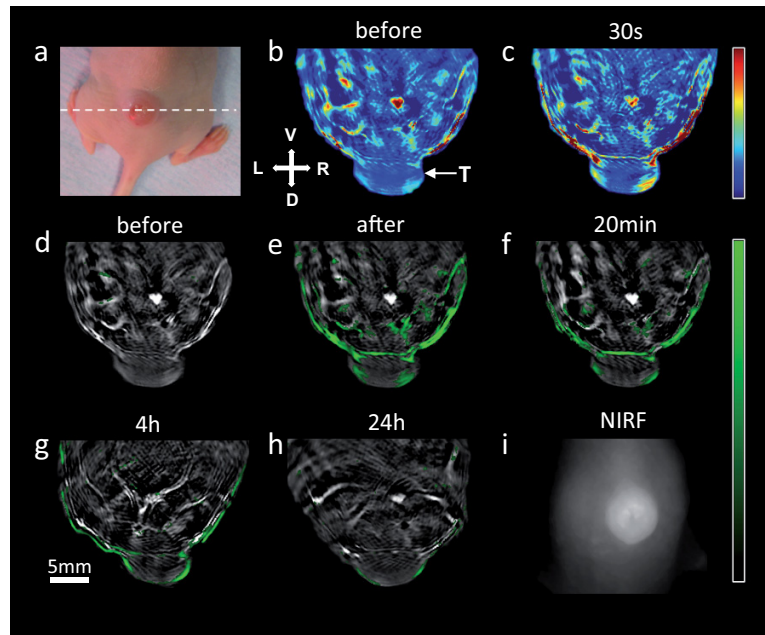


Figure 8.1: Dynamic imaging of ICG perfusion in a tumor. a: Photograph of subcutaneous tumor on the back of a nude mouse. The dotted line indicates the imaged slice shown. b: Single optoacoustic frame recorded at 790nm before ICG injection. c: The same image taken 30s after the start of ICG injection. d-h: MSOT images from subsequent time points where the specific ICG signal is overlaid in green on single wavelength images for anatomical reference. i: NIRF planar reflectance image of the tumor at approximately 24 hours after ICG injection.

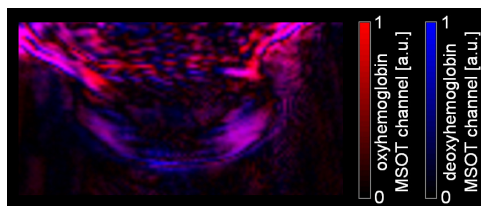


Figure 8.2: Hemoglobin distributions in tumor.

By imaging multispectrally we gain an extra dimension in the data, which allows us to separate the ICG signal from the background, as is shown in the MSOT images in figure 8.1d-h. Here, the signal originating from ICG is overlaid in green on single wavelength images that show the background anatomy. A clear pattern emerges: before injection there is no signal from ICG (figure 8.1d); directly afterwards the unmixed distribution (figure 8.1e) corresponds to the areas where an increase in contrast was observed in the single wavelength sequence, serving as additional validation. The remaining time points show a rapid decrease in signal, as expected from the fact that ICG displays a circulation half-life of a few minutes in mice. The 24 hour image (figure 8.1h) shows only trace amounts of dye remaining in the tumor, probably having leaked out of the malformed vasculature. This is also apparent in the corresponding NIRF image (figure 8.1i).

In addition to unmixing for ICG, the intrinsic hemoglobin contrast can also give insight into the tumor vasculature, and possibly explain the resolved ICG distributions. Figure 8.2 shows an MSOT images of the oxy- and deoxyhemoglobin distribution, extracted from the same data set, in this case prior to injection of ICG. Areas of viable vasculature, indicated by the presence of oxyhemoglobin, correspond with those tumor regions that showed ICG perfusion, an intuitive result.

8.2.4 Discussion

From the results we are able to discern the primary advantage of MSOT over single wavelength optoacoustic imaging for tumor characterisation: it is possible to resolve specific absorbers at single time points without the need for temporally separated reference measurements. This is a key requirement for longitudinal studies of tumor parameters because it is highly challenging to position the animal, primarily consisting of soft tissue, in a way that comparisons of overall absorption can be made over long time periods. In addition to the images of ICG distribution, hemoglobin concentration in both oxygenation states can be mapped in tumors, giving insight into the functional parameters of the tumor vasculature, which can be linked

to intratumoral exogenous agent distributions. Another conclusion that can be drawn from the results is that the high resolution MSOT images give spatially resolved signal distributions revealing the heterogeneity of the tumor. For example, the MSOT image shown in figure 8.1e shows strong ICG signals in areas of viable tumor vasculature and less signal elsewhere. In contrast, the NIRF image (figure 8.1i), which represents a widely used method in biological research for imaging optical agent distribution, gives a surface weighted 2D impression of dye distribution, hiding the underlying tumor heterogeneity.

8.3 MSOT imaging of targeted agent distribution in tumors

8.3.1 Purpose

A wide variety of targeted fluorescent imaging agents exists and more are continuously being developed. As discussed in section 8.2.4, MSOT could provide more accurate intratumoral agent distribution images than commonly employed NIRF techniques. The aim of this study was to investigate the feasibility of targeted fluorescent agent detection in and around tumors by MSOT. Simultaneously, mice were imaged at a number of time points after tumor cell inoculation to investigate the ability of MSOT to probe intrinsic tissue absorbers to give a more complete picture of the tumor environment.

8.3.2 Method

A commercially available fluorescent agent, IntegriSense750 (PerkinElmer), which is targeted to $\alpha_V\beta_3$ integrins was employed. The experimental protocol was as follows:

1. Adult female nude mice were inoculated subcutaneously on the lower back with 0.8 million 4T1 mouse mammary tumor cells (ATCC CRL-2539) each.
2. MSOT imaging experiments without agent injection were performed at on various days during tumor growth.
3. Once the tumor reached a diameter of approximately 8mm, the terminal imaging experiments were initiated. The mice were kept under isoflurane anesthesia for the duration of the experiments.

4. A catheter was placed in the tail vein prior to positioning in the MSOT imaging system.
5. Guided by real-time optoacoustic images displayed on the system, the mice, in a supine position, were translated to allow transverse slices through the tumor to be recorded.
6. Reference images were recorded at multiple slice positions through the tumor. The imaged wavelengths were 700nm, 730nm, 745nm, 760nm, 800nm, and 900nm. 100 single pulse images were averaged at each wavelength.
7. A series of single pulse images was recorded at 750nm, near the absorption peak of IntegriSense750. During this acquisition, 24nmoles of IntegriSense750 were injected into the tail vein.
8. After injection, multispectral imaging was performed as described for the reference images. This data was recorded repeatedly at the following time points after injection: immediately afterwards, 30 minutes, 1 hour, 2 hours, and 6:45 hours.
9. Images were reconstructed. IntegriSense was resolved using ICA unmixing (section 4.3.2) and oxy- and deoxyhemoglobin was resolved using linear spectral unmixing using their known spectra.
10. Mice were sacrificed after MSOT imaging. Fluorescence cryoslicing (FCSI, see appendix) was performed after freezing at -80°C.

8.3.3 Results

The results are summarised in figure 8.3. The case presented here is of particular interest, because, as can be seen from the MSOT image resolving the agent (figure 8.3a) and the validating cryosection (figure 8.3b), the agent is distributed on the periphery of the tumor and fails to penetrate further in significant amounts. Why? We can get more information on the tumor by looking at the hemoglobin MSOT images (figure 8.3c). On day 13, from the same measurement data as the agent distribution was obtained, we observe that oxyhemoglobin signals are only detected on the periphery of the tumor, indicating a lack of viable vasculature to bring the agent to the tumor core. Additionally, an area of concentrated deoxyhemoglobin is detected within the tumor core. We can observe this hypoxic core already in MSOT images from day 6.

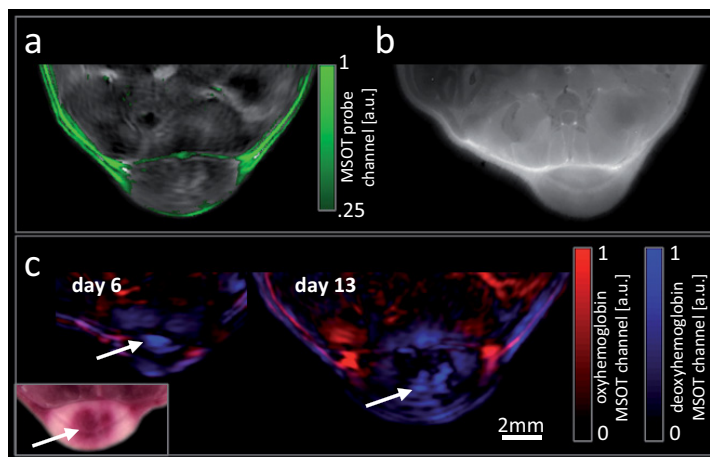


Figure 8.3: MSOT imaging of a targeted optical agent in a tumor. a: MSOT image showing the distribution of an $\alpha_V\beta_3$ targeting fluorescent agent. b: Corresponding fluorescence cryosection image. c: MSOT mapping of oxy- and deoxyhemoglobin in the same tumor on day 6 and day 13 after tumor cell injection. Inset: Colour image of corresponding cryosection. Arrows indicate areas of high deoxyhemoglobin concentration.

8.3.4 Discussion

The results show a number of important findings:

- MSOT is able to detect targeted fluorescent agents, in this case IntegriSense750.
- The resolution and depth penetration of MSOT gives images showing the distribution of detected agents throughout whole tumors.
- The ability to simultaneously image intrinsic absorbers like oxy- and deoxyhemoglobin provides additional functional insights into the tumors and resulting agent distributions.

Again, as seen in section 8.2, the tumor is not homogeneous: the vasculature and the resulting agent distribution is shown by MSOT imaging to show strong intratumoral variations, a result that intravital microscopy would likely miss because of the microscopic fields-of-view analysed, and macroscopic NIRF imaging would equally be blind to due to insufficient spatial resolution.

8.4 Imaging of long-circulating gold nanorods in tumors

8.4.1 Purpose

The aim of this study was to establish whether MSOT could image the accumulation in tumors of long-circulating gold nanorods (AuNR). AuNR display a high, tunable absorption in the near-infrared region. Their accumulation in tumors has been a subject of research because their intense photothermal properties can be used for tumor therapeutic purposes [84] and allow light-mediated drug release [109]. Because of their strong optical absorption peaks, they make suitable MSOT contrast agents, as shown in section 5.4. The dimensions of AuNR are generally well-suited to the so-called enhanced permeability and retention (EPR) effect: the defective vascular architecture in tumors as well as impaired drainage causes particles of this size range to accumulate in tumors. This is referred to as passive tumor targeting.

8.4.2 Method

Commercial AuNR were employed (Ntracker 30-PM-780, Nanopartz), as in section 5.4. The nanorod dimensions are 10nm-by-38nm; this aspect ratio results in an absorption peak at approximately 780nm. The nanorods are coated in a proprietary layer of hydrophilic methyl-polymers that give them extended circulation times *in vivo*, and therefore a longer time period over which to accumulate in tumors by the EPR effect. For the initial experiments, the protocol was as follows:

1. Tumor preparation and handling of mice was as described in section 8.2.2.
2. Reference images were recorded at multiple slice positions through the tumor. The imaged wavelengths were 750nm, 775nm, 800nm, 825nm, 850nm and 900nm. 100 single pulse images were averaged at each wavelength.
3. 16 μ g/g of AuNR was injected into the tail vein during which images at 800nm were recorded.
4. Multispectral imaging was repeated at multiple time points after injection until 24 hours.
5. Blood samples were collected by cardiac puncture. The mice were euthanised, frozen and later sectioned in a multispectral cryoslicing

- imaging system (FSCI, see appendix).
6. The blood samples were centrifuged and the plasma supernatant was measured in a spectrometer to identify AuNR remaining in the circulation.
 7. H&E stains of cryosections from the tumor region were prepared for validation.
 8. Additional cryosections from the tumor region were analysed using darkfield microscopy to identify AuNR by means of their strong scattering.
 9. Images were reconstructed and the AuNR distribution was resolved using linear spectral unmixing.

Further studies were performed on two additional tumor cell lines: A2780 human ovarian cancer (Sigma-Aldrich, 0.8 million cells), and HT29 human colon adenocarcinoma (ATCC-HTB-38, 1.5 million cells). In these studies, the excitation wavelengths were changed (700nm, 730nm, 760nm, 780nm, 800nm, 825nm, 850nm, 900nm) for optimised imaging of hemoglobin oxygenation, and the dosage was reduced to 8 μ g/g.

8.4.3 Results

The results confirm accumulation of AuNR in tumors imagable by MSOT (figure 8.4). The greatest accumulation of AuNR was measured 24 hours post injection, where the MSOT image shows particularly high concentrations of AuNR at the tumor interface (figure 8.4b). Additionally, some accumulation is seen in regions in the core of the tumor. A photograph of a corresponding cryosection (figure 8.4c) shows elevated levels of accumulated blood in the tumor interface and in the core of the tumor where AuNR was also detected. The H&E stains indicate acellular regions in the same places (figure 8.4d: tumor interface and 8.4e: in the tumor core). Darkfield microscopy revealed high levels of AuNR concentration (AuNR appear as bright yellow/orange spots in figure 8.4f&g) in the tumor interface (figure 8.4f) as well as more sparsely distributed AuNR in the tumor core (figure 8.4g), confirming the MSOT findings.

In subsequent experiments we quantified accumulation parameters of AuNR in examples of tumors displaying differing vascular characteristics. By mapping areas of high AuNR concentration onto the images (figure 8.5a-e) we observe a changing pattern: at the initial time points after injection, the AuNR are mainly found in the circulation (figure 8.5b&c), whereas the images taken after 5 and 24 hours show accumulation outside of blood vessels,

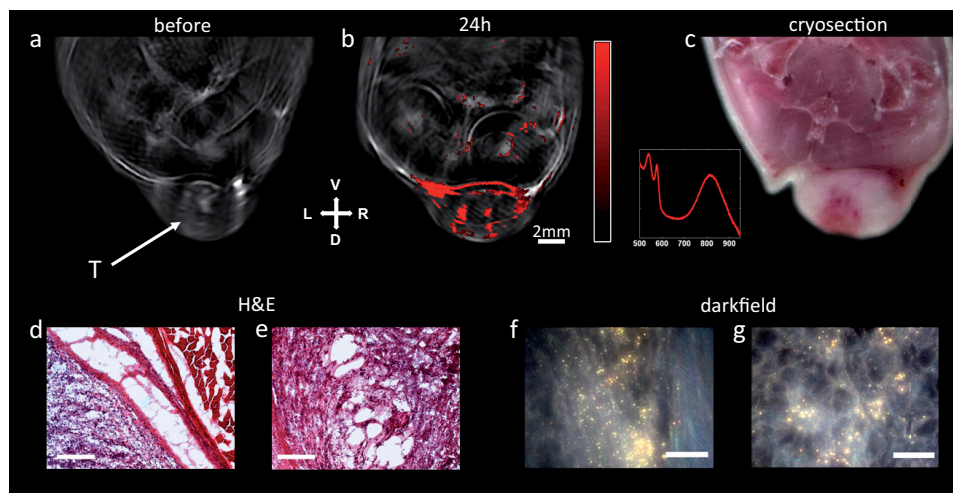


Figure 8.4: Initial imaging of long-circulating gold nanorods in tumors. a&b: MSOT images from before injection of AuNR (a) and after 24 hours (b) where the specific signal from AuNR is overlaid in red on single wavelength images for anatomical reference. T - tumor. Inset: extinction spectrum of plasma supernatant (24h) showing absorption peak of AuNR still present. c: colour photograph of a corresponding cryosection. d&e: H&E stained slides from the tumor showing the tumor interface (d) and acellular areas inside the tumor (e). Scalebars show 500 μ m. f&g: darkfield microscopy images of slides from the tumor interface (f) and from the inside of the tumor (g). Scalebars show 20 μ m.

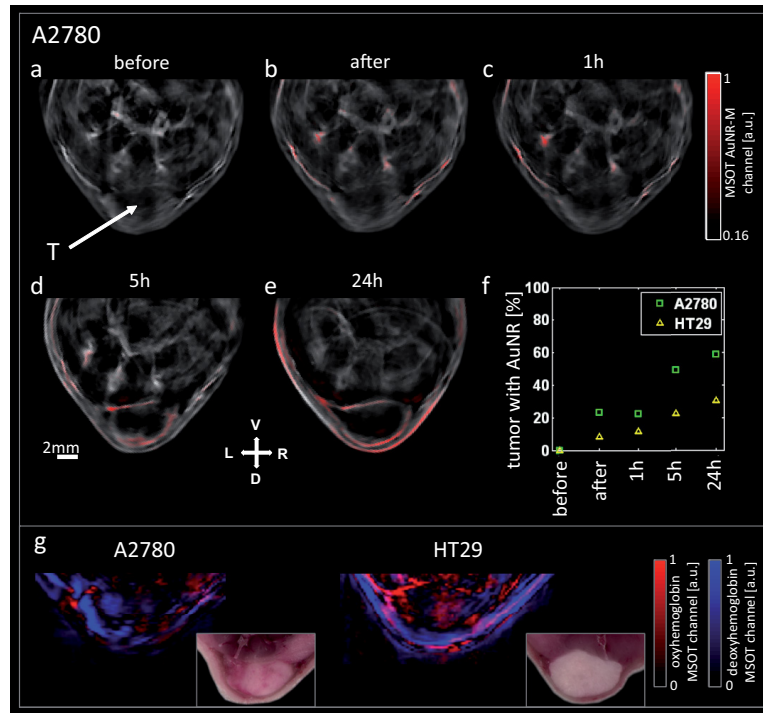


Figure 8.5: MSOT imaging of accumulation of AuNR in tumors. a-e: Images from a A2780 tumor mouse with multispectrally resolved AuNR signal overlaid in red where transparency increases with decreases in signal strength; time points: a: before injection, b: directly after injection, c: 1 hour after injection, d: 5 hours after injection, e: 24 hours after injection. f: A plot showing the percentage of tumor tissue with detectable AuNR signal for 2 tumors of different cell lines. g: 2-colour oxy/deoxyhemoglobin images of the tumors. Insets: Colour images of corresponding cryosections.

by the EPR effect (figure 8.5d&e). We characterised the percentage of tumor tissue displaying increased AuNR signal in two single tumors of the cell lines HT29 and A2780. The A2780 tumor showed accumulation in a higher percentage of the measured tumor tissue (figure 8.5f). Again, from the same MSOT data, we produced quantitative maps of contributions from oxy- and deoxyhemoglobin in the tumors (figure 8.5g). The resulting images indicate functionally differing tumor vasculatures, which suggest a relationship between the accumulation metrics and vascular architecture. *Ex vivo* images of cryosections taken after the experiments agree with these *in vivo* results: the A2780 tumor has visible blood accumulations where the *in vivo* image showed deoxyhemoglobin signal (figure 8.5g).

8.4.4 Discussion

The initial experimental results show that MSOT can be used to detect the accumulation of AuNR in tumors. As in the case of ICG (see section 8.2) the distribution of the AuNR detected by MSOT and confirmed by darkfield microscopy, is highly heterogeneous. The correlation between areas of high AuNR concentration and areas shown in the the cryosection to have high concentrations of blood could indicate that the AuNR has been deposited by malformed vasculature, that is, by the EPR effect (passive tumor targeting). This valuable information is only available to MSOT: AuNR cannot be detected in deep tissues at high resolution by other optical methods. Such imaging may be used for studies of passive targeting efficiency of nanoparticles of different sizes and properties, or to track the therapeutic effects of photothermal and photodynamic therapy.

8.5 Gold-enhanced liposomal nanocarriers

8.5.1 Purpose

The promise of therapeutic applications of small interfering RNA (siRNA) has given rise to a large interest in their use for prevention and treatment of a variety of diseases, including cancer. Routine clinical use of siRNA therapeutics will depend in part on the development of appropriate delivery vehicles [110]. Naked siRNAs are degraded by enzymes *in vivo*, are not suited for crossing cell membranes, and may not have suitable pharmacokinetic profiles for successfully reaching their targets after administration. It is therefore the task of the delivery vehicle to protect the siRNA from the biological environment and safely carry it to its specific target. Liposomes are considered among the most promising delivery vehicles for siRNA, in

particular due to their history as vehicles for chemotherapeutic agents [111], their fusogenic capacity [112] and the wide range of chemical modifications possible to tailor both their targeting and release profiles.

In vivo imaging can become an essential method for optimising siRNA delivery vehicles by characterising their pharmacokinetic and biodistribution profiles. Requirements of a suitable imaging modality include the ability to noninvasively resolve the distribution of the nanocarriers at sufficient spatial resolution throughout relevant animal models of disease and enable longitudinal studies at adequate temporal resolution. MSOT fits these requirements, as shown in the imaging results presented up to this point.

In this study we considered an imaging platform based on the combination of *in vivo* MSOT imaging and *ex vivo* fluorescence cryoslicing imaging (FCSI, see appendix) to investigate the pharmacokinetics and biodistribution of siRNA carrying liposomes and of siRNA.

8.5.2 Method

8.5.2.1 Nanocarrier system

The nanocarrier system is based on a solution of liposomes obtained by extrusion of an aqueous phospholipid preparation. For validation purposes, a fluorescent tag (NIR-797) labels the layers of the vesicle. In order for this nanocarrier to provide optoacoustic contrast, commercially available gold nanorods (NTracker 30-PM-780, Nanopartz Inc.), as described in section 8.4, were loaded onto the liposome outer layer by mixing. After purification by size exclusion, a fluorescent siRNA-Atto655 conjugate was added, yielding a nanocarrier-siRNA complex by electrostatic interaction on the surface of the liposome.

8.5.2.2 Phantom imaging

To confirm the ability of MSOT to detect the gold nanorod-enhanced liposomal nanocarriers, a cylindrical phantom of 2cm diameter was prepared by molding 1.3% by weight of agar powder (Sigma-Aldrich) mixed with 6% of Intralipid 20% emulsion (Sigma-Aldrich) to obtain a background with an reduced scattering coefficient of $\mu'_s \approx 10\text{cm}^{-1}$. A cylindrical inclusion with a diameter of approximately 3mm in the centre of the cylinder contained a solution of the liposomes. Multispectral data sets of the phantom were recorded in the real-time MSOT system (section 3.5.2) between 700nm and 900nm with 10nm steps each using 100 signal averages.

8.5.2.3 Tumor imaging

We employed 4T1 mouse breast cancer and HT29 human colon adenocarcinoma cancer cells, in each case inoculated subcutaneously in adult female CD1 nude mice (Charles River Laboratories). In the case of the 4T1 tumors, 0.8 million cells were used per mouse; for the HT29 tumors, 1.5 million cells were used. Upon reaching a tumor diameter of approximately 7mm, mice were anesthetised with Isoflurane and intra-tumorally injected with the liposomal nanocarrier systems. The injected volume of the complex was 25 μ l.

We performed *in vivo* MSOT imaging by recording optoacoustic data at multiple excitation wavelengths (700nm, 730nm, 760nm, 770nm, 800nm, 860nm and 900nm) using 100 averaged signals per wavelength (real-time MSOT system, section 3.5.2). The wavelengths were selected to be able to resolve the gold nanorods labelling the liposomes from the background absorption of the tissue. Imaging time points were directly before injection (as a reference), immediately after injection, and after 30 minutes, 1 hour and 6 hours. Multiple slices were acquired at 1mm intervals to cover the entire tumor region. After delay-and-sum image reconstruction, nanocarrier distributions were resolved using independent component analysis (ICA, section 4.3.2).

Following *in vivo* MSOT, mice were euthanised and frozen. We performed *ex vivo* imaging using fluorescence cryoslicing imaging (FCSI, see Appendix). The frozen mice were sliced at a 500 μ m pitch, and colour and fluorescence images were recorded from each slice. Fluorescence images were captured at 817nm (peak emission) to resolve the liposomes based on their fluorescent labels (NIR-797) as well as 677nm to resolve the siRNA by means of their fluorescent tags (Atto655). To confirm the presence and distribution of gold nanorods inside the tumors, tissue samples were characterised using darkfield scattering microscopy.

8.5.3 Results

8.5.3.1 Phantom imaging

It was possible to detect the gold nanorod-enhanced liposomes in the phantom, as can be seen in figure 8.6 where the optoacoustic image at 780nm displays a cross-section through the inclusion with high contrast over the background. In figure 8.7, the mean value of the optoacoustic image intensity from the gold nanorod-enhanced liposome inclusion is plotted against wavelength. The results show good correspondence between the spectrum of the gold nanorod-enhanced liposomes measured by MSOT and the spectrometer.

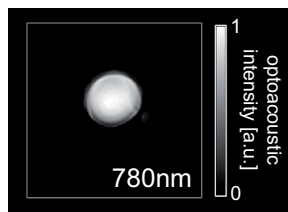


Figure 8.6: Optoacoustic image of phantom containing gold nanorod-enhanced liposomes at 780nm excitation. The inclusion can be observed to produce a bright signal.

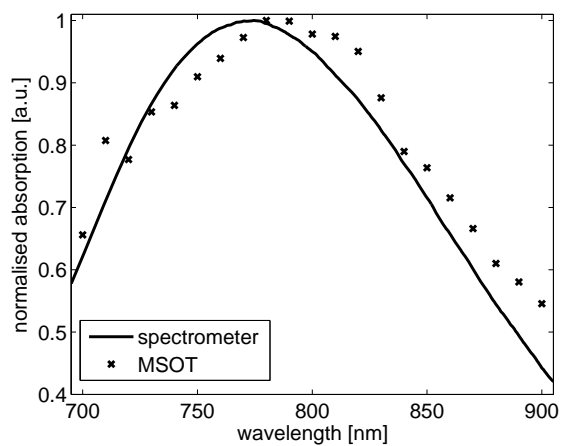


Figure 8.7: Absorption spectrum of gold nanorod-enhanced liposomes, as measured in a spectrometer and by MSOT.

8.5.3.2 Tumor imaging

The *in vivo* MSOT imaging results using the nanocarrier-siRNA complex are summarised in figure 8.8. Figure 8.8a&b are MSOT images (slices through the middle of the tumor) of a mouse with a 4T1 tumor at 1 hour and 6 hours after injection respectively; the signal fitted to the spectrum of the gold nanorods is overlaid in green on anatomical (900nm) images. Figure 8.8f&g show the equivalent images for a mouse with an HT29 tumor. It can be concluded by the similarity of the green signal in the images at the different time points that the liposomes exhibited minimal diffusion through the tumor volume over 6 hours, independent of the cancer cell line used. This information is not available to conventional optical macroscopy methods because of insufficient spatial resolution due to photon diffusion. Figure 8.8c&d show fluorescence cryosections corresponding to the MSOT slices. Evident on the images is that the distribution of the liposomes as determined by epi-fluorescence corresponds to the signals detected in the *in vivo* MSOT imaging experiments. Figure 8.8d shows the distribution of the siRNA, determined by signal from the Atto655 tag (emission peak 677nm). The images reveal an siRNA pattern that is markedly different from the biodistribution resolved for the liposomes, indicating a release of siRNA. Correspondingly, figure 8.8f-j show the images obtained from an HT29 tumor-bearing mouse. Again, *in vivo* MSOT findings are in agreement with the epi-fluorescence image of the liposomes (figure 8.8h). The siRNA distribution in this case (figure 8.8i), shows more diffusion away from the accumulation site of the liposomes than in the case of the 4T1 tumor, possibly caused by the increased viable vascularity of the HT29 tumor, as in both cases the siRNA signal seemed to be colocalised with blood vessels. Finally, figure 8.8e&j show darkfield scattering microscopy images of tissue slices from the 4T1 and HT29 tumors respectively; gold nanorods can be seen as orange spots in these images due to their light scattering properties.

8.5.4 Discussion

The experimental results demonstrate *in vivo* MSOT imaging that resolves gold nanorod-enhanced liposomal nanocarriers for delivery of siRNA within tumors. The successful MSOT detection of this delivery system was validated by epi-fluorescence imaging in two different cancer cell lines.

Research on therapeutic applications of synthetic siRNAs has already demonstrated the ability to knock down genetic targets in several diseases *in vivo*, including cancer. For successful clinical translation, it is important to efficiently deliver the therapeutic molecule to the intended target by achieving appropriate pharmacokinetic and biodistribution profiles using appropriate

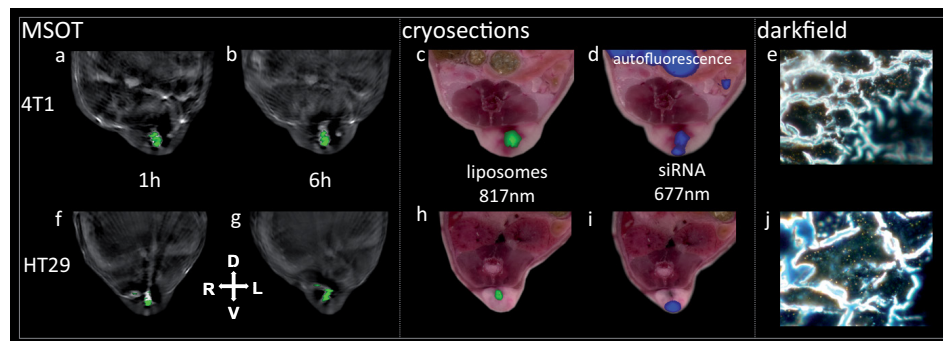


Figure 8.8: Tumor imaging results. a and b: MSOT images showing multispectrally resolved gold nanorod-enhanced liposomes within a 4T1 tumor after 1 hour and 6 hours respectively. c and d: Epi-fluorescence images of a corresponding cryosection taken after 6 hours, where c shows fluorescence signal from the liposomes and d shows signal from the siRNA. e: Darkfield microscopy showing gold nanorods in the tumor tissue as orange points. f-j: Same as a-e for an HT29 tumor.

delivery vehicles. *In vivo* imaging can be an essential tool in the development and optimisation of such systems.

Future efforts in this field of application will use delivery systems optimised for intravenous administration and fine tune the release kinetics and localization via modification of the liposome surface functions. Additionally, we hope to tag the siRNA in such a way that it can be resolved by MSOT *in vivo* alongside the carriers to give a more complete, multispectral picture of the delivery and biodistribution of these exciting therapeutic strategies.

8.6 Concluding remarks

The performance indicated by the MSOT imaging results in this chapter shows a new ability in optical imaging of cancer. Intravital microscopy offers high resolution information on tumor parameters, but reveals only a superficial view into the tumor. Macroscopic NIRF imaging generally reveals average, superficially-weighted information on fluorochrome distribution from the tumor surface, rather than highly resolved underlying activity. On the other hand, the presented MSOT results reveal the highly heterogeneous distribution of optical agents and tissue absorbers. The images display varying patterns, a typical example being peripheral distribution around tumors and inability for agents to penetrate uniformly through the tumor bulk. Corresponding images of hemoglobin in its separate oxygenation states indicate a lack of viable vasculature in the tumor core in such

cases. This detailed information on intra-tumoral parameters is available to MSOT because it is a high resolution method that further displays an appropriate sensitivity for detecting these various absorbers.

The identification of spectral signatures of specific absorbers, allowing imaging of the biodistribution of a molecule of interest without the need for baseline measurements, is particularly useful in studies where measurements over several hours or days are necessary. In this way, we were able to characterise the accumulation of nanoparticles over time. Importantly, the current MSOT implementation allows fast wavelength scans, enabling the identification of multiple spectral signatures in the same imaging section. This allowed the additional spatial mapping of oxy- and deoxyhemoglobin in tumors, to provide functional insights into their vasculature.

A superficial tumor model was employed here for simplicity; however internal mouse structures are also visible in the images. It would therefore be possible to image orthotopic tumors, an aspect of future investigation. The sensitivity in detecting tumor biomarkers will however naturally drop with depth, since light attenuates by approximately 1-2 orders of magnitude per centimetre of propagation. An additional limitation in the current system is that real-time imaging can be achieved only on a single slice at one time. Therefore, while the entire tumor can be scanned sequentially by mechanical scanning, real-time imaging can be performed only on two-dimensional slices. Future developments foresee a larger detector array that could capture three-dimensional data from entire tumors without the need for mechanical scanning.

Overall, MSOT can play the role of a natural extension of intravital microscopy: by sacrificing optical diffraction limited resolution one can achieve significantly larger penetration depths at ultrasound resolution. A strength of using macroscopic MSOT systems alongside optical microscopy is that for many agents, the same contrast can be visualised macroscopically and microscopically. This performance could also find applications in clinical settings, in particular in relation to hand-held or endoscopic systems, expanding the capabilities of clinical cancer imaging.

Chapter 9

Conclusions and future directions

9.1 Conclusions

Established biomedical imaging is dominated by modalities informing on structure and morphology, like ultrasound, MRI, and X-ray, with limited insight into the biology that is the underlying cause of disease. Nuclear imaging provides valuable biological parameters, but at a low spatial resolution, and at the cost of ionising radiation and decaying tracers. Multi-spectral optoacoustic tomography (MSOT), based on the ultrasound detection of optical absorption via the optoacoustic effect, provides images that probe the underlying biological processes involved in disease. The technique combines rich optical contrast, provided by intrinsic tissue absorbers like hemoglobin and a multitude of optical imaging agents, with ultrasound resolution in deep tissues, breaking through the barrier that the high scattering of light raises after the first millimetre. By employing multi-wavelength illumination, MSOT distinguishes absorbers based on their spectral signatures, enabling multichannel images of specific chromophores of interest, including the different hemoglobin oxygenation states and exogenous optical contrast agents, enabling *in vivo* imaging of a diverse range of disease-related biomarkers.

This thesis is entitled *Multispectral optoacoustic tomography for imaging of disease biomarkers*, and, if you have read to this point, you will have seen diverse studies showing that MSOT is indeed capable of visualising a variety of biomarkers in the form of tissue-intrinsic and exogenous absorbers of light, and you will also understand the methods employed for successful MSOT imaging and the limitations involved with the technique. Returning to the

stated objectives of this research (section 1.6), a number of questions have now been answered. Concerning instrumentation (chapters 3):

- It is now an established fact that multi-element arrays detecting optoacoustic signals from a 2D plane with the help of focussing in the elevational dimension enable meaningful images to be acquired from each single laser pulse, making real-time imaging of slices through small animals possible.

Concerning the methods applied for image reconstruction (chapter 4):

- Model-based approaches to image reconstruction can, in theory, produce quantitative images of the initial optoacoustic pressure distribution, as long as all measurement system characteristics with significant influence are modelled. Delay-and-sum approaches are fast and ideally suited for invaluable real-time displays during experiments.
- A number of approaches for spectrally resolving the separate distributions of absorbers exist. Linear spectral unmixing is suited for scenarios where the major source spectra are known, such as unmixing of oxygenation states of hemoglobin. Blind unmixing approaches better handle situations where unknown source spectra or unknown changes in source spectra are present.
- Algorithms that constrain least-squares to positive solutions should be applied in imaging experiments to prevent physically unrealistic combinations of source spectra in linear spectral unmixing results.
- In simulation models, light attenuation with penetration depth has been shown to have an effect not only on overall optoacoustic signal levels, but also, because of wavelength-dependent attenuation, on the robustness of spectrally unmixed MSOT results. However, in many scenarios relative quantification is possible, for example in imaging absorbers of different concentrations at similar depths. Additionally, the effect of wavelength-dependent light attenuation in corrupting measured optoacoustic spectra only takes hold after a significant depth. Correction approaches for light attenuation are a topic of active research.
- Ratio normalisation techniques, where unmixed signals from specific absorbers are divided by overall signal levels, can be used to extract relative concentration metrics that are corrected for the overall attenuation of light.

Concerning the sources of MSOT image contrast (chapter 5):

- Hemoglobin is the most natural source of MSOT contrast because it dominates optical absorption in tissue, even in the near infrared. Blood vessels therefore appear in the images. Distinguishing the oxygenation states of hemoglobin based on near infrared excitation is also possible, enabling imaging of the separate distributions of oxy- and deoxyhemoglobin, and also functional measures like hemoglobin oxygen saturation. A multitude of biomarkers based on this capability alone can thus be probed by MSOT.
- Other tissue-intrinsic absorbers of light that have the potential to yield meaningful MSOT contrast are melanin, water and lipids.
- A wealth of different exogenous contrast agents for optoacoustic imaging have been reported in the literature. They can largely be categorised as organic dyes, plasmonic nanoparticles or varieties of carbon nanotubes. For purposes of spectral separation from the background, the defining mechanism of MSOT, contrast agents should ideally have absorption spectra which display a rapid variation with wavelength or narrow characteristic peaks. Some of the agents reported in the literature for single-wavelength optoacoustic imaging, such as carbon nanotubes, have relatively flat absorption spectra which are not ideal for MSOT.
- The feasibility of MSOT imaging of ICG and gold nanorods was demonstrated. By imaging circulating gold nanorods *in vivo*, the primary advantage of MSOT over single-wavelength imaging became clear: MSOT can separate the injected agent from the tissue background and therefore has no need for reference images where everything except the agent must be kept constant.
- By exploiting changes on activation in the absorption spectrum of an enzyme-activatable fluorescent agent, it was shown that imaging protease activity by MSOT is feasible.

Overall, the wide range of biologically relevant sources of contrast available to MSOT imaging confirm the technique's potential in imaging biomarkers of disease.

We can draw the following conclusions from work on characterising the dynamics of exogenous optical agents, which could find application in the drug development process for assessing both the uptake of drugs in various organs and also the function of crucial organs such as the kidneys and liver after drug exposure (chapter 6):

- Because of the high-rate imaging enabled by parallel multi-element ultrasound detection, it is possible to extract metrics on agent concen-

tration changes at the laser pulse repetition rate. To obtain spectrally-resolved specific agent metrics the time needed to vary the excitation wavelength must also be taken into account. Measurements resolving ICG in the circulation using 5 wavelengths with 10 pulses per wavelength were demonstrated; the period between each multispectral data point was then approximately 17s. Improvements in the rate at which the excitation wavelength can be varied are expected in the near future, which will result in the acceleration of an already fast method for characterising optical agent uptake in multiple organs.

- Ratio normalisation techniques are well-suited to characterise the dynamics of exogenous agent uptakes in organs because they give a metric of relative concentration with respect to the total absorption of each pixel, resulting in measures unaffected by overall fluence variations in space and time.

In the field of small animal cardiovascular imaging, several questions have been answered in the course of this research (chapter 7):

- Visualisation of the carotid arteries in the neck and the aortic arch in the upper thorax by MSOT succeeded, pointing to the possibility of studies of atherosclerosis, since these are locations at which plaque development occurs. MSOT is the only known optical imaging technique capable of resolutions sufficient for imaging carotid arteries in mice (order of hundreds of microns), several millimetres under the skin surface.
- Despite the challenges of optoacoustic imaging in the thorax, the first MSOT images of a beating heart show not only that multispectral imaging can distinguish the myocardium from surrounding tissue, but also that frames resulting from single laser pulses yield meaningful images of the heart from which different stages in the cardiac cycle can be identified.
- Automatic clustering according to the stage in the cardiac cycle to which each individual frame belongs can be successfully applied to images of the heart across all wavelengths in such a way that the unmixed MSOT results, for each cluster, display reduced motion blurring. In other words, post measurement motion correction is possible without any gating or triggering schemes.
- Finally, it is possible, with the help of advanced methods such as motion clustering and blind spectral unmixing, to resolve an inflammation-targeted optical agent *in vivo* in a mouse model of myocardial infarction. Because of the anatomical detail available in the MSOT images,

it was possible to distinguish between signal sources in the myocardium and other adjacent regions of peripheral agent accumulation. The promise of such fast, high-resolution imaging of molecular biomarkers *in vivo* could have a significant impact in small animal studies and beyond.

And finally, applying to cancer imaging (chapter 8):

- Subcutaneous tumors, ubiquitous in cancer research, can be successfully imaged in cross-sections by the methods employed here. Optically absorbing organic dyes and nanoparticles can be imaged dynamically as they enter tumors, and over long periods of time, where the spectral unmixing capabilities of MSOT produce more robust comparisons in the face of changing background tissue than single-wavelength imaging can achieve.
- Compared to planar near-infrared fluorescence imaging of agent uptake in tumors (a method in common use in preclinical research today) where photon diffusion causes blurred images that give little information on the subsurface fluorescence distribution, MSOT gives volumetrically robust high resolution results that show, in many cases, highly heterogeneous agent distributions. Intravital microscopy, on the other hand, provides highly resolved information on comparatively small fields-of-view close to the surface, unable to capture whole-tumor characteristics.
- By exploiting the MSOT contrast from hemoglobin, tumor vasculature can be characterised according to distributions of each oxygenation state, providing measures of vascular viability and hypoxia. These parameters, in turn, can provide further information about the possible reasons for heterogeneous exogenous agent distributions in individual tumors.
- The MSOT imaging results of long-circulating gold nanorods accumulating in tumors by the enhanced permeability and retention effect, demonstrate a method highly suited for the study of nanoparticle-based passive-targeting therapeutics.
- Additionally, initial results show that liposomal nanocarriers enhanced with MSOT contrast agents (gold nanorods in this case) can be imaged inside tissue. Studies of the pharmacokinetics of such delivery systems are crucial to their development, which, in turn, are considered of critical importance to emerging therapeutic strategies, such as the siRNA of the experimental studies.

Overall, the high-rate, simultaneous characterisation of optical agent uptake and vascular characteristics through multiple millimetres of tumor tissue and at resolutions sufficient to visualise the heterogeneous nature of tumor biology, is unprecedented.

Naturally, there are limitations associated with MSOT in the context of biomarker imaging, as well as scope for improvement:

- As with any optical imaging technique, the penetration depth is limited by the high absorption and scattering of light in tissue. The results shown display features through entire mouse cross-sections (transverse slices). Results showing deeper penetration, of several centimetres, have been reported in the literature. However, depths measured in tens of centimetres seem unlikely. This limits the applications of non-invasive MSOT to the many scenarios where the imaging targets are within single centimetre ranges from the skin surface. This barrier can also be overcome by endoscopy and intravascular imaging.
- Since optoacoustic signals are in the form of broadband ultrasound waves, regions of the anatomy where ultrasound is highly attenuated are unlikely to yield meaningful MSOT images. As shown with regard to imaging of the thorax, the lungs are not suitable MSOT imaging targets. In mouse imaging, bones are so small that they hardly play a role, as was demonstrated with the rib cage; however, clinical applications involving ultrasound propagation through thick bone layers will require advanced correction algorithms, which form a current research area (see Dean et al., for example [113]).
- As discussed in chapter 4, reconstructing absolute concentrations of absorbers from multispectral optoacoustic data is hindered in deep tissue by the effects of wavelength-dependent light attenuation. Correction methods for light attenuation suited to overcome this obstacle are a topic of ongoing research (see Rosenthal et al., for an example of a promising approach [59]). However, relative quantification is possible and also highly valuable.
- The sensitivity of MSOT detection is a highly complex question which has not been directly answered in this research. As far as detection of organic fluorescent dyes is concerned, experience tells us that regular fluorescence imaging is significantly more sensitive than MSOT. While initial efforts to characterise the sensitivity of MSOT have been made (see Razansky et al. [114]), *in vivo* characterisation is needed. Additionally, sensitivity is instrumentation-specific. It should be noted that statements concerning MSOT sensitivity in units of amount of agent or agent concentration are highly oversimplified: any realistic

measure would need to be given in absorption per unit of light fluence reaching the agent.

- MSOT resolution is a function of the ultrasound detection employed, depending on the cut-off frequency of detection and the detection geometry, as discussed in section 3.3.5. The spatial resolutions shown in this work were in the region of 100-200 μm (in-plane), limited by the specific instrumentation, which was developed for imaging cross-sections through mice (approximate diameter of 2cm). For smaller fields of view, with reduced required penetration depths such as the heart, or subcutaneous tumors, smaller, higher frequency detector elements could have been used to produce higher resolution images. Imaging systems dedicated to producing images of such dimensions, although narrower in general imaging scope, could allow the visualisation of finer details than was possible in this work.
- As discussed quite extensively in chapter 3, the MSOT systems described in this work produced 2D slice images by means of mechanical ultrasound focusing. This is a trade-off, which enables real-time imaging with far less detector elements than would be necessary for full 3D imaging. However, it comes at a price with respect to quantification: although the slice elevation can be mechanically scanned to image through multiple positions, a function which was used throughout the experimental work, the thickness of slices is a function of signal frequency and spatial location, making accurate quantification of signal sources (for example, the amount of an agent) over multiple slices highly challenging. Full 3D real-time MSOT imaging would be a significant improvement for small animal imaging in this respect.
- Another current limitation related to signal detection discussed in chapter 3 is the resonant nature of commonly employed piezoelectric transducers, which is ill-suited for detecting inherently broadband optoacoustic signals, and especially limiting when features across a wide range of scales should be simultaneously imaged. Optical detection of ultrasound, a topic of increasing interest in the research community [40, 29], is one approach that can enable broader-band detection.

These limitations pose challenges which future research efforts in the field of MSOT imaging will surely, at least to some extent, overcome. However, the utility of the method is, through this work and work of others, already proven. Increasingly, MSOT is attracting the interest of biologists and medical professionals, with the focus moving from technical development to biomedical applications, including clinical imaging.

9.2 Towards clinical applications

Although small animal imaging is an ideal starting point for an emerging technology and of much value in pharmaceutical and basic research, there is no reason why MSOT should be restricted to this domain. Conceivable clinical applications are numerous. In particular, the natural sensitivity of MSOT to hemoglobin is an exploitable advantage, without the need for clinically approved contrast agents. Initial results from an optoacoustic breast scanner were published by Manohar et al. in 2007, showing that increased hemoglobin signals resulting from tumor angiogenesis can be detected in cancer patients [39]. However, only 1064nm excitation was used. Applying MSOT to spectrally differentiate hemoglobin oxygenation states would add much certainty to the results. Technology has advanced a great deal since then, and the achievable image quality with it. Further studies are a certainty. Other applications at similar scales in urgent need of imaging that informs on biology include peripheral artery disease and carotid atherosclerosis. On the other end of the depth penetration range, much work is being devoted to the development of optoacoustic microscopy for visualisation of microvasculature and melanoma [30, 115]. On the whole, the range of potential clinical applications across scales varying from microscopy to fields of view of several centimetres is vast. There is much work to be done.

Appendix A

Fluorescence cryoslicing imaging (FCSI)

Fluorescence cryoslicing imaging (FCSI), a method for *ex vivo* visualisation of biodistributions of fluorescent agents was developed at the Institute for Biological and Medical Imaging and described by Sarantopoulos et al. in 2010 [116]. Since FCSI results can be found in multiple figures throughout this document, a brief description of the technique is warranted.

The system (figure A.1) consists of a camera (Luca-R, Andor) mounted on a commercial cryotome (CM 1950, Leica Microsystems), such that the required images can be taken while the sample is being sectioned. A white light source is used for illumination; this light is passed through a selection of bandpass filters in a filter wheel to enable suitable excitation for a range of different fluorochromes. Mounted between the camera and objective is a second filter wheel with appropriate filters for the emission wavelengths of the fluorochromes and chromophores of interest. The filter wheels are controlled by software from a PC. Overall, the system is capable of producing colour images, as well as fluorescence in multiple channels and images at the fluorescence excitation wavelengths that can be used for correction [117]. The field of view is typically a cross-section (transverse plane) through a whole mouse or other tissue specimen.

As an example of what kind of images can be produced using this technique, figure A.2, shows a section through a liver that has taken up the fluorescent dye indocyanine green (ICG). This image is also presented as part of the results in chapter 6. The following steps are needed to produce the image: first, with no excitation filter, that is, with white light, images are acquired using red, green and blue bandpass emission filters successively. These are then merged to form the background colour image as seen in the figure. Next,

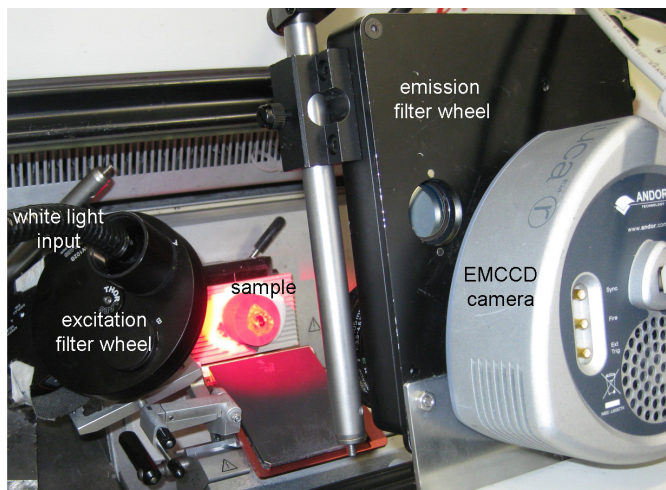


Figure A.1: Labelled photograph of fluorescence cryoslicing imaging system showing the major components.

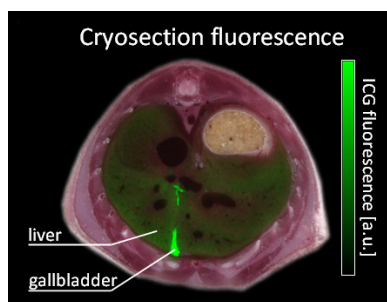


Figure A.2: An example FCSI image.

an excitation filter is selected to give an illumination spectrum suitable for exciting ICG fluorescence, and the suitable filter for the fluorescence emission of ICG is simultaneously selected in the second filter wheel, allowing an image of the fluorescence distribution to be acquired. This image can then be overlaid on the colour image to form a composite: in the example figure the ICG fluorescence is overlaid using a green colour scale with additional transparency.

Because the MSOT implementation presented here produces 2D slice images, it makes sense to present FCSI images in 2D slice form as well, for intuitive comparison. However, since slices can be taken through whole mice at a selectable pitch, it is further possible to visualise FCSI results in 3D and other slice directions than the physical cutting plane, as Sarantopoulos et al. have shown [116].

Bibliography

- [1] “World health organisation: Causes of death 2008 summary tables,” May 2011.
- [2] S. M. Paul, D. S. Mytelka, C. T. Dunwiddie, C. C. Persinger, B. H. Munos, S. R. Lindborg, and A. L. Schacht, “How to improve r&d productivity: the pharmaceutical industry’s grand challenge.,” *Nat Rev Drug Discov*, vol. 9, pp. 203–214, Mar 2010.
- [3] R. Weissleder and V. Ntziachristos, “Shedding light onto live molecular targets.,” *Nat Med*, vol. 9, pp. 123–128, Jan 2003.
- [4] A. Ale, R. B. Schulz, A. Sarantopoulos, and V. Ntziachristos, “Imaging performance of a hybrid x-ray computed tomography-fluorescence molecular tomography system using priors.,” *Med Phys*, vol. 37, pp. 1976–1986, May 2010.
- [5] B. Brooksby, B. W. Pogue, S. Jiang, H. Dehghani, S. Srinivasan, C. Kogel, T. D. Tosteson, J. Weaver, S. P. Poplack, and K. D. Paulsen, “Imaging breast adipose and fibroglandular tissue molecular signatures by using hybrid mri-guided near-infrared spectral tomography.,” *Proc Natl Acad Sci U S A*, vol. 103, pp. 8828–8833, Jun 2006.
- [6] V. Ntziachristos, “Going deeper than microscopy: the optical imaging frontier in biology.,” *Nat Methods*, vol. 7, pp. 603–614, Aug 2010.
- [7] A. Rosencwaig, *Photoacoustics and photoacoustic spectroscopy*. Wiley New York, 1980.
- [8] R. A. Kruger, “Photoacoustic ultrasound.,” *Med Phys*, vol. 21, pp. 127–131, Jan 1994.
- [9] X. Wang, Y. Pang, G. Ku, X. Xie, G. Stoica, and L. V. Wang, “Non-invasive laser-induced photoacoustic tomography for structural and functional in vivo imaging of the brain.,” *Nat Biotechnol*, vol. 21, pp. 803–806, Jul 2003.

- [10] K. H. Song, C. Kim, C. M. Cobley, Y. Xia, and L. V. Wang, "Near-infrared gold nanocages as a new class of tracers for photoacoustic sentinel lymph node mapping on a rat model.," *Nano Lett*, vol. 9, pp. 183–188, Jan 2009.
- [11] R. A. Kruger, W. L. Kiser, D. R. Reinecke, G. A. Kruger, and K. D. Miller, "Thermoacoustic molecular imaging of small animals.," *Mol Imaging*, vol. 2, pp. 113–123, Apr 2003.
- [12] D. Razansky, C. Vinegoni, and V. Ntziachristos, "Multispectral photoacoustic imaging of fluorochromes in small animals.," *Opt Lett*, vol. 32, pp. 2891–2893, Oct 2007.
- [13] M. Li, J. Oh, X. Xie, G. Ku, W. Wang, C. Li, G. Lungu, G. Stolica, and L. Wang, "Simultaneous molecular and hypoxia imaging of brain tumors in vivo using spectroscopic photoacoustic tomography.," *Proceedings of the IEEE*, vol. 96, no. 3, pp. 481–489, 2008.
- [14] A. Taruttis, N. Deliolanis, A. Rosenthal, D. Razansky, and V. Ntziachristos, "Multispectral optoacoustic tomography (msot) characterization in resolving molecular biomarkers.," in *World Congress on Medical Physics and Biomedical Engineering, September 7-12, 2009, Munich, Germany*, pp. 447–449, Springer, 2009.
- [15] R. Weissleder, "Scaling down imaging: molecular mapping of cancer in mice.," *Nat Rev Cancer*, vol. 2, pp. 11–18, Jan 2002.
- [16] D. E. Sosnovik, M. Nahrendorf, N. Deliolanis, M. Novikov, E. Aikawa, L. Josephson, A. Rosenzweig, R. Weissleder, and V. Ntziachristos, "Fluorescence tomography and magnetic resonance imaging of myocardial macrophage infiltration in infarcted myocardium in vivo.," *Circulation*, vol. 115, pp. 1384–1391, Mar 2007.
- [17] J. o Deguchi, M. Aikawa, C.-H. Tung, E. Aikawa, D.-E. Kim, V. Ntziachristos, R. Weissleder, and P. Libby, "Inflammation in atherosclerosis: visualizing matrix metalloproteinase action in macrophages in vivo.," *Circulation*, vol. 114, pp. 55–62, Jul 2006.
- [18] L. Wang and H. Wu, *Biomedical optics: principles and imaging*. Wiley-Blackwell, 2007.
- [19] M. J. Niedre, G. M. Turner, and V. Ntziachristos, "Time-resolved imaging of optical coefficients through murine chest cavities.," *J Biomed Opt*, vol. 11, no. 6, p. 064017, 2006.
- [20] G. M. Hale and M. R. Querry, "Optical constants of water in the 200-nm to 200-microm wavelength region.," *Appl Opt*, vol. 12, pp. 555–563, Mar 1973.

- [21] S. J. Matcher, M. Cope, and D. T. Delpy, "In vivo measurements of the wavelength dependence of tissue-scattering coefficients between 760 and 900 nm measured with time-resolved spectroscopy.," *Appl Opt*, vol. 36, pp. 386–396, Jan 1997.
- [22] J. R. Mourant, T. Fuselier, J. Boyer, T. M. Johnson, and I. J. Bigio, "Predictions and measurements of scattering and absorption over broad wavelength ranges in tissue phantoms.," *Appl Opt*, vol. 36, pp. 949–957, Feb 1997.
- [23] C. Li and L. V. Wang, "Photoacoustic tomography and sensing in biomedicine.," *Phys Med Biol*, vol. 54, pp. R59–R97, Oct 2009.
- [24] G. Diebold, T. Sun, and M. Khan, "Photoacoustic monopole radiation in one, two, and three dimensions.," *Phys Rev Lett*, vol. 67, pp. 3384–3387, Dec 1991.
- [25] R. Fine and F. Millero, "Compressibility of water as a function of temperature and pressure," *The Journal of Chemical Physics*, vol. 59, p. 5529, 1973.
- [26] R. A. Kruger, P. Liu, Y. R. Fang, and C. R. Appledorn, "Photoacoustic ultrasound (paus)–reconstruction tomography.," *Med Phys*, vol. 22, pp. 1605–1609, Oct 1995.
- [27] T. Szabo, *Diagnostic ultrasound imaging: inside out*. Academic Press, 2004.
- [28] P. Beard, F. Pérennes, and T. Mills, "Transduction mechanisms of the fabry-perot polymer film sensing concept for wideband ultrasound detection," *Ultrasonics, Ferroelectrics and Frequency Control, IEEE Transactions on*, vol. 46, no. 6, pp. 1575–1582, 1999.
- [29] A. Rosenthal, D. Razansky, and V. Ntziachristos, "High-sensitivity compact ultrasonic detector based on a pi-phase-shifted fiber bragg grating.," *Opt Lett*, vol. 36, pp. 1833–1835, May 2011.
- [30] H. F. Zhang, K. Maslov, G. Stoica, and L. V. Wang, "Functional photoacoustic microscopy for high-resolution and noninvasive in vivo imaging.," *Nat Biotechnol*, vol. 24, pp. 848–851, Jul 2006.
- [31] K. Maslov, H. F. Zhang, S. Hu, and L. V. Wang, "Optical-resolution photoacoustic microscopy for in vivo imaging of single capillaries.," *Opt Lett*, vol. 33, pp. 929–931, May 2008.
- [32] R. Ma, A. Taruttis, V. Ntziachristos, and D. Razansky, "Multispectral optoacoustic tomography (msot) scanner for whole-body small animal imaging.," *Opt Express*, vol. 17, pp. 21414–21426, Nov 2009.

- [33] A. Buehler, E. Herzog, D. Razansky, and V. Ntziachristos, “Video rate optoacoustic tomography of mouse kidney perfusion.,” *Opt Lett*, vol. 35, pp. 2475–2477, Jul 2010.
- [34] A. Taruttis, E. Herzog, D. Razansky, and V. Ntziachristos, “Real-time imaging of cardiovascular dynamics and circulating gold nanorods with multispectral optoacoustic tomography.,” *Opt Express*, vol. 18, pp. 19592–19602, Sep 2010.
- [35] H.-P. Brecht, R. Su, M. Fronheiser, S. A. Ermilov, A. Conjusteau, and A. A. Oraevsky, “Whole-body three-dimensional optoacoustic tomography system for small animals.,” *J Biomed Opt*, vol. 14, no. 6, p. 064007, 2009.
- [36] R. A. Kruger, R. B. Lam, D. R. Reinecke, S. P. D. Rio, and R. P. Doyle, “Photoacoustic angiography of the breast.,” *Med Phys*, vol. 37, pp. 6096–6100, Nov 2010.
- [37] M. Xu and L. V. Wang, “Analytic explanation of spatial resolution related to bandwidth and detector aperture size in thermoacoustic or photoacoustic reconstruction.,” *Phys Rev E Stat Nonlin Soft Matter Phys*, vol. 67, p. 056605, May 2003.
- [38] J. Gamelin, A. Maurudis, A. Aguirre, F. Huang, P. Guo, L. V. Wang, and Q. Zhu, “A real-time photoacoustic tomography system for small animals.,” *Opt Express*, vol. 17, pp. 10489–10498, Jun 2009.
- [39] S. Manohar, S. E. Vaartjes, J. C. G. van Hespren, J. M. Klaase, F. M. van den Engh, W. Steenbergen, and T. G. van Leeuwen, “Initial results of in vivo non-invasive cancer imaging in the human breast using near-infrared photoacoustics.,” *Opt Express*, vol. 15, pp. 12277–12285, Sep 2007.
- [40] J. Laufer, E. Zhang, G. Raivich, and P. Beard, “Three-dimensional noninvasive imaging of the vasculature in the mouse brain using a high resolution photoacoustic scanner.,” *Appl Opt*, vol. 48, pp. D299–D306, Apr 2009.
- [41] C. Zhang, K. Maslov, and L. V. Wang, “Subwavelength-resolution label-free photoacoustic microscopy of optical absorption in vivo.,” *Opt Lett*, vol. 35, pp. 3195–3197, Oct 2010.
- [42] S. Hu, B. Rao, K. Maslov, and L. V. Wang, “Label-free photoacoustic ophthalmic angiography.,” *Opt Lett*, vol. 35, pp. 1–3, Jan 2010.
- [43] S. Jiao, M. Jiang, J. Hu, A. Fawzi, Q. Zhou, K. K. Shung, C. A. Puliafito, and H. F. Zhang, “Photoacoustic ophthalmoscopy for in vivo retinal imaging.,” *Opt Express*, vol. 18, pp. 3967–3972, Feb 2010.

- [44] J. Sanz and Z. A. Fayad, "Imaging of atherosclerotic cardiovascular disease.," *Nature*, vol. 451, pp. 953–957, Feb 2008.
- [45] S. Sethuraman, S. R. Aglyamov, J. H. Amirian, R. W. Smalling, and S. Y. Emelianov, "Intravascular photoacoustic imaging using an ivus imaging catheter.," *IEEE Trans Ultrason Ferroelectr Freq Control*, vol. 54, pp. 978–986, May 2007.
- [46] K. Jansen, A. F. W. van der Steen, H. M. M. van Beusekom, J. W. Oosterhuis, and G. van Soest, "Intravascular photoacoustic imaging of human coronary atherosclerosis.," *Opt Lett*, vol. 36, pp. 597–599, Mar 2011.
- [47] J.-M. Yang, K. Maslov, H.-C. Yang, Q. Zhou, K. K. Shung, and L. V. Wang, "Photoacoustic endoscopy.," *Opt Lett*, vol. 34, pp. 1591–1593, May 2009.
- [48] Y. Yuan, S. Yang, and D. Xing, "Preclinical photoacoustic imaging endoscope based on acousto-optic coaxial system using ring transducer array.," *Opt Lett*, vol. 35, pp. 2266–2268, Jul 2010.
- [49] E. I. Galanzha, E. V. Shashkov, T. Kelly, J.-W. Kim, L. Yang, and V. P. Zharov, "In vivo magnetic enrichment and multiplex photoacoustic detection of circulating tumour cells.," *Nat Nanotechnol*, vol. 4, pp. 855–860, Dec 2009.
- [50] E. I. Galanzha, E. V. Shashkov, P. M. Spring, J. Y. Suen, and V. P. Zharov, "In vivo, noninvasive, label-free detection and eradication of circulating metastatic melanoma cells using two-color photoacoustic flow cytometry with a diode laser.," *Cancer Res*, vol. 69, pp. 7926–7934, Oct 2009.
- [51] C. G. Hoelen and F. F. de Mul, "Image reconstruction for photoacoustic scanning of tissue structures.," *Appl Opt*, vol. 39, pp. 5872–5883, Nov 2000.
- [52] M. Xu and L. V. Wang, "Universal back-projection algorithm for photoacoustic computed tomography.," *Phys Rev E Stat Nonlin Soft Matter Phys*, vol. 71, p. 016706, Jan 2005.
- [53] A. Rosenthal, D. Razansky, and V. Ntziachristos, "Fast semi-analytical model-based acoustic inversion for quantitative photoacoustic tomography.," *IEEE Trans Med Imaging*, vol. 29, pp. 1275–1285, Jun 2010.
- [54] C. Paige and M. Saunders, "Lsqr: An algorithm for sparse linear equations and sparse least squares," *ACM Transactions on Mathematical Software (TOMS)*, vol. 8, no. 1, pp. 43–71, 1982.

- [55] A. Buehler, A. Rosenthal, T. Jetzfellner, A. Dima, D. Razansky, and V. Ntziachristos, "Model-based optoacoustic inversions with incomplete projection data.," *Med Phys*, vol. 38, pp. 1694–1704, Mar 2011.
- [56] A. Rosenthal, V. Ntziachristos, and D. Razansky, "Model-based optoacoustic inversion with arbitrary-shape detectors," *Medical Physics*, vol. 38, p. 4285, 2011.
- [57] C. Lawson and R. Hanson, *Solving least squares problems*. Society for Industrial Mathematics, 1995.
- [58] J. Glatz, N. C. Deliolanis, A. Buehler, D. Razansky, and V. Ntziachristos, "Blind source unmixing in multi-spectral optoacoustic tomography.," *Opt Express*, vol. 19, pp. 3175–3184, Feb 2011.
- [59] A. Rosenthal, D. Razansky, and V. Ntziachristos, "Quantitative optoacoustic signal extraction using sparse signal representation.," *IEEE Trans Med Imaging*, vol. 28, pp. 1997–2006, Dec 2009.
- [60] R. B. Schulz, A. Ale, A. Sarantopoulos, M. Freyer, E. Soehngen, M. Zientkowska, and V. Ntziachristos, "Hybrid system for simultaneous fluorescence and x-ray computed tomography.," *IEEE Trans Med Imaging*, vol. 29, pp. 465–473, Feb 2010.
- [61] K. Maslov, H. Zhang, and L. Wang, "Effects of wavelength-dependent fluence attenuation on the noninvasive photoacoustic imaging of hemoglobin oxygen saturation in subcutaneous vasculature in vivo," *Inverse Problems*, vol. 23, p. S113, 2007.
- [62] W. F. Cheong, S. A. Prahl, and A. J. Welch, "A review of the optical properties of biological tissues," *IEEE Journal of Quantum Electronics*, vol. 26, no. 12, pp. 2166–2185, 1990.
- [63] Z. Guo, S. Hu, and L. V. Wang, "Calibration-free absolute quantification of optical absorption coefficients using acoustic spectra in 3d photoacoustic microscopy of biological tissue.," *Opt Lett*, vol. 35, pp. 2067–2069, Jun 2010.
- [64] Y. Y. Petrov, I. Y. Petrova, I. A. Patrikeev, R. O. Esenaliev, and D. S. Prough, "Multiwavelength optoacoustic system for noninvasive monitoring of cerebral venous oxygenation: a pilot clinical test in the internal jugular vein.," *Opt Lett*, vol. 31, pp. 1827–1829, Jun 2006.
- [65] J.-T. Oh, M.-L. Li, H. F. Zhang, K. Maslov, G. Stoica, and L. V. Wang, "Three-dimensional imaging of skin melanoma in vivo by dual-wavelength photoacoustic microscopy.," *J Biomed Opt*, vol. 11, no. 3, p. 34032, 2006.

- [66] J. Nordlund, *The pigmentary system: physiology and pathophysiology*. Wiley-Blackwell, 2006.
- [67] Z. Xu, C. Li, and L. V. Wang, “Photoacoustic tomography of water in phantoms and tissue.,” *J Biomed Opt*, vol. 15, no. 3, p. 036019, 2010.
- [68] C. Tsai, J. Chen, and W. Wang, “Near-infrared absorption property of biological soft tissue constituents,” *Journal of Medical and Biological Engineering*, vol. 21, no. 1, pp. 7–14, 2001.
- [69] S. Sethuraman, J. H. Amirian, S. H. Litovsky, R. W. Smalling, and S. Y. Emelianov, “Spectroscopic intravascular photoacoustic imaging to differentiate atherosclerotic plaques.,” *Opt Express*, vol. 16, pp. 3362–3367, Mar 2008.
- [70] A. D. la Zerda, C. Zavaleta, S. Keren, S. Vaithilingam, S. Bodapati, Z. Liu, J. Levi, B. R. Smith, T.-J. Ma, O. Oralkan, Z. Cheng, X. Chen, H. Dai, B. T. Khuri-Yakub, and S. S. Gambhir, “Carbon nanotubes as photoacoustic molecular imaging agents in living mice.,” *Nat Nanotechnol*, vol. 3, pp. 557–562, Sep 2008.
- [71] V. Ntziachristos and D. Razansky, “Molecular imaging by means of multispectral optoacoustic tomography (msot).,” *Chem Rev*, vol. 110, pp. 2783–2794, May 2010.
- [72] S. Mallidi, T. Larson, J. Tam, P. P. Joshi, A. Karpiouk, K. Sokolov, and S. Emelianov, “Multiwavelength photoacoustic imaging and plasmon resonance coupling of gold nanoparticles for selective detection of cancer.,” *Nano Lett*, vol. 9, pp. 2825–2831, Aug 2009.
- [73] S. Chang, C. Shih, C. Chen, W. Lai, and C. Wang, “The shape transition of gold nanorods,” *Langmuir*, vol. 15, no. 3, pp. 701–709, 1999.
- [74] C. Didychuk, P. Ephrat, A. Chamson-Reig, S. Jacques, and J. Carson, “Depth of photothermal conversion of gold nanorods embedded in a tissue-like phantom,” *Nanotechnology*, vol. 20, p. 195102, 2009.
- [75] K. Song, E. Stein, J. Margenthaler, and L. Wang, “Noninvasive photoacoustic identification of sentinel lymph nodes containing methylene blue in vivo in a rat model,” *Journal of biomedical optics*, vol. 13, p. 054033, 2008.
- [76] X. Wang, G. Ku, M. A. Wegiel, D. J. Bornhop, G. Stoica, and L. V. Wang, “Noninvasive photoacoustic angiography of animal brains in vivo with near-infrared light and an optical contrast agent.,” *Opt Lett*, vol. 29, pp. 730–732, Apr 2004.

- [77] W. Lu, Q. Huang, G. Ku, X. Wen, M. Zhou, D. Guzatov, P. Brecht, R. Su, A. Oraevsky, L. V. Wang, and C. Li, "Photoacoustic imaging of living mouse brain vasculature using hollow gold nanospheres," *Biomaterials*, vol. 31, pp. 2617–2626, Mar 2010.
- [78] C. Kim, E. C. Cho, J. Chen, K. H. Song, L. Au, C. Favazza, Q. Zhang, C. M. Cobley, F. Gao, Y. Xia, and L. V. Wang, "In vivo molecular photoacoustic tomography of melanomas targeted by bioconjugated gold nanocages," *ACS Nano*, vol. 4, pp. 4559–4564, Aug 2004/2010.
- [79] J.-W. Kim, E. I. Galanzha, E. V. Shashkov, H.-M. Moon, and V. P. Zharov, "Golden carbon nanotubes as multimodal photoacoustic and photothermal high-contrast molecular agents," *Nat Nanotechnol*, vol. 4, pp. 688–694, Oct 2009.
- [80] K. Homan, S. Kim, Y.-S. Chen, B. Wang, S. Mallidi, and S. Emelianov, "Prospects of molecular photoacoustic imaging at 1064 nm wavelength," *Opt Lett*, vol. 35, pp. 2663–2665, Aug 2010.
- [81] A. de la Zerda, Z. Liu, S. Bodapati, R. Teed, S. Vaithilingam, B. T. Khuri-Yakub, X. Chen, H. Dai, and S. S. Gambhir, "Ultrahigh sensitivity carbon nanotube agents for photoacoustic molecular imaging in living mice," *Nano Lett*, vol. 10, pp. 2168–2172, Jun 2010.
- [82] D. Hunton, J. Bollman, and H. Hoffman, "Studies of hepatic function with indocyanine green," *Gastroenterology*, vol. 39, p. 713, 1960.
- [83] M. Eghtedari, A. Oraevsky, J. A. Copland, N. A. Kotov, A. Conjusteau, and M. Motamedi, "High sensitivity of in vivo detection of gold nanorods using a laser optoacoustic imaging system," *Nano Lett*, vol. 7, pp. 1914–1918, Jul 2007.
- [84] E. Dickerson, E. Dreaden, X. Huang, I. El-Sayed, H. Chu, S. Pushpanketh, J. McDonald, and M. El-Sayed, "Gold nanorod assisted near-infrared plasmonic photothermal therapy (phtt) of squamous cell carcinoma in mice," *Cancer letters*, vol. 269, no. 1, pp. 57–66, 2008.
- [85] A. G. Skirtach, C. Dejugnat, D. Braun, A. S. Susa, A. L. Rogach, W. J. Parak, H. Mhwald, and G. B. Sukhorukov, "The role of metal nanoparticles in remote release of encapsulated materials," *Nano Lett*, vol. 5, pp. 1371–1377, Jul 2005.
- [86] V. Ntziachristos, C.-H. Tung, C. Bremer, and R. Weissleder, "Fluorescence molecular tomography resolves protease activity in vivo," *Nat Med*, vol. 8, pp. 757–760, Jul 2002.

- [87] D. Razansky, N. J. Harlaar, J. L. Hillebrands, A. Taruttis, E. Herzog, C. J. Zeebregts, G. M. van Dam, and V. Ntziachristos, "Multispectral optoacoustic tomography of matrix metalloproteinase activity in vulnerable human carotid plaques.," *Mol Imaging Biol*, Jul 2011.
- [88] X. Shu, A. Royant, M. Z. Lin, T. A. Aguilera, V. Lev-Ram, P. A. Steinbach, and R. Y. Tsien, "Mammalian expression of infrared fluorescent proteins engineered from a bacterial phytochrome.," *Science*, vol. 324, pp. 804–807, May 2009.
- [89] D. Razansky, M. Distel, C. Vinegoni, R. Ma, N. Perrimon, R. K. Oster, and V. Ntziachristos, "Multispectral opto-acoustic tomography of deep-seated fluorescent proteins in vivo.," *Nature Photonics*, vol. 3, no. 7, pp. 412–417, 2009.
- [90] A. Krumholz, S. VanVickle-Chavez, J. Yao, T. Fleming, W. Gillanders, and L. Wang, "Photoacoustic microscopy of tyrosinase reporter gene in vivo.," *Journal of Biomedical Optics*, vol. 16, p. 080503, 2011.
- [91] F. A. Jaffer, P. Libby, and R. Weissleder, "Molecular imaging of cardiovascular disease.," *Circulation*, vol. 116, pp. 1052–1061, Aug 2007.
- [92] K. H. Song and L. V. Wang, "Noninvasive photoacoustic imaging of the thoracic cavity and the kidney in small and large animals.," *Med Phys*, vol. 35, pp. 4524–4529, Oct 2008.
- [93] R. J. Zemp, L. Song, R. Bitton, K. K. Shung, and L. V. Wang, "Real-time photoacoustic microscopy of murine cardiovascular dynamics.," *Opt Express*, vol. 16, pp. 18551–18556, Oct 2008.
- [94] J. Chen, C.-H. Tung, U. Mahmood, V. Ntziachristos, R. Gyurko, M. C. Fishman, P. L. Huang, and R. Weissleder, "In vivo imaging of proteolytic activity in atherosclerosis.," *Circulation*, vol. 105, pp. 2766–2771, Jun 2002.
- [95] J. Waldeck, F. Hger, C. Hltke, C. Lanckohr, A. von Wallbrunn, G. Torsello, W. Heindel, G. Theilmeyer, M. Schfers, and C. Bremer, "Fluorescence reflectance imaging of macrophage-rich atherosclerotic plaques using an alphavbeta3 integrin-targeted fluorochrome.," *J Nucl Med*, vol. 49, pp. 1845–1851, Nov 2008.
- [96] M. Nahrendorf, P. Waterman, G. Thurber, K. Groves, M. Rajopadhye, P. Panizzi, B. Marinelli, E. Aikawa, M. J. Pittet, F. K. Swirski, and R. Weissleder, "Hybrid in vivo fnt-ct imaging of protease activity in atherosclerosis with customized nanosensors.," *Arterioscler Thromb Vasc Biol*, vol. 29, pp. 1444–1451, Oct 2009.

- [97] C. K. Zarins, D. P. Giddens, B. K. Bharadvaj, V. S. Sottiurai, R. F. Mabon, and S. Glagov, "Carotid bifurcation atherosclerosis. quantitative correlation of plaque localization with flow velocity profiles and wall shear stress.," *Circ Res*, vol. 53, pp. 502–514, Oct 1983.
- [98] F. Dunn, "Attenuation and speed of ultrasound in lung.," *J Acoust Soc Am*, vol. 56, pp. 1638–1639, Nov 1974.
- [99] A. Jain, M. Murty, and P. Flynn, "Data clustering: a review," *ACM computing surveys (CSUR)*, vol. 31, no. 3, pp. 264–323, 1999.
- [100] F. K. Swirski, M. Nahrendorf, M. Etzrodt, M. Wildgruber, V. Cortez-Retamozo, P. Panizzi, J.-L. Figueiredo, R. H. Kohler, A. Chudnovskiy, P. Waterman, E. Aikawa, T. R. Mempel, P. Libby, R. Weissleder, and M. J. Pittet, "Identification of splenic reservoir monocytes and their deployment to inflammatory sites.," *Science*, vol. 325, pp. 612–616, Jul 2009.
- [101] M. Nahrendorf, D. E. Sosnovik, P. Waterman, F. K. Swirski, A. N. Pande, E. Aikawa, J.-L. Figueiredo, M. J. Pittet, and R. Weissleder, "Dual channel optical tomographic imaging of leukocyte recruitment and protease activity in the healing myocardial infarct.," *Circ Res*, vol. 100, pp. 1218–1225, Apr 2007.
- [102] J. Dervede, A. Rausch, M. Weinhart, S. Enders, R. Tauber, K. Licha, M. Schirner, U. Zgel, A. von Bonin, and R. Haag, "Dendritic polyglycerol sulfates as multivalent inhibitors of inflammation.," *Proc Natl Acad Sci U S A*, vol. 107, pp. 19679–19684, Nov 2010.
- [103] M. Khalil, H. Kim, I. Kim, R. Dayal, and A. Hielscher, "Detecting lower extremity vascular dynamics in patients with peripheral artery disease using diffuse optical tomography," in *Proceedings of SPIE*, vol. 7896, p. 78962Z, 2011.
- [104] R. K. Jain, L. L. Munn, and D. Fukumura, "Dissecting tumour pathophysiology using intravital microscopy.," *Nat Rev Cancer*, vol. 2, pp. 266–276, Apr 2002.
- [105] R. Siphanto, K. Thumma, R. Kolkman, T. Leeuwen, F. Mul, J. Neck, L. Adrichem, and W. Steenbergen, "Serial noninvasive photoacoustic imaging of neovascularization in tumor angiogenesis," *Optics express*, vol. 13, no. 1, pp. 89–95, 2005.
- [106] Y. Lao, D. Xing, S. Yang, and L. Xiang, "Noninvasive photoacoustic imaging of the developing vasculature during early tumor growth," *Physics in Medicine and Biology*, vol. 53, p. 4203, 2008.

-
- [107] H. Maeda, J. Wu, T. Sawa, Y. Matsumura, and K. Hori, "Tumor vascular permeability and the epr effect in macromolecular therapeutics: a review.," *J Control Release*, vol. 65, pp. 271–284, Mar 2000.
- [108] G. Cherrick, S. Stein, C. Leevy, and C. Davidson, "Indocyanine green: observations on its physical properties, plasma decay, and hepatic extraction," *Journal of Clinical Investigation*, vol. 39, no. 4, p. 592, 1960.
- [109] A. Skirtach, C. Dejumat, D. Braun, A. Susa, A. Rogach, W. Parak, H. M
"ohwald, and G. Sukhorukov, "The role of metal nanoparticles in remote release of encapsulated materials," *Nano letters*, vol. 5, no. 7, pp. 1371–1377, 2005.
- [110] K. A. Whitehead, R. Langer, and D. G. Anderson, "Knocking down barriers: advances in sirna delivery.," *Nat Rev Drug Discov*, vol. 8, pp. 129–138, Feb 2009.
- [111] D. Peer, J. M. Karp, S. Hong, O. C. Farokhzad, R. Margalit, and R. Langer, "Nanocarriers as an emerging platform for cancer therapy.," *Nat Nanotechnol*, vol. 2, pp. 751–760, Dec 2007.
- [112] M. S. Shim and Y. J. Kwon, "Efficient and targeted delivery of sirna in vivo.," *FEBS J*, vol. 277, pp. 4814–4827, Dec 2010.
- [113] X. Deán-Ben, V. Ntziachristos, and D. Razansky, "Statistical optoacoustic image reconstruction using a-priori knowledge on the location of acoustic distortions," *Applied Physics Letters*, vol. 98, no. 17, pp. 171110–171110, 2011.
- [114] D. Razansky, J. Baeten, and V. Ntziachristos, "Sensitivity of molecular target detection by multispectral optoacoustic tomography (msot).," *Med Phys*, vol. 36, pp. 939–945, Mar 2009.
- [115] Y. Wang, K. Maslov, Y. Zhang, S. Hu, L. Yang, Y. Xia, J. Liu, and L. V. Wang, "Fiber-laser-based photoacoustic microscopy and melanoma cell detection.," *J Biomed Opt*, vol. 16, no. 1, p. 011014, 2011.
- [116] A. Sarantopoulos, G. Themelis, and V. Ntziachristos, "Imaging the bio-distribution of fluorescent probes using multispectral epillumination cryoslicing imaging.," *Mol Imaging Biol*, Sep 2010.
- [117] V. Ntziachristos, G. Turner, J. Dunham, S. Windsor, A. Soubret, J. Ripoll, and H. A. Shih, "Planar fluorescence imaging using normalized data.," *J Biomed Opt*, vol. 10, no. 6, p. 064007, 2005.

Acknowledgements

I am grateful to Athanasios Sarantopoulos and George Themelis for technical advice and assistance with fluorescence imaging, Rui Ma, Andreas Bühler, Andreas Oancea, Till Gradinger and Josef Konradl for assistance with instrumentation, Miguel Araque Caballero and Thomas Jetzfellner for help with simulations, Luis Dean Ben and Daniel Queiros for simulation and reconstruction code and related support, Nikolaos Deliolanis, Jerome Gateau and Amir Rosenthal for assistance with problem solving and theory, Angélique Ale for setting me up with light propagation models et cetera, Eva Herzog for helping me develop successful experimental methods, Niels Harlaar, Nicolas Beziere, Neal Burton, Jing Shi and Stefan Morscher for performing studies together with me, Moritz Wildgruber, Eliane Weidl and Katja Kosanke for providing mouse models and experimental support, Kai Licha for providing novel imaging agents, Daniel Razansky for guidance and Vasilis Ntziachristos for guidance and getting me into this exciting field in the first place.